Stability of Anisotropic Gap Solitons in Photorefractive Media

Vom Fachbereich Physik
der Technischen Universität Darmstadt
zur Erlangung des Grades
eines Doktors der Naturwissenschaften
(Dr. rer. nat.)

genehmigte

DISSERTATION

von

Dipl.-Phys. Tobias Richter

aus Frankfurt am Main

Darmstadt 2008
D17

Referent:	Prof. Dr. Friedemann Kaiser
Korreferent:	Prof. Dr. Robert Roth
Tag der Einreichung:	14.5.2008
Tag der mündlichen Prüfung:	23.6.2008

Contents

1 Introduction **1**
- 1.1 Nonlinear photonic crystals . . . 2
- 1.2 Outline of this work . . . 4

2 Light propagation in nonlinear photonic media **5**
- 2.1 Propagation equation . . . 5
- 2.2 Photorefractive nonlinearity . . . 7
- 2.3 Photonic lattices . . . 12
  - 2.3.1 Additive periodic potential . . . 12
  - 2.3.2 Optical induction . . . 14
- 2.4 Gap solitons . . . 15

3 Stability of gap solitons in statically imprinted photonic lattices **19**
- 3.1 Basic (lowest-intensity) gap solitons . . . 20
  - 3.1.1 Linear stability analysis . . . 21
  - 3.1.2 1D numerical simulations . . . 23
  - 3.1.3 2D numerical simulations . . . 29
- 3.2 Soliton clusters . . . 33
  - 3.2.1 Amplitude profiles . . . 33
  - 3.2.2 Stability . . . 35

4 Gap solitons in optically induced photonic lattices **39**
- 4.1 Lattice types . . . 39
  - 4.1.1 Square and rectangular symmetry . . . 39
  - 4.1.2 Hexagonal symmetry . . . 41
- 4.2 Band structure and basic solitons . . . 43
  - 4.2.1 Diamond and vortex lattices . . . 43
  - 4.2.2 Horizontal triangular lattice . . . 47
  - 4.2.3 Vertical triangular lattice . . . 51
- 4.3 Soliton clusters . . . 54

5 Gap vortices and vortex clusters **57**
- 5.1 Necessary stability criterion . . . 58
- 5.2 Elementary vortex clusters (focusing nonlinearity) . . . 58
- 5.3 Multivortex clusters . . . 63
  - 5.3.1 Clusters with triangular shape . . . 63
  - 5.3.2 Clusters with hexagonal shape . . . 65

5.4 Defocusing vortex clusters 69
5.5 Ring-shaped vortex clusters 70

6 Stability of symmetric gap vortices **73**
6.1 Focusing media 73
6.1.1 Semi-infinite gap 73
6.1.2 First gap 77
6.2 Defocusing media 79

7 Summary and outlook **85**

Zusammenfassung **89**

Appendices **93**

A Numerical calculation of gap solitons **93**
A.1 Gradient-based methods 93
A.2 Petviashvili methods 94

B Numerical beam propagation and absorbing boundary conditions **97**

Bibliography **101**

Danksagung **107**

1 Introduction

From linear media, it is well known that harmonic waves of different frequencies may travel at different phase velocities. This phenomenon is called *dispersion*. Depending on whether the phase velocity decreases or increases with the frequency, one speaks of *normal* or *anomalous* dispersion. For a localized pulse, which can be regarded as a superposition of several harmonic waves with slightly different frequencies, this results in a broadening (normal dispersion) or steepening (anomalous dispersion) of its shape during the propagation.

However, if the response of the medium becomes *nonlinear*, the phase velocity also depends on the amplitude of the wave, and the superposition principle does not hold anymore. Since the nonlinearity effectively changes the spectrum of the pulse, it also may countervail the dispersion. In this case special pulse shapes exist, for which diffraction and nonlinear effects exactly counterbalance each other. Such pulses are known as *solitary waves*; they propagate without any change in shape or speed through the medium in spite of being nonlinear waves.

Historically, the first observation of a solitary wave was made already in 1834 by John Scott Russell [1]. He observed a wave propagating in a shallow water canal over several kilometers without becoming significantly distorted. In 1965, Zabusky and Kruskal found by numerically studying the Korteweg-de Vries equation that solitary waves may maintain their shapes even after strongly interacting with each other during collisions [2]. In order to emphasize this particle-like behavior, they introduced the word *soliton*. While originally this term was used only in a strict sense implying this characteristic interaction property, it is often used as a synonym for 'solitary wave' in the literature nowadays. In this latter sense it shall also be used within this thesis.

In optics, nonlinear effects arise when the light intensity is high enough, so that material parameters like the refractive index become intensity-dependent. Since in most media this requires very high beam powers, nonlinear optical effects have not been noticed until the first lasers were available. Already in 1964, it was found that optical nonlinearities can countervail the diffraction, leading to *self-focusing* and *self-trapping* of a beam [3]. Subsequently it was realized that for a simple, cubic nonlinearity, paraxial propagation models predict the beam to self-focus until its shape becomes singular, if the initial intensity exceeds a certain threshold (*catastrophic self-focusing*, [4, 5]). Experimentally it was found that the catastrophic self-focusing is often preceded by a break-up of the beam into multiple filaments (*filamentation*). This is confirmed by the theoretical models, if vectorial effects are taken into account, or if the initial beam is perturbed by random noise [6] (and references therein).

Based on the effect of self-focusing, it was theoretically predicted in 1992 that *optical solitons* should exist in *photorefractive crystals* [7]. These media have two advantages: On the one hand, they require only small beam powers in order to show nonlinear effects. On the other hand, their nonlinear response is *saturable*, i.e., it cannot grow infinitely for large intensities. Therefore catastrophic self-focusing does not occur in photorefractive crystals. Nevertheless, filamentation can still be observed as a result of transversal modulational instabilities [8]. In 1993 photorefractive solitons could be demonstrated experimentally [9].

Solitons arising from a self-focusing nonlinearity consist of a center with one (or more) localized bright spots, whereas the intensity outside of this center asymptotically approaches zero. Hence this soliton type is called a *bright soliton*. A counterpart, the so-called *dark soliton* with an inverted intensity profile, may be obtained if the sign (or character) of the nonlinearity is reversed, thus yielding a self-defocusing medium. Dark solitons are not subject to this thesis however.

Photorefractive solitons are an example of *spatial solitons*, since it is the diffraction as a kind of "spatial dispersion" which is counterbalanced by the nonlinearity. Once established, these solitons are steady-state phenomena. By contrast, the travelling solitons in water canals are called *temporal solitons*. They do not change their shape either, but their propagation is a temporal phenomenon. In nonlinear optics temporal solitons exist as well, e.g., in the form of pulses propagating through a nonlinear fiber.

One motivation for the investigation of optical solitons is their ability to transport a certain amount of energy or information over quite large distances without dispersion-related losses. Moreover, they are of theoretical interest as fundamental nonlinear structures, which may arise from or being preserved during the interaction of beams. Their interaction behavior can also be used to control or manipulate the propagation of optical beams including, e.g., the realization of all-optical switches [10].

1.1 Nonlinear photonic crystals

In modern optics periodically modulated structures, commonly known as *photonic crystals*, have started to play an important role after they had originally been suggested in the 1980s [11, 12]. Also in these media spatial solitons are possible in the presence of a nonlinearity [13], and the investigation of their properties is quite an active field up to now [14–16].

Additional interest in this topic arises from the fact that the nonlinear Schrödinger equation, which describes solitons in nonlinear photonic crystals in a scalar approximation, is also applicable to Bose-Einstein condensates (BEC) in periodic, optical traps (in this context, it is referred to as *Gross-Pitaevskii equation* [17]).

Since Zobay et al. [18] realized in 1999 that solitons should consequently exist in this system as well, they have been investigated in parallel [19, 20] with their

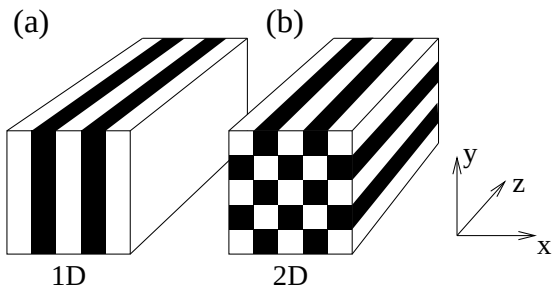

Figure 1.1: Lower-dimensional photonic crystals ("lattices"), being homogeneous in propagation (z) direction. (a) 1D case; (b) 2D case.

optical counterparts in photonic media [21]. Experimentally, such (bright) *matter wave solitons* were first observed in [22].

Photonic crystals are the optical analog of crystal structures in solid state physics. However, in contrast to the latter they are not necessarily periodic in all three dimensions. If they are homogeneous in one or even two directions, they are often referred to as 2D or 1D photonic lattices (Figure 1.1). These "reduced" cases are also the center of interest in this work, where it is assumed that the beam propagates along a homogeneous direction of the crystal.

Efremidis et al. demonstrated in 2002 that such lattices can be reversibly induced in photorefractive crystals using purely optical methods [23]. This result renders them well-suited for studying the properties both of photonic lattices itself [24] and of solitons therein [25, 26]. Even typical solid state phenomena like Bloch oscillations and Zener tunneling may be studied [27]. Moreover, this system may serve as a "model system" for BEC in optical lattices due to the aforementioned analogy.

According to Bloch's theorem, wave propagation in photonic crystals is possible only if the corresponding wave vectors lie within certain intervals, which are called *Bloch bands*. The intervals between the Bloch bands are called *photonic band gaps* or just gaps. It turns out that there is always exactly one semi-infinite gap, whereas all other gaps are finite. This semi-infinite gap corresponds to the forbidden regime below the ground state of an electron in a periodic potential.

Since in a nonlinear optical medium the refractive index depends on the intensity, the same holds for the wave vector as well. This means that in *nonlinear photonic crystals* its component pointing in propagation direction is shifted by the nonlinearity and may now lie within a gap (relating to the linear regime). Thus in presence of a nonlinearity wave propagation in the linear band gaps becomes possible. These nonlinear gap waves may be spatially localized, and in the case of solitary propagation one speaks of *gap solitons*.

Physically seen, the self-guiding property of gap solitons arises from two different origins: On the one hand, it can be based on the local elevation of the refractive index in the presence of a focusing nonlinearity, such as in homogeneous media.

This is the case for solitons in the semi-infinite gap, or in the (transversally) homogeneous direction of an 1D photonic lattice [cf. Figure 1.1 (a)]. On the other hand, self-guiding may occur due to transversal Bragg reflection. This is the dominant mechanism in all finite gaps. The Bragg reflection also enables the formation of bright solitons in *defocusing* photonic media, whereas this is obviously impossible in homogeneous media (the diffraction is always enhanced in this case).

1.2 Outline of this work

The aim of this thesis is an in-depth study of the stability properties of gap solitons in photorefractive media. The focus lies on optically induced photonic lattices in connection with a realistic, anisotropic model of the photorefractive nonlinearity. This system is chosen since it is easily accessible in the experiment.

The necessary fundamentals are recapitulated in chapter 2. At first, a scalar propagation equation for lossless, nonlinear photonic media is introduced. A short derivation of the photorefractive nonlinearity is given as well. Furthermore, the technique of optically inducing photonic lattices in photorefractive crystals is explained. These optically induced lattices are distinguished from statically imprinted ones. Finally, some basic properties of gap solitons are discussed.

In chapter 3, the stability properties of elementary gap solitons are investigated depending on the lattice strength. Additionally the influence of the character of the nonlinearity (focusing or defocusing) is discussed in connection with the order (number) of the gap. Furthermore, the stability of soliton clusters is investigated. Since the quite special features of the photorefractive nonlinearity are pronounced by optically induced lattices, these general investigations are done exemplarily for statically imprinted lattices. This also increases the similarities to the Gross-Pitaevskii equation.

In chapter 4 some basic lattice types are compared, which are well-suited (also in the experiment) for optical induction. The emphasis is on the influence of the lattice geometry in view of the support of different types of gap solitons. It is shown that in some cases the symmetry reduction due to the photorefractive anisotropy has significant consequences.

The capters 5 and 6 deal with the properties of gap vortices and vortex clusters, i.e., structures containing one or more phase singularities, which are associated with circular intensity flows. In chapter 5, necessary conditions are derived for the propagation of various vortex clusters to be stable though the nonlinearity is anisotropic. In chapter 6, the stability of (mirror) symmetric vortices is investigated. In this context, also gap vortices being localized at *single* lattice sites are discussed.

Finally, the numerical methods used to determine the soliton profiles and to solve the propagation equation with absorbing boundary conditions are described in the appendices A and B.

2 Light propagation in nonlinear photonic media

Due to the vectorial nature of the underlying fields, the general case of a light wave propagating in a nonlinear medium is rather complex. Therefore a large number of simplified wave equations has been derived in the past, each of which is valid for a certain range of practical cases.

In this work we consider photorefractive crystals, which are usually birefringent. Furthermore the photorefractive nonlinearity is strongly polarization dependent, thus we assume linearly polarized beams in all cases. The geometry is chosen such that the crystal can be regarded as uniaxial even in the nonlinear regime. The beam propagates always perpendicular to the optical axis, while the polarization is always strictly ordinary or extraordinary. Typical transversal structure sizes or beam diameters are about 10 μm or above. Therefore a scalar propagation model is sufficient in our case. At first we derive such a model for homogeneous media. Thereafter we show that it can be easily generalized to the case of periodic structures (i.e., photonic crystals).

2.1 Propagation equation

In order to derive a scalar, nonlinear propagation equation we start from Maxwell's equations:

$$\boldsymbol{\nabla} \times \mathbf{E} + \frac{1}{c}\frac{\partial \mathbf{B}}{\partial t} = 0 \tag{2.1}$$

$$\boldsymbol{\nabla} \times \mathbf{H} = \frac{4\pi}{c}\mathbf{j} + \frac{1}{c}\frac{\partial \mathbf{D}}{\partial t} \tag{2.2}$$

$$\boldsymbol{\nabla} \cdot \mathbf{D} = 4\pi\rho \tag{2.3}$$

$$\boldsymbol{\nabla} \cdot \mathbf{B} = 0. \tag{2.4}$$

The vectors $\mathbf{D}$ and $\mathbf{B}$ are related to the fields $\mathbf{E}$ and $\mathbf{H}$ through the material equations

$$\mathbf{D} = \mathbf{E} + 4\pi\mathbf{P} \tag{2.5}$$

$$\mathbf{B} = \mathbf{H} + 4\pi\mathbf{M}. \tag{2.6}$$

Photorefractive crystals are non-magnetic ($\mathbf{M} = 0$), and we can assume that there are no free charges or currents ($\rho = 0$ and $\mathbf{j} = 0$). Since we consider monochromatic light, the polarization can be written as $\mathbf{P}(t) = \chi(I)\mathbf{E}(t)$ with an effective, intensity dependent susceptibility χ ($I \equiv |E|^2$). Equation (2.5) can then be written as

$\mathbf{D} = (1+4\pi\chi)\mathbf{E} = \varepsilon\mathbf{E}$, where we have already used the fact that a scalar treatment of χ is sufficient in our case.

Inserting Eqn. (2.2) into Eqn. (2.1) and using the relation $\boldsymbol{\nabla}\times\boldsymbol{\nabla}\times\mathbf{E} = -\boldsymbol{\nabla}^2\mathbf{E} + \boldsymbol{\nabla}(\boldsymbol{\nabla}\cdot\mathbf{E})$ then yields

$$\boldsymbol{\nabla}^2\mathbf{E} - \boldsymbol{\nabla}(\boldsymbol{\nabla}\cdot\mathbf{E}) - \frac{n^2}{c^2}\frac{\partial^2\mathbf{E}}{\partial t^2} = 0, \tag{2.7}$$

where we introduced the intensity dependent, effective refractive index $n(I) = \sqrt{1+4\pi\chi(I)}$. The $-\boldsymbol{\nabla}(\boldsymbol{\nabla}\cdot\mathbf{E})$ term on the left hand side can also be written as $2\boldsymbol{\nabla}\left(\frac{1}{n}(\boldsymbol{\nabla}n)\cdot\mathbf{E}\right)$ by using that $\boldsymbol{\nabla}\cdot\mathbf{D} = 0$. The changes of n caused by the light are small, and even for localized beams the partial derivatives of n are smaller than those of $\mathbf{E}$. We can therefore neglect this term and obtain the Helmholtz equation

$$\boldsymbol{\nabla}^2\mathbf{E} - \frac{n^2}{c^2}\frac{\partial^2\mathbf{E}}{\partial t^2} = 0. \tag{2.8}$$

In the following it will be useful to split n^2 into a static part n_0^2 ("dark" crystal) and a light-induced change δn^2 by writing $n^2 = n_0^2 + \delta n^2$. Additionally we introduce the abbreviations $\mathbf{r} \equiv (\mathbf{r}_\perp, z) \equiv (x, y, z)$ and $\nabla_\perp^2 \equiv \partial_{xx} + \partial_{yy}$. Assuming a wave which is linearly polarized in x direction and propagating in z direction, we then can write $\mathbf{E}(\mathbf{r}, t) = A(\mathbf{r})e^{i(k_z z-\omega t)}\cdot\mathbf{e}_x$ with $k_z = n_0 k_0$ and $k_0 = \omega/c$. If the condition

$$|\partial_{zz}A| \ll |k_z\partial_z A| \tag{2.9}$$

is met, we can neglect the double partial z derivative of A as well and find

$$i\partial_z A = -\frac{1}{2k_z}\boldsymbol{\nabla}_\perp^2 A - \frac{k_z}{2n_0^2}\delta n^2(I)A. \tag{2.10}$$

The condition (2.9) is also known as *Slowly Varying Amplitude Approximation* (SVAA). It is fully equivalent to the assumption of a paraxial beam propagation in the sense that $k_x^2 + k_y^2 \ll k_z^2$ holds for all significant Fourier components of the beam. This can be easily verified when solving the Helmholtz equation (2.8) in the Fourier space [28]. Within the scope of the SVAA it is also justifiable to neglect the vectorial character of $\mathbf{E}$ (namely the E_z component).

It is convenient to make Eqn. (2.10) dimensionless by expressing x and y in units of a transversal scale w_0 and z in units of $z_0 = k_z w_0^2$. This leads to

$$i\partial_z A = -\frac{1}{2}\boldsymbol{\nabla}_\perp^2 A - \frac{k_0^2 w_0^2}{2}\delta n^2(I)A. \tag{2.11}$$

In a homogeneous, linear medium z_0 can be associated with the so-called *diffraction length*, after which a Gaussian beam with the diameter 1 (relating to $1/e$) has doubled its width due to the diffraction.

Equation (2.11) is the basic propagation model which is used throughout this work. However, we still need to derive an expression for the nonlinear response $\delta n^2(I) = \delta n^2(|A|^2)$. This is done in the next section.

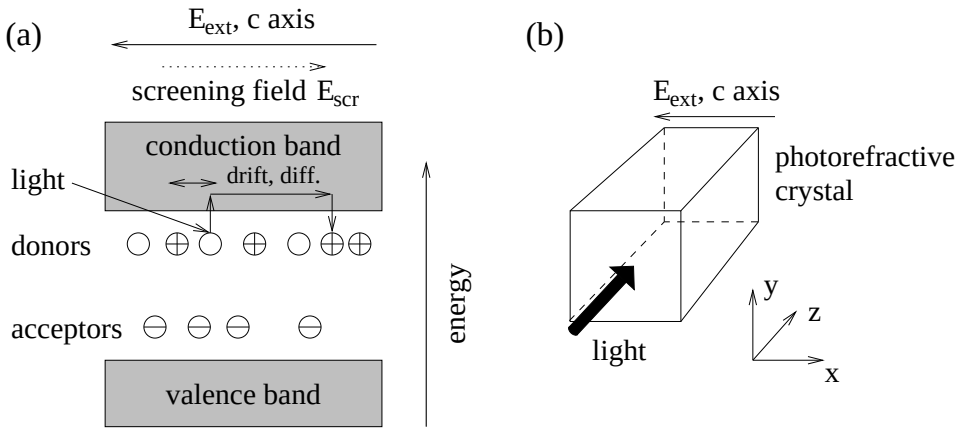

Figure 2.1: (a) charge carrier transport in photorefractive crystals. Ionized donors and acceptors are marked with $\oplus$ and $\ominus$. (b) geometry and coordinate system.

2.2 Photorefractive nonlinearity

Photorefractive crystals are one class of nonlinear optical media, i.e., their refractive index depends on the intensity of the incident light. They are quite common objects for experimental studies, since the nonlinear effects are observable at much lower intensities (Milliwatts of beam powers are sufficient) than in usual Kerr media. For that reason we also choose them as model system in this work. Examples of photorefractive crystals are $LiNbO_3$, $KNbO_3$ or the widely used $Sr_{1-x}Ba_xNb_2O_6$ (SBN). The photorefractive effect is based on the Pockels effect in combination with charge transport mechanisms and requires an external electric field. These transport processes, and thus the nonlinear response, are quite slow however. The time constants strongly depend on the material and on the light intensity, for SBN they range from seconds (bright environment) to several minutes (dark environment). Therefore an (incoherent) background illumination is always desirable.

Photorefractive crystals are transparent semiconductors (in the visible and near-infrared regime), which are doped with donors and acceptors [Figure 2.1 (a)]. Usually the concentration of the donors N_D is approximately three orders of magnitude larger than those of the acceptors N_A. Thus in a dark environment all acceptors can assumed to be occupied, leaving an equivalent number N_D^+ of donors per unit volume ionized ($N_D^+ = N_A$). If the crystal is illuminated by a light beam, whose frequency ω matches the energy difference between the donor niveau and the conduction band, donor electrons will jump into the conduction band and move around by drifting in the externally applied electrical field E_{ext} or by diffusion [Figure 2.1 (a)]. When they reach an unlighted area again, they recombine with another ionized donor. Due to the drift an electrical screening field E_{scr} pointing contrary to E_{ext} is built up. A steady state is reached when both fields balance each other.

Quantitatively, these processes can be described by a set of five equations which have originally been introduced by Kukhtarev et al. [29] in 1979:

First, the rate G_N of electrons, which are excited into the conduction band by a beam of the intensity I, is given by

$$G_N = (\beta_e + sI)(N_D - N_D^+) - \gamma_e N N_D^+, \tag{2.12}$$

with N being the charge carrier (electron) density in the conduction band, and s and γ_e denoting the photo-ionization and the recombination coefficients. The coefficient β_e accounts for non-optical (e.g., thermal) excitations of electrons into the conduction band. It is possible to combine the latter with the intensity I_b of the background illumination to an effective background ("dark") intensity $I_d = \beta_e/s + I_b$. Usually s and I are expressed in units of I_d; we will do this throughout the rest of this work.

The total current density $\mathbf{j}$ in the conduction band is given by

$$\mathbf{j} = e\mu N \mathbf{E}_{ext} + \mu k_B T \boldsymbol{\nabla} N + \hat{p}_n \mathbf{e}_p (N_D - N_D^+) I. \tag{2.13}$$

Herein the first and second terms describe the drift and diffusion effects, while the last one accounts for photovoltaic effects. The constant μ denotes the mobility of the electrons (with the charge e), $\hat{p}_n$ is the photovoltaic tensor, the unit vector $\mathbf{e}_p$ gives the polarization direction of the incident light wave, T is the temperature, and k_B denotes Boltzmann's constant. $\mathbf{E}_{ext}$ is assumed to be homogeneous and temporally constant. In this work the coordinate system [Figure 2.1 (b)] is always chosen such that $\mathbf{E}_{ext}$ is parallel to the x axis (i.e., $\mathbf{E}_{ext} = E_{ext}\mathbf{e}_x$), and the light is propagating in z direction. If nothing else is specified, we will assume $\mathbf{e}_p = \mathbf{e}_x$ as well.

The temporal change of the concentration of ionized donors is given by

$$\frac{\partial N_D^+}{\partial t} = G_N, \tag{2.14}$$

and we have the continuity equation

$$\frac{\partial N}{\partial t} = G_N + \frac{1}{e}\boldsymbol{\nabla}\mathbf{j}. \tag{2.15}$$

Together with Gauss's law [cf. Eqn. (2.3)]

$$\boldsymbol{\nabla}(\hat{\varepsilon}\mathbf{E}_{ges}) = -4\pi e(N + N_A - N_D^+), \tag{2.16}$$

with $\mathbf{E}_{ges} = \mathbf{E}_{ext} + \mathbf{E}_{scr}$ being the total electrical field in the crystal, the set of (2.12)-(2.16) is also known as *Kukhtarev's equations*.

$\mathbf{E}_{ges}$ is directly connected with the light-induced change of the dielectric tensor (and therefore of the refractive index) via the Pockels effect:

$$\Delta\varepsilon_{ij} = -n_i^2 n_j^2 r_{ijk} E_k. \tag{2.17}$$

Herein r_{ijk} is called *linear electro-optic tensor*, n_i and n_j denote the unperturbed refractive indices along the three coordinate axes[1], and E_k is the k-th component of $\mathbf{E}_{ges}$ (for k Einstein's sum convention applies). SBN crystals have a preferential direction (c axis), which we assume to point in x direction as well [see Figure 2.1 (b)]. This results in a dominating element $r_{333} \equiv r_{33} \equiv r_{eff}$ of the electro-optic tensor; all other elements are more than one order of magnitude smaller than r_{eff} and can therefore be neglected. We then obtain the following effective change of the refractive index, if the incident light is polarized in x direction:

$$\delta n^2 = n^2 - n_0^2 = -n_0^4 r_{eff} \mathbf{E}_{ges} \cdot \mathbf{e}_x. \tag{2.18}$$

Since the underlying charge carrier dynamics is slow, $\mathbf{E}_{scr}$ and $\mathbf{E}_{ges}$ can be conveniently expressed by scalar potentials:

$$\begin{aligned} \mathbf{E}_{scr} &= -\boldsymbol{\nabla}\tilde{\phi}, \\ \mathbf{E}_{ges} &= -\boldsymbol{\nabla}\phi = -\boldsymbol{\nabla}\tilde{\phi} + \mathbf{E}_{ext}. \end{aligned} \tag{2.19}$$

When solving the propagation equation, it is indeed allowed to use $\mathbf{E}_{scr}$ instead of $\mathbf{E}_{ges}$ in Eqn. (2.18), since here the contribution of $\mathbf{E}_{ext}$ alone is just a phase factor. Omitting this term is therefore equivalent to rescaling n_0. As it is only the x component of $\mathbf{E}_{scr}$ which determines the nonlinear change δn^2, we simply refer to it as E_{scr} in the following.

In 1995 Zozulya and Anderson derived under some simplifying, but well-justified assumptions an equation for ϕ directly from Kukhtarev's equations [30]. Rescaled to $\tilde{\phi}$ and using the abbreviation $\kappa = k_B T/q = -k_B T/e$ it reads

$$\begin{aligned} \frac{\tau_0}{1+I}\partial_t \left(\boldsymbol{\nabla}(\hat{\varepsilon}\boldsymbol{\nabla}\tilde{\phi}) \right) + \Delta\tilde{\phi} + \boldsymbol{\nabla}\ln(1+I)\boldsymbol{\nabla}\tilde{\phi} &= E_{\text{ext}}\partial_x \ln(1+I) \\ -\kappa\left[\Delta\ln(1+I) + (\boldsymbol{\nabla}\ln(1+I))^2\right] &- \boldsymbol{\eta}\boldsymbol{\nabla}\ln(1+I), \end{aligned} \tag{2.20}$$

with the relaxation time

$$\tau_0 = \frac{\gamma_e}{4\pi e\mu s}\frac{N_A}{(N_D - N_A)} \tag{2.21}$$

and the photovoltaic tensor

$$\boldsymbol{\eta} = \frac{N_A \hat{p}_n \mathbf{e}_x}{e\mu}. \tag{2.22}$$

For SBN crystals the y and the z components of $\boldsymbol{\eta}$ can be neglected, so the remaining term for η_x can be taken into account by introducing an effective external field $\tilde{E}_{ext} = E_{ext} - \eta_x$. In the following we will drop the tilde and assume silently, that the photovoltaic term is included in E_{ext} if it cannot be neglected. Furthermore, we are interested only in steady state phenomena. Thus we may set all temporal

[1] we follow the convention that the index 3 denotes the direction of the c axis (i.e., 1 and 2 denote the y and z directions)

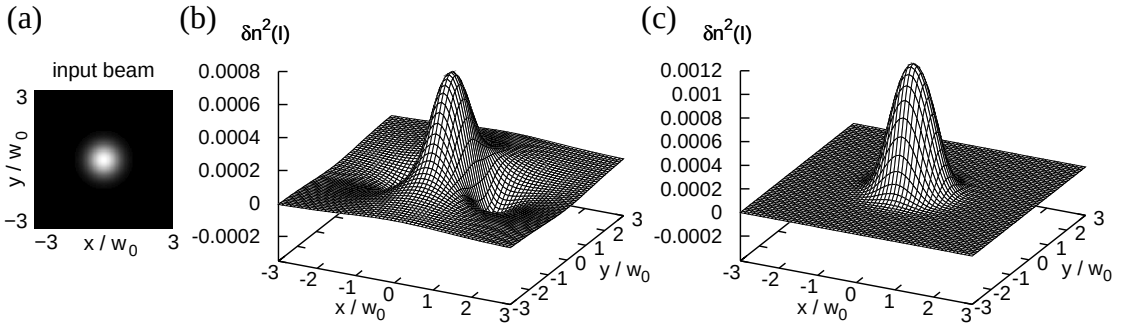

Figure 2.2: Photorefractive nonlinearity (self-focusing case, $E_{ext} = 2.5\text{kV/cm}$). (a) Gaussian input beam ($I_{max} = 1$; light gray tones denote high intensities); (b) δn^2 in the anisotropic model [Eqn. (2.23)]; (c) δn^2 in the isotropic model [Eqn. (2.24)].

derivatives equal to zero. The same holds for the z derivatives of $\tilde{\phi}$, since the relevant length scale (w_0) of the transverse structures is more than two orders of magnitude smaller than that of the dynamics in propagation direction (z_0). The z derivatives vanish exactly for solitons. Equation (2.20) then reads:

$$\begin{aligned}\boldsymbol{\nabla}_\perp^2\tilde{\phi} + \boldsymbol{\nabla}_\perp \ln(1+I)\boldsymbol{\nabla}_\perp\tilde{\phi} = E_{\text{ext}}\partial_x \ln(1+I) \\ - \kappa\left[\boldsymbol{\nabla}_\perp^2 \ln(1+I) + (\boldsymbol{\nabla}_\perp \ln(1+I))^2\right].\end{aligned} \tag{2.23}$$

This equation contains all relevant information about the photorefractive nonlinearity (i.e., the dependency $E_{scr}(I)$). While it can be solved easily in the transversally one-dimensional limit (all y derivatives are equal to zero), there is no analytical solution for the full, two-dimensional problem however. Thus one has to integrate (2.23) numerically in this case. A suitable algorithm for doing this is given in [31].

One of the most important features of the photorefractive nonlinearity is that it is *saturable*. This means that E_{scr}, and hence δn^2, cannot grow infinitely as $I \to \infty$ (in fact, E_{scr} is bounded by E_{ext}). As a consequence, the catastrophic self-focusing effect known from Kerr media [5] cannot occur in photorefractive media.

Due to the externally applied field the model (2.23) is inherently *anisotropic*, as it can also be seen from the single partial x derivative in the first term on the right hand side. Furthermore, it is *nonlocal* in the sense that the change of the refractive index in each point depends on the intensity distribution in the whole transverse plane.

The character of the nonlinearity is determined by the sign of E_{ext}. If $E_{ext} > 0$, the change of the refractive index δn^2 will be positive as well and increase with the light intensity. For a Gaussian beam [Figure 2.2 (a)] this leads to a higher refractive index in the center of the beam and thus to a waveguiding structure. Hence, the nonlinearity is self-focusing in this case. Due to the anisotropy, the profile of δn^2

also features two *minima* being aligned in x direction [Figure 2.2 (b)]. This is a direct consequence of the charge transport occuring mainly in this direction (i.e., parallel to $\mathbf{E}_{ext}$). At these minima, the refractive index is even *lower* than in an unperturbed (dark) crystal [30, 32].

If the sign of E_{ext} is reversed, the same follows for δn^2, and a defocusing nonlinearity is obtained. However, apart from this sign change the shape of δn^2 will be the same in both cases if a specific beam profile is given.

Sometimes it is desirable to have an explicit, *local* expression for the photorefractive nonlinearity. To this end, the (exact) solution

$$E_{scr} = -\frac{E_{ext} I + \kappa \partial_x I}{1 + I} \tag{2.24}$$

of the one-dimensional version of Eqn. (2.23) is often used in two transverse dimensions as well. This approximation correctly reproduces the saturability, but it obviously cannot describe the photorefractive anisotropy [Figure 2.2 (c)]. Thus Eqn. (2.24) is commonly known as the *isotropic model*. By contrast, we will refer to Eqn. (2.23) as the *anisotropic model*.

Though the isotropic approximation may be sufficient for fundamental investiagtions or in special cases, the anisotropic effects are not negligible in general. They have already been observed in many experiments as well [32]. Hence we will use the anisotropic model (2.23) as the standard model in this thesis and compare the results with the isotropic one if appropriate.

In homogeneous media, the diffusion effects (i.e., the terms containing κ) are known to cause a transverse displacement of the beam during the propagation. This leads to a parabolic shape of the beam trajectory (so-called *self-bending effect*) [33]. When investing the stability of solitons, this effect can usually be neglected however. This is still the case if a photonic lattice is present, provided that the lattice is strong enough to suppress the transverse displacement. Under this assumption, the diffusion effects can be treated as an additional, but negligible perturbation of the beam. We will therefore assume $T = 0\,\mathrm{K}$ ($\kappa = 0$) throughout this work.

For several reasons, it is difficult to find an appropriate and "realistic" choice for the photorefractive material parameters r_{eff} and n_0. These do not only depend on the type of the crystal and on the wavelength, but they also differ strongly between several crystals with nominally identical compositions. Additionally, the effective value of E_{ext} *inside* the crystal is not exactly known in the experiments due to screening effects at the crystal boundaries, and also E_{scr} cannot be measured directly. However, the *qualitative* features of many phenomena remain the same within a wide parameter regime, so the exact values of the parameters are not crucial for general theoretical investigations. This allows us to choose an "universal" parameter set throughout this work: If nothing else is mentioned, we assume $r_{eff} = 280\,\mathrm{pm/V}$, $n_0 = 2.35$, and $E_{ext} = 2.5\,\mathrm{kV/cm}$. These values are based on the widely used SBN75 crystals and hold for a vacuum laser wavelength of $\lambda = 532\,\mathrm{nm}$

(frequency-doubled Nd:YAG). For comparisons with experiments these values have to be fitted appropriately, whereas in the context of this work modifications of E_{ext} turn out to be sufficient. The transversal length scale is set to $w_0 = 10\,\mu$m, which yields $z_0 = 2.78\,$mm. In the following, all spatial coordinates are expressed in units of w_0 and z_0.

2.3 Photonic lattices

Within the context of this work, the term *photonic lattice* means a refractive index pattern which is *periodic* in the transverse directions, but *homogeneous* in the propagation direction of the light. Basically, there are two different methods how this can be modelled within the framework of Eqn. (2.11): On the one hand, the modulation of the refractive index can assumed to be static and prefabricated, resulting in an additive, periodic potential term. On the other hand, the lattice may be induced optically. Then the coupling between the lattice and the probe beam is realized solely by the nonlinearity. In the following we discuss both types of lattice induction.

2.3.1 Additive periodic potential

The last term of the propagation equation (2.11) containing the nonlinear shift of the refractive index $\delta n^2(I)$ can be easily generalized to include a static, periodic modulation $\delta n_p^2(\mathbf{r}_\perp)$ of n as well. Together with Eqn. (2.18) and the nonlinear coupling constant $\gamma_{nl} = k_0^2 w_0^2 n_0^4 r_{eff}$, Eqn. (2.11) then reads

$$2i\partial_z A = -\boldsymbol{\nabla}_\perp^2 A - k_0^2 w_0^2\, \delta n_p^2(\mathbf{r}_\perp) A + \gamma_{nl} E_{scr}(|A|^2) A. \tag{2.25}$$

This equation has the remarkable feature of being fully equivalent to a nonlinear Schrödinger equation with a periodic potential if a Kerr-type nonlinearity, i.e., $E_{scr}(|A|^2) = \pm|A|^2$, is chosen. Such a model describes a Bose-Einstein condensate (BEC) in the presence of an optically induced lattice [20, 34]. In this context, the Eqn. (2.25) with the substitutions $z \to t$, $\boldsymbol{\nabla}_\perp \to \boldsymbol{\nabla}$, and $\hbar = 1$ is also known as *Gross-Pitaevskii equation*. Even when a photorefractive nonlinearity is used, there are still many parallels to the BEC.

The linear version of Eqn. (2.25) (i.e., $\gamma_{nl} \equiv 0$) is well-known from standard solid state theory, where it describes an electron in a periodic potential. Bloch's theorem states that it can be solved by the ansatz $A(\mathbf{r}) = \psi_m(\mathbf{r}_\perp, \mathbf{k}_\perp) \cdot e^{i\beta_m z}$ with the so-called *Bloch functions* $\psi_m(\mathbf{r}_\perp, \mathbf{k}_\perp) = b_m(\mathbf{r}_\perp, \mathbf{k}_\perp) \cdot e^{i\mathbf{k}_\perp \cdot \mathbf{r}_\perp}$. The functions b_m have the same periodicity in ordinary space as the lattice. In our case the resulting eigenvalue problem for the b_m reads

$$\frac{1}{2}\left((\boldsymbol{\nabla}_\perp + i\mathbf{k}_\perp)^2 + k_0^2 w_0^2\, \delta n_p^2(\mathbf{r}_\perp)\right) \cdot b_m(\mathbf{r}_\perp, \mathbf{k}_\perp) = \beta_m(\mathbf{k}_\perp) b_m(\mathbf{r}_\perp, \mathbf{k}_\perp). \tag{2.26}$$

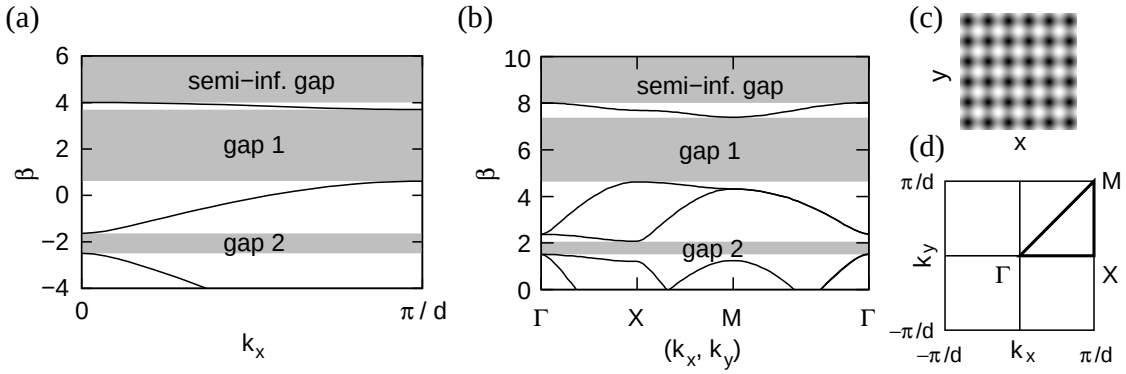

Figure 2.3: Band structure and dispresion relation (black lines) of the separable $\cos^2$ lattice [Eqns. (2.27), $V_{eff} = 0.0009$, $d = 2w_0$]. (a) 1D case; (b) 2D case; (c) 2D lattice (light gray tones denote a high refractive index) and (d) reduced part (triangle ΓXM) of the first Brillouin zone.

Herein the positive, integer number m denotes the so-called *Bloch bands* (see below), whereas $\mathbf{k}_\perp$ is restricted to the first Brillouin zone. In solid state physics, $\mathbf{k}_\perp$ is also known as *quasi-momentum*. The eigenvalues β_m are called *propagation constants*[2] of the Bloch modes ψ_m, since they can be seen as "offset corrections" to the wave vector k_z in propagation direction. Due to the sign convention in optics, they correspond to the negative electron energy in a solid state or to the negative chemical potential in the BEC model.

A common choice for δn_p^2 is

$$\text{transvers. 1-dim.:} \qquad \delta n_p^2(\mathbf{r}_\perp) = V_{eff} \cdot \cos^2(\pi x/d) \tag{2.27a}$$

$$\text{transvers. 2-dim.:} \qquad \delta n_p^2(\mathbf{r}_\perp) = \frac{V_{eff}}{2} \cdot \big(\cos^2(\pi x/d) + \cos^2(\pi y/d)\big) \tag{2.27b}$$

with the effective modulation depth V_{eff} and the lattice constant d. This has the advantage that for two transverse dimensions, the eigenvalue problem (2.26) separates in two one-dimensional ones. In general, this is not possible for more complicated lattices however.

Since the transverse coordinates x and y are expressed in units of the scaling constant w_0, the effective period of the lattice may also be changed by varying w_0 (w_0 is not subject to any restrictions). Because the δ_p^2 term in Eqn. (2.25) is weighted with w_0^2, dividing the lattice constant d by a factor u is equivalent to multiplying V_{eff} by u^2.

Figure 2.3 shows the band structure [i.e., the spectrum $\beta_m(\mathbf{k}_\perp)$] of Eqn. (2.26) in combination with the lattices (2.27a/b), both for the case of one (a) and two (b) transverse dimensions. A picture of the 2D lattice is shown in Figure 2.3 (c). Due

[2] In the following we write β without index, if we do not refer to a special Bloch band.

to the separability of Eqn. (2.26) in the 2D case, it is actually sufficient to know the dispersion relation along the lines between the Γ and the X as well as between the X and the M high symmetry points of the reduced first Brillouin zone [Figure 2.3(d)]. However, it is convention to plot closed paths in band structure diagrams.

The set of β_m is the union of several finite intervals $[\beta_m^{(min)}, \beta_m^{(max)}]$, which are called *Bloch bands* with the *band edges* $\beta_m^{(min)}$ and $\beta_m^{(max)}$. They are numbered in ascending order with decreasing β, starting with 1. If two neighboring bands do not overlap, the interval between them is called *(photonic) band gap*. The band structure of each lattice has exactly one semi-infinite gap. The finite gaps are labeled in a similar way as the bands, i.e., the first gap lies right below the semi-infinite one [Figure 2.3 (a), (b)].

The number and the width of the finite gaps increase with V_{eff}; for $V_{eff} = 0$ (homogeneous medium) there is only the semi-infinite gap. Note that the β_m are only determined up to an arbitrary, additive constant: The total wave vector in z direction is given by $k_z + \beta_z$, and there is no fixed rule for the choice of k_z in the initial separation ansatz for $\mathbf{E}(\mathbf{r}, t)$ (or, in other words, the separation of n^2 in the parts n_0^2 and δn^2 is arbitrary). Throughout this work we always choose this constant such that the semi-infinite gap reaches from 0 to $+\infty$ for $V_{eff} \to 0$.

2.3.2 Optical induction

Optically induced lattices have the great advantage that their parameters can be changed easily in the experiment. The obvious way to realize them is to launch a second beam into the crystal, which has a periodically shaped intensity profile. This so-called *lattice beam* should be incoherent with respect to the *probe beam*, but propagate in the same direction.

It has been demonstrated both theoretically and experimentally [35–38] that for this configuration stable lattices are possible within certain parameter regions. However, the nonlinear self-interaction of the lattice beam and the bidirectional interaction with the probe beam is not always desired, especially since numerical simulations show that in general the lattice becomes unstable after long propagation distances.

Efremidis et al. realized in 2002 [23] that this problems can be overcome if the polarization of the lattice beam is rotated about 90° (i.e., being parallel to the y axis). In the literature this is usually referred to as *ordinary* polarization, whereas the probe beam remains *extraordinarily* polarized. The strength of the nonlinearity *seen by the lattice beam* is then given by a different element of the linear electro-optic tensor ($r_{113} \equiv r_{13}$ instead of r_{33}). Because of $r_{13} \ll r_{33}$ in the case of SBN [cf. Eqns. (2.17) and (2.18)], the lattice beam propagates effectively in the linear regime and does not show self-interaction anymore. However, the light-induced excitation of charge carriers into the conduction band is not polarization sensitive. Thus the effective refractive index *seen by the probe beam* does not depend on the polarization

of the lattice beam[3], but the probe beam cannot influence the lattice any longer. Experimentally, this setup has proven to be rather successful [14, 25, 39–42].

The companion piece to Eqn. (2.25) reads for this case

$$2i\partial_z A = -\boldsymbol{\nabla}_\perp^2 A + \gamma_{nl} E_{scr}(I_{tot}) A, \quad I_{tot} = |A_{latt}|^2 + |A|^2 \tag{2.28}$$

with A and A_{latt} being the amplitudes of the probe and the lattice beam. The Bloch spectrum of Eqn. (2.28) can be obtained by replacing I_{tot} by $|A_{latt}|^2$ in the nonlinear term and making the same ansatz for A as in section 2.3.1. The effective modulation depth of the refractive index lattice is not given directly by the amplitude of A_{latt}, but merely by

$$V_{eff} = n_0^4 r_{eff} \left[\max\left(E_{scr}(|A_{latt}|^2)\right) - \min\left(E_{scr}(|A_{latt}|^2)\right)\right]. \tag{2.29}$$

However, this relation is monotonic in $\max(|A_{latt}|^2) - \min(|A_{latt}|^2)$ even for the anisotropic nonlinearity (2.23).

Since γ_{nl} contains a factor w_0^2, a similar argumentation as in the previous section shows that for optically induced lattices a change of the lattice constant can generally be expressed by an equivalent change of γ_{nl}. For $T = 0\,\mathrm{K}$, this can also be interpreted as a change of E_{ext}, hence in this case dividing the lattice constant d by a factor u is equivalent to multiplying E_{ext} by u^2.

In order to make the lattice homogeneous in the z direction, the lattice beam must propagate without diffraction in the linear regime, i.e., A_{latt} must be an eigenfunction of a linear propagation equation. In chapter 4.1 we will present some beam profiles which fulfill this requirement.

2.4 Gap solitons

We now look for spatial amplitude profiles $a(\mathbf{r}_\perp)$, which do not change their shape while propagating through a photorefractive crystal when a photonic lattice is present. This can be expressed by the condition

$$A(\mathbf{r}) = a(\mathbf{r}_\perp)\, e^{i\beta z}, \tag{2.30}$$

where β again denotes the propagation constant. Substituting this condition into the propagation equation (2.25), one obtaines the following equation for the soliton profile $a(\mathbf{r}_\perp)$:

$$-2\beta a + \boldsymbol{\nabla}_\perp^2 a + k_0^2 w_0^2\, \delta n_p^2(\mathbf{r}_\perp) a - \gamma_{nl} E_{scr}(|a|^2) a = 0. \tag{2.31}$$

In the case of an optically induced lattice the corresponding equation reads

$$-2\beta a + \boldsymbol{\nabla}_\perp^2 a - \gamma_{nl} E_{scr}\left(|A_{latt}|^2 + |a|^2\right) a = 0. \tag{2.32}$$

[3]Here we neglect possible differences in the photovoltaic term in Eqn. (2.20). This turns out to be a justifiable assumption in practice.

The propagation constant β is (for a given lattice and nonlinearity) the only free parameter of the soliton. Due to the complex structure of the photorefractive nonlinearity, neither Eqn. (2.31) nor Eqn. (2.32) can be solved analytically. In the appendix A it is described how this can be done numerically instead.

Since the Bloch functions $\psi_m(\mathbf{r}_\perp, \mathbf{k}_\perp)$ form a complete set of orthogonal functions, each solitary profile $a(\mathbf{r}_\perp)$ can be expressed by a superposition of them

$$a(\mathbf{r}_\perp) = \sum_{m=1}^{\infty} \int_{FBZ} c_m(\mathbf{k}_\perp)\psi_m(\mathbf{r}_\perp, \mathbf{k}_\perp)\mathrm{d}\mathbf{k}_\perp. \tag{2.33}$$

Herein the integral is taken over the first Brillouin zone (FBZ). We are interested only in spatially localized profiles fulfilling the condition $\lim_{||\mathbf{r}_\perp||\to\infty} a(\mathbf{r}_\perp) = 0$. A focusing nonlinearity thus leads to a localized increase of the refractive index, i.e., the beam induces its own waveguide. Within this waveguide, also the k_z component of the wave vector is locally increased for all ψ_m. Even if for a certain solitary superposition a the coefficients c_m may approach zero at the upper edge of a certain band, it is thus clear that the propagation constant β of the solitary superposition a must lie in the gap *above* this band (hence the name *gap soliton*[4]). For a defocusing nonlinearity this argumentation reverses, and β lies in the gap *below* the band from whose Bloch modes the soliton is constructed. A deeper discussion on the existence of gap solitons can be found in [43].

Figure 2.4 shows an one-dimensional example of both a focusing [Figure 2.4 (a), (c)] and a defocusing [Figure 2.4 (d), (f)] gap soliton. The focusing one propagates in the semi-infinte gap, whereas the defocusing one lies in the first gap. Both are *fundamental solitons*, i.e., they have a bell-shaped envelope and the lowest total intensity for a given β. Their intensity maxima coincide with a maximum of the refractive index. Hence, in analogy to solid state physics, the maxima (or focusing regions) of photonic lattices are also called *lattice sites*. The nonlinearity is given by Eqn. (2.24) with $\kappa = 0$, and the lattice is the one-dimensional, additive $\cos^2$ potential (2.27a). In two transverse dimensions the transversal cross sections of the profiles look similar.

The focusing fundamental soliton is mainly formed by Bloch modes near the upper edge of the first band. This is also intuitively clear: The further the Bloch modes have to be shifted in order to reach the gap, the more energy (or intensity) is needed. The curvature of the dispersion relation (i.e., the group velocity dispersion) is negative in the vicinity of the upper band edge [cf. Figure 2.3 (a)], indicating that the beam diameter initially increases when the profile propagates in the linear regime (normal diffraction). This is confirmed by Figure 2.4 (b): The intensity of the beam has its absolute maximum at $x = z = 0$.

[4] In some papers this term is used solely for the solitons in the *finite* gaps, whereas those in the semi-infinite gap are called *discrete solitons* instead. However, this latter name has origininally been introduced in the context of the *discrete* nonlinear Schrödinger equation, which is not subject to this thesis. Hence we avoid this term in the following and speak only of *gap solitons*.

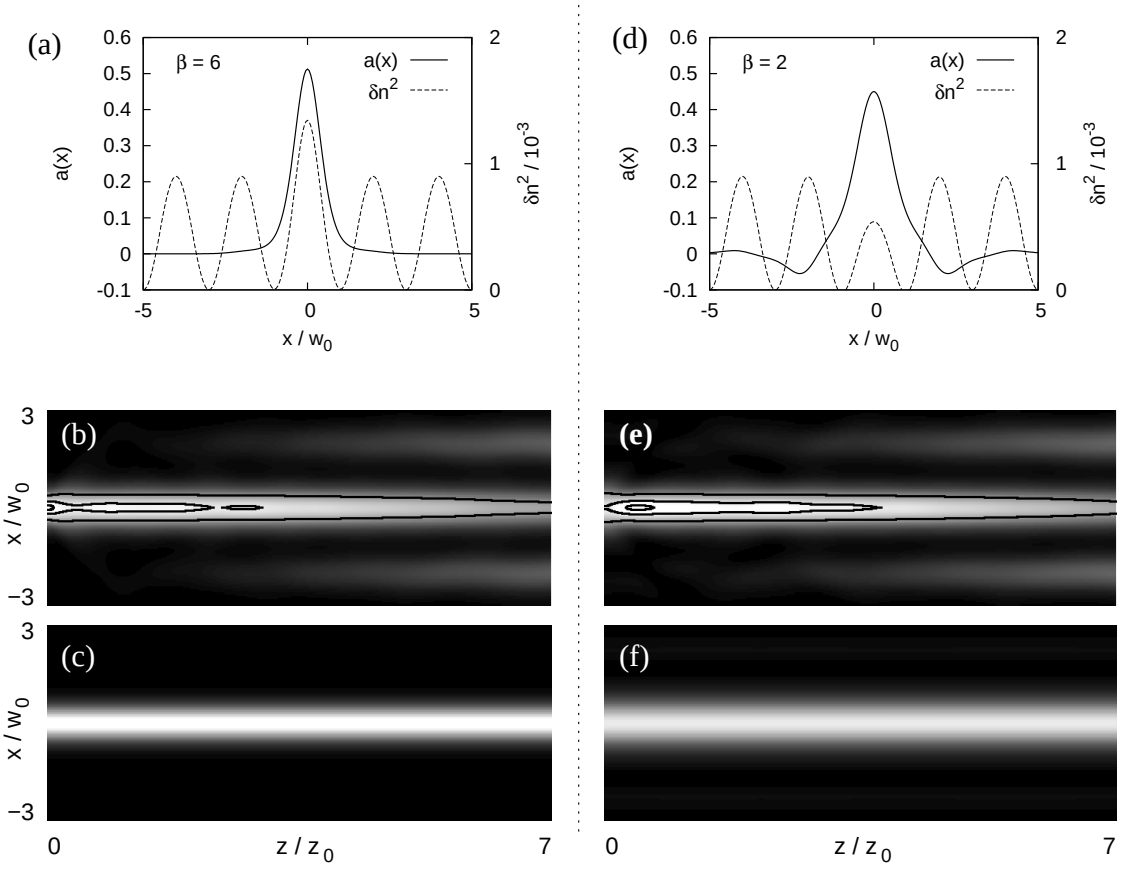

Figure 2.4: Fundamental 1D gap solitons in the separable $\cos^2$ lattice [Eqn. (2.27a), $V_{eff} = 0.0009$]. Left: focusing nonlinearity (semi-inf. gap), right: defocusing nonlinearity (first gap). (a), (d) soliton profile and effective refractive index (periodic potential and nonlinearity together); (b), (e) discrete diffraction without nonlinearity (the black lines are contour lines); (c), (f) solitary propagation. Light gray tones denote high intensities.

By constrast, the defocusing fundamental soliton arises from the Bloch modes near the lower edge of the first band, since the above-mentioned argument reverses. For these Bloch modes the dispersion relation is curved contrarily, thus in the linear regime the beam diameter should initially *decrease* (anomalous diffraction), before it increases as usual. This can be seen in the left part of Figure 2.4 (e), where the contour lines show that the beam does not reach its absolute intensity maximum until having propagated over a certain distance.

Despite many common properties, the guiding mechanisms of the two solitons are rather different: The focusing one arises solely from self-focusing effects, whereas the defocusing one could not exist without transversal Bragg reflection, such as

in homogeneous photorefractive media. This also becomes noticeable in the sign changes of the amplitude, which correspond to phase jumps of π. Such a phase profile is often called *staggered* in the literature, in contrast to the *unstaggered* phase structure of the focusing fundamental soliton.

However, it is important to note that a focusing nonlinearity does not always antagonize a negative curvature of the dispersion relation, and a defocusing nonlinearity does not always do the opposite. For example, this is not the case for multi-humped structures like soliton clusters. In this case, even for the anisotropic model the range of the nonlinearity is shorter than the distance between two contiguous intenity maxima. Thus each maximum is affected *separately* by the character of the nonlinearity, and hence such solitons may arise from different band edges compared to the example above. They exist in one-, two- and (within the BEC theory) even three-dimensional systems [44]; a detailed discussion of the 1D case can be found in [45]. We will investigate their stability properties both for additive, periodic potentials (chapter 3.2) and for optically induced lattices (chapter 4.3).

3 Stability of gap solitons in statically imprinted photonic lattices

Having seen that gap solitons may exist in nonlinear photonic structures [43], the next question arising is whether they are dynamically stable. In view of nonlinear photonic crystals, we use this term solely in a spatial sense and imply that a temporal steady state has been reached. Thus instabilities may occur only as spatial deviations from the solitary profile, which arise after some propagation distance z. However, in the context of BEC this picture is translated back into the temporal domain, since the spatial propagation of an optical beam corresponds to the temporal evolution of the condensate.

Instabilities of gap solitons have been treated in several publications in the past, both using numerical techniques alone [19, 46] and combining them with analytical methods [47, 48]. In doing so, a link between instabilities and resonances in the Bloch bands caused by the internal modes of the solitons has been revealed. In the context of BEC also the effects of a time-periodic modulation of the lattice have been investigated [46].

However, all these works consider only a fixed value for the strength (or modulation depth) V_{eff} of the photonic lattice. Since the size of the band gaps increases with V_{eff}, intuition suggests that for deeper lattices gap solitons should be stable in a larger parameter regime. This is especially clear since in the limit $V_{eff} \to \infty$ the nonlinearity becomes negligible, and the gap solitons degenerate to linear eigenmodes of the waveguides induced by the lattice. By contrast, the solitons in the finite gaps should become unstable for small values of V_{eff}.

In order to study these dependencies systematically for intermediate lattice strengths, we follow [49] and choose the one-dimensional version of the system (2.25) as the starting point, thus implying an additive periodic potential. This has several advantages: The strengths of both the lattice (V_{eff}) and the nonlinearity (E_{ext} and γ_{nl}, respectively) are not bounded and can be varied independently. This holds for the sign of the nonlinearity as well, so focusing and defocusing media can be directly compared without changing the band structure. Additionally, this system is closely related to the Gross-Pitaevskii equation, so the fundamental results can be transferred easily.

We subsequently discuss how far the 1D results also hold in two transverse dimensions. In this context we use the anisotropic model, though this chapter is dedicated to statically imprinted lattices. However, this allows us to study some of the inherently anisotropic effects while keeping the possibility of easily comparing focusing and defocusing media. The experimentally more relevant case of optical lattice induction in photorefractive crystals is covered from chapter 4 onward.

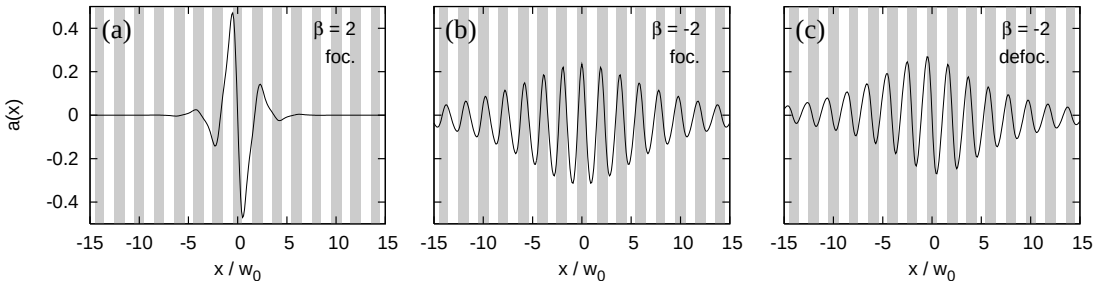

Figure 3.1: Basic gap solitons in the higher-order gaps of the separable $\cos^2$ lattice [Eqn. (2.27a), $V_{eff} = 0.0009$, $d = 2w_0$]. (a) first gap, focusing nonlinearity; (b) second gap, focusing nonlinearity; (c) second gap, defocusing nonlinearity. The gray bars are centered around the maxima of δn_p^2.

3.1 Basic (lowest-intensity) gap solitons

Among the large number of possible solitons in each gap, those with the lowest total intensity (or energy) are outstanding. If they are unstable, they cannot decay into other, "simpler" solitons *within the same gap*. Hence we will call them *basic solitons* in the following.

In the lowest accessible gaps (i.e., the semi-infinite one for focusing and the first one for defocusing media), the basic solitons are the fundamental ones depicted in the Figures 2.4 (a) and (d). As already explained in chapter 2.4, these are always nodeless in focusing media, whereas their phase profile is staggered in defocusing media.

By contrast, the basic solitons in the higher-order gaps are not bell-shaped. Their profiles are determined by the shape of the Bloch modes at the respective band edges. In the quantum mechanical interpretation they form excited states, while the fundamental solitons correspond to ground states.

For focusing media, the symmetry of the basic solitons is odd within the first gap and even within the second gap [Figures 3.1 (a) and (b)]. For defocusing media the same holds – due to the contrary shift of β – for the second [Figure 3.1 (c)] and the third gap (not shown here). It can be seen that the transverse oscillation period of the solitons decreases with increasing gap numbers. This is because the Bloch modes from higher bands are associated with higher k values (cf. section 2.3.1 and the reduced band scheme in Figure 2.3). Figure 3.1 also shows, that the soliton profiles become the broader the narrower the gap is. For stronger lattices, the solitons in the second and possibly existing higher order gaps are sharply localized as well.

For convenience, we introduce the shortcuts $B_n^{(foc)}$ for the focusing and $B_n^{(def)}$ for the defocusing basic solitons in the n-th gap. At this the index '0' denotes

the semi-infinite gap[1]. If the upper index is omitted, we refer to both kinds of nonlinearities.

3.1.1 Linear stability analysis

In several cases the stability of solitons can be proven analytically. In 1973 Vakhitov and Kolokolov derived a criterion which states that a soliton is stable if its total intensity increases strictly monotonically with the propagation constant β [50, 51]. Though this criterion is convenient to use, its (strict) validity is restricted to nodeless soliton profiles. Thus in our case it is applicable only to focusing fundamental solitons in the semi-infinite gap, where it states that these are stable.

For the basic solitons in other gaps or in defocusing media, we have to make a general linear stability ansatz. For that purpose we consider the evolution of a solitary solution $a(x)$ in the presence of the small, complex-valued perturbations $v(x)$ and $w(x)$ ($\varepsilon \ll 1$) [48]:

$$A(x,z) = e^{i\beta z}\left(a(x) + \varepsilon\left[(v(x)+iw(x))e^{\lambda z} + (v^*(x)+iw^*(x))e^{\lambda^* z}\right]\right). \tag{3.1}$$

By inserting this ansatz into the propagation equation (2.25), the following linear eigenvalue problem is obtained:

$$\begin{aligned} \lambda v &= -\mathcal{L}w \\ \lambda w &= \mathcal{L}v - \gamma_{nl}\partial_I E_{scr}(I)a^2\, v, \quad I = |a|^2 \end{aligned} \tag{3.2}$$

with

$$\mathcal{L} \equiv -\beta + \frac{1}{2}\boldsymbol{\nabla}_\perp^2 + \frac{k_0^2 w_0^2}{2}\delta n_p^2(x) - \frac{\gamma_{nl}}{2}E_{scr}(|a|^2). \tag{3.3}$$

Herein the imaginary part of the eigenvalue λ describes the shifted propagation constants of the perturbation modes v and w, while their growth rate is given by the real part. In general, the problem (3.2) can be solved only numerically however. This requires large grids since the unstable eigenmodes have very long oscillating tails.

The equations (3.1-3.3) can be easily generalized to two transverse dimensions. Since in this case the required computing power increases drastically, it may be advisable to transform Eqn. (3.2) into the Bloch space [52]. The size of the numerical problem can then be reduced significantly by restricting the Bloch basis to the modes of the lowest-order bands. This still leads to good approximations of the unstable eigenmodes in several cases. As a minimum, at least $n+1$ bands should be considered in the reduced basis, if the soliton is mainly formed by the Bloch modes of the n-th band.

Solving the problem (3.2) requires in all cases the knowledge of the partial derivative of the nonlinearity with respect to the intensity I. Even numerically this derivative may be calculated only if the function E_{nl} is local, i.e., a point-wise mapping

[1] In [46], the $B_2^{(def)}$ solitons are also called *subfundamental solitons*.

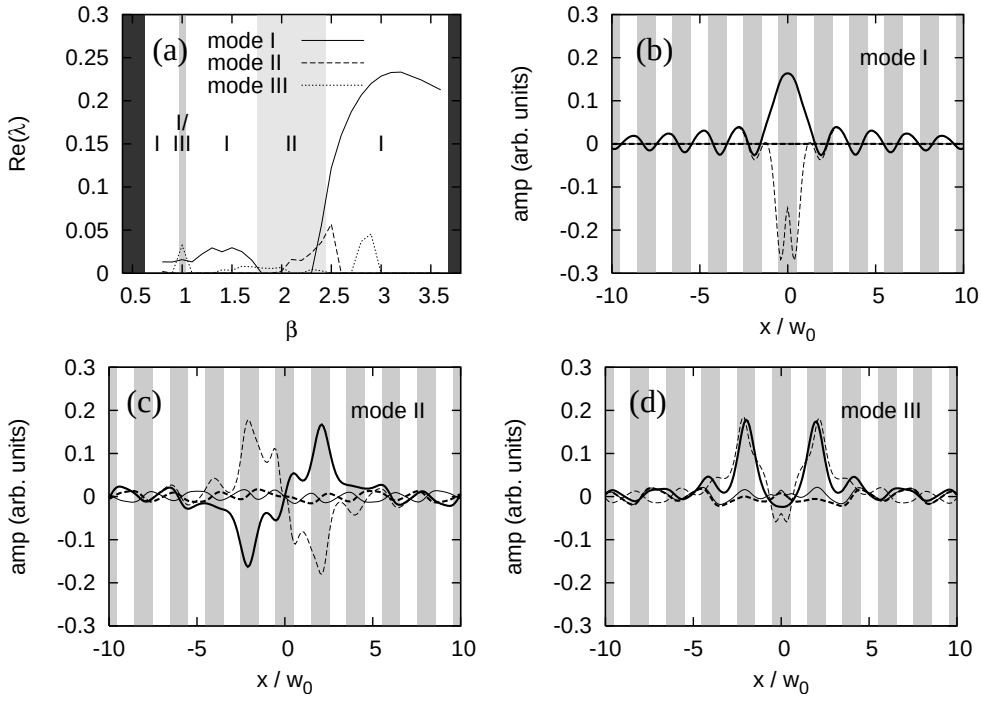

Figure 3.2: Linear stability analysis of the $B_1^{(foc)}$ solitons [$V_{eff} = 0.0009$ ($d = 2w_0$), cf. Figure 3.1 (a)]: (a) real parts of the eigenvalues for the three dominating unstable eigenmodes; the numbers in the shaded bars indicate the modes which cause the decay of the soliton in the numerical simulations; (b)-(d) real (—) and imaginary (- -) parts of v (thick lines) and w (thin lines) for the modes from (a). The gray bars in (b)-(d) mark the maxima of δn_p^2.

$(x[, y]) \mapsto E_{nl}(x[, y])$. This is not the case for the anisotropic model (2.23) however, so one either has to go back to the isotropic approximation (2.24) or to switch to direct simulations of the soliton propagation in this case. Because the focus of this work lies on the anisotropic model, we will use the second possibility as the standard method for investigating soliton instabilies in two transverse dimensions. However, in the 1D case this problem does not occur, so both methods may be compared. In order to do this we continue with the 1D application of (3.1-3.3).

Figure 3.2 shows the results for the $B_1^{(foc)}$ solitons [cf. Figure 3.1 (a)] in combination with a medium lattice strength ($V_{eff} = 0.0009$). There are three dominating eigenmodes, a single-peaked fundamental one [mode I, Figure 3.2 (b)] and both a symmetric and an antisymmetric double-peaked one [modes II and III, 3.2 (c) and (d)]. The plot of the corresponding real parts of λ [Figure 3.2 (a)] shows that for each value of β at least one of them is growing exponentially.

Hence these results suggest that for this parameters the basic solitons in the first

gap are always unstable. The instabilities seem to arise mainly from the symmetric mode I, except for the interval $1.8 \lesssim \beta \lesssim 2.4$ and a small region around $\beta = 1$, where the growth rates of the modes II and III are higher. However, one has to bear in mind that the accuracy of this stability analysis is low within regions of very weak instabilities (i.e., $\mathrm{Re}(\lambda) \ll 1$), which is obtained e.g. around $\beta = 2$. This is a consequence of the special symmetry of the system (3.2): The two eigenvalue equations can be rewritten as a single one containing only λ^2

$$\lambda^2 v = -\mathcal{L}^2 v + \gamma_{nl} \mathcal{L} \partial_I E_{scr}(I) a^2 \, v. \tag{3.4}$$

Thus all eigenmodes with $\mathrm{Re}(\lambda) \neq 0$ are actually linearly unstable since they occur twice, and once with $\mathrm{Re}(\lambda) > 0$. This means that we cannot find stable gap solitons with this analysis alone, since the spatial evolution of the modes with $\mathrm{Re}(\lambda) = 0$ would only be described by a nonlinear stability analysis. In combination with the poor spatial localization of the eigenmodes, the numerical accuracy is also restricted in the vicinity of zero.

3.1.2 1D numerical simulations

Due to the shortcomings of the linear stability analysis, we check the results of the previous section by numerically integrating the propagation equation (2.25). This has the additional advantage that also information about the soliton decay itself is gained. In doing so the wide-ranging tails of the unstable eigenmodes require special care again: In order to avoid artefacts arising from the finite numerical grid, highly absorbing boundary conditions are required. The algorithm used here is based on [53], it is described in more details in the appendix B.

In order to provide a better comparison with the linear stability analysis, the results obtained by the direct simulations of the soliton propagation are displayed in Figure 3.2 (a) as shaded vertical bars. The numbers inside these bars indicate the domains in which the respective eigenmode(s) actually govern the decay of the soliton. It is confirmed that the $B_1^{(foc)}$ solitons are always unstable for $V_{eff} = 0.0009$.

The unstable domain ($\beta \lesssim 1.7$ or $\beta \gtrsim 2.4$) of the fundamental mode I coincides quite well with the intervals predicted by the linear stability analysis. However, the simulations unveil that the antisymmetric mode II is always the leading unstable eigenmode in the range $1.7 \lesssim \beta \lesssim 2.4$, while the influence of the double-peaked symmetric mode III remains secondary. This indicates that especially for $1.7 \lesssim \beta \lesssim 2.0$ the accuracy of the stability analysis is too low due to the reasons mentioned above. The growth rate of the mode III becomes comparable to those of the mode I only within a small interval around $\beta = 1$.

The soliton decay due to the fundamental mode I is shown in the Figures 3.3 (a) and (b) for $\beta = 1.5$. Since the instability is weak, the soliton propagates seemingly undisturbed for $z \lesssim 200 z_0$. Thereafter a slight, alternating pulsing of the peak

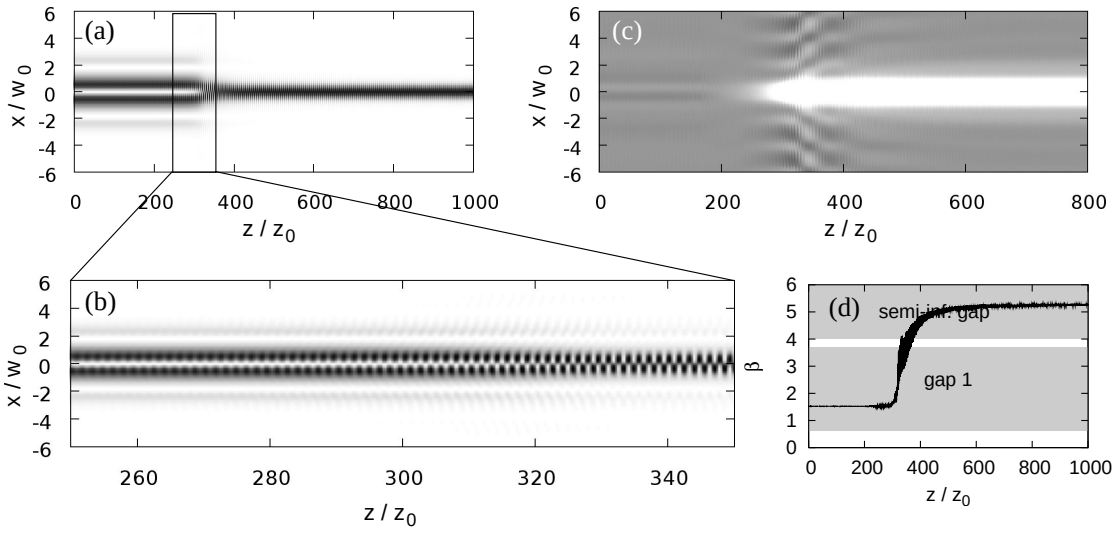

Figure 3.3: Decay of the $B_1^{(foc)}$ soliton with $\beta = 1.5$ [first gap, cf. Figure 3.1 (a)] due to the symmetric eigenmode from Figure 3.2 (b):
(a) spatial evolution of the intensity distribution; (b) detailed view of the decay; (c) amplitude deviation from the initial soliton profile; (d) evolution of the mean propagation constant. Dark (light) gray tones indicate high (low) intensities in (a) and (b) and negative (positive) amplitudes in (c).

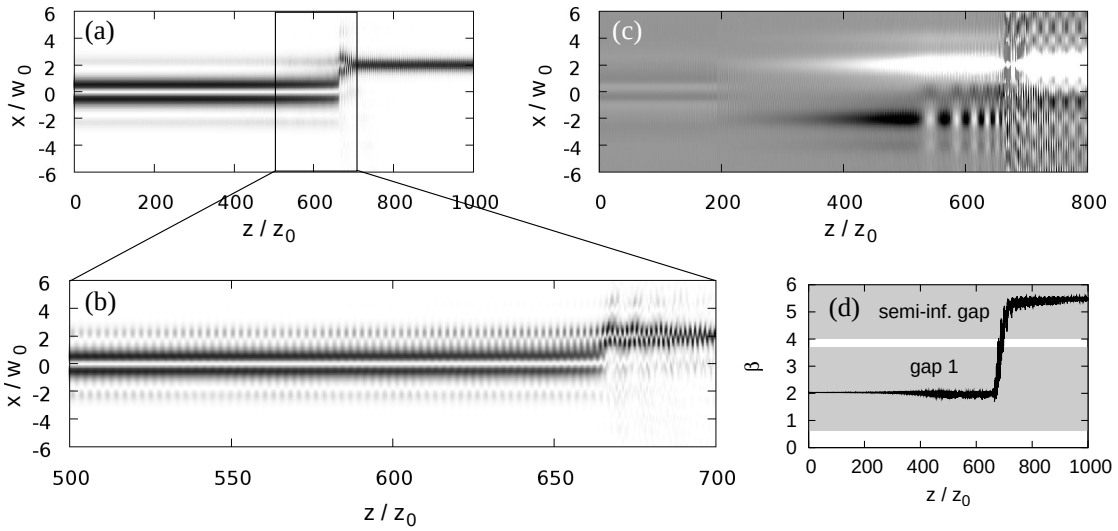

Figure 3.4: Decay of the $B_1^{(foc)}$ soliton with $\beta = 2.0$ [first gap, cf. Figure 3.1 (a)] due to the eigenmodes II (dominating) and III from Figure 3.2 (c) and (d). The meaning of (a)-(d) is the same as in Figure 3.3.

intensities becomes visible. This is the signature of a symmetry break: Whereas the unstable eigenmode is symmetric, the *amplitude* profile of the soliton [Figure 3.1 (a)] is antisymmetric (however, the intensity profiles of both are symmetric!). The pulsing increases until the beam has lost a considerable amount of intensity by diffraction and consists merely of a single peak now, which is strongly oscillating around the center of the corresponding lattice site. While these oscillations slowly decay, the final state is reached and the beam looks like a fundamental soliton. This is confirmed by the propagation constant β, which indeed is shifted from the first gap into the semi-infinite one during the decay [Figure 3.3 (d)].

The "effective" unstable eigenmode can also be obtained numerically in each propagation step by orthogonally projecting the current amplitude profile onto the initial soliton profile. This is shown in Figure 3.3 (c), corroborating that the decay indeed is triggered by the fundamental mode I.

Figure 3.4 shows in a similar manner the decay governed by the mode II ($\beta = 2.0$). In this case both the soliton [Figure 3.1 (a)] and the dominating unstable eigenmode have an *antisymmetric* amplitude profile. Hence the intensity profile of the beam maintains its symmetry even after the instability has set in [Figure 3.4 (a), (b) for $z \approx 500 z_0$]. However, a symmetry break still occurs at $z \approx 530 z_0$ when the double-peaked *symmetric* mode III becomes excited too [alternating negative/positive (black/white) amplitudes at $x = -2w_0$ in 3.4 (c)]. At first this becomes manifest in an increased spatial oscillation period of the intensity on *one* side of the beam (in the example shown here, it is the one associated with the positive x values, but it might be the other one as well). Subsequently the total intensity on this side slowly increases, until the major part of the beam suddenly jumps ($z = 675 z_0$) onto the neighboring lattice site ($x = +2w_0$). The direction of this jump is determined by the direction of the previous intensity shift. After the jump the spatial oscillations of the beam decay, and its profile takes the form of a fundamental soliton as in the previous case. Again, the propagation constant is shifted into the semi-infinite gap. The successive excitation of *both* unstable eigenmodes II and III is also clearly visible in Figure 3.4 (c): Since their propagation constants differ, the sign of their (nonlinear) superposition periodically changes on one side of the beam (here at $x = +2w_0$ for $530 z_0 \lesssim z \lesssim 675 z_0$).

The absolute values of z mentioned in the above discussions depend on the initial deviation of the beam from the exact soliton profile due to discretization errors. Nevertheless, the different growth rates of the respective unstable eigenmodes are still obvious: While both in Figure 3.3 and in Figure 3.4 the decay sets in at $z \approx 200 z_0$, it is almost finished at $z = 400 z_0$ for the mode I instability, but it lasts until $z \gtrsim 700 z_0$ for the mode II instability. This is in accordance with the linear stability analysis [Figure 3.2 (a)], which states that the growth rates are much smaller for $\beta = 2.0$ (even beyond the resolution limit) than those for $\beta = 1.5$.

As it has been shown in [48], the instabilities oberved here coincides with *resonances* in the Bloch bands. These may occur when the "effective" propagation

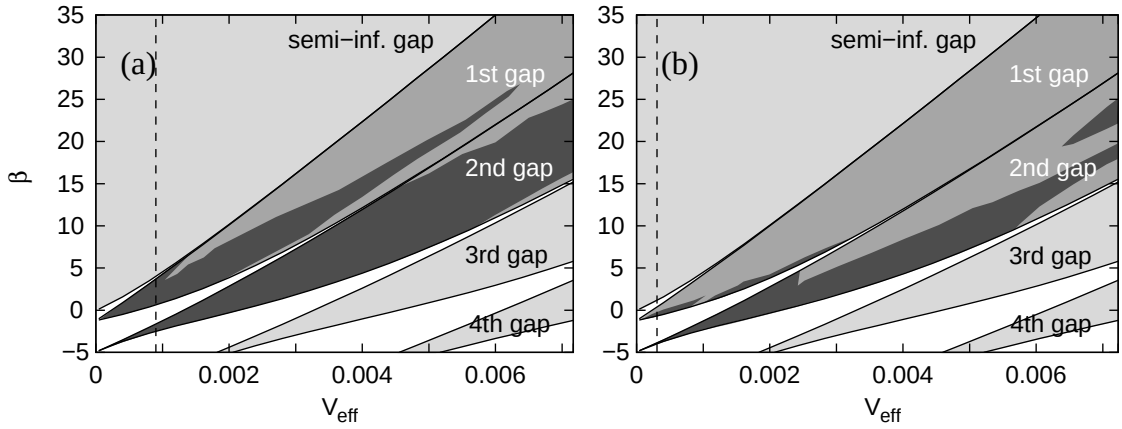

Figure 3.5: Stability vs. lattice depth ($d = 2w_0$) for the basic solitons in the first two gaps: (a) self-focusing, (b) self-defocusing nonlinearity. Shadings: light gray: band gaps, medium gray: stable basic solitons, dark gray: unstable basic solitons. Dashed lines: potential depths from (a) Figures 3.1–3.4 and (b) Figure 3.6.

constant $\beta \pm \mathrm{Im}\lambda$ of at least one eigenmode of the system (3.2) lies within a Bloch band. Since the Bloch bands become narrower for stronger lattices, it seems to be obvious that gap solitons should become stable if the depth of the lattice is high enough. In order to investigate this in detail, the stability analysis and the simulations are repeated for different lattice depths V_{eff}. Following the argumentation in section 2.3.1, this can be reinterpreted as modifying the lattice constant d, hence it is sufficient to vary V_{eff} alone.

The result of this analysis for the first two finite gaps is shown in Figure 3.5 (a) for the focusing and in Figure 3.5 (b) for the defocusing nonlinearity.

The $B_1^{(foc)}$ solitons are unstable for $V_{eff} \lesssim 0.001$. For higher values of V_{eff}, at first those solitons lying in a certain interval close to the *upper* edge of the gap (i.e., those with a high total intensity) become stable. For $V_{eff} \gtrsim 0.002$, another interval of stable solitons arises from the *lower* edge. Now the instabilies are solely caused by resonances in the *third* Bloch band, thus the stable intervals grow with increasing lattice strengths in the same way as this band becomes smaller. At $V_{eff} \approx 0.0064$ they finally merge, and the $B_1^{(foc)}$ solitons become stable throughout the first gap.

For the largest part of the unstable region in the first gap [Figure 3.5 (a)], the soliton decays are governed by the unstable eigenmode I [cf. Figure 3.2 (b)]. The decay via the double-peaked modes II and III occurs only in a certain interval (i.e., approximately for $V_{eff} = 0.0009 \pm 0.0003$) around the dashed line indicating the lattice depth used in the discussions above.

Interestingly the situation is different for self-defocusing media: The $B_1^{(def)}$ soli-

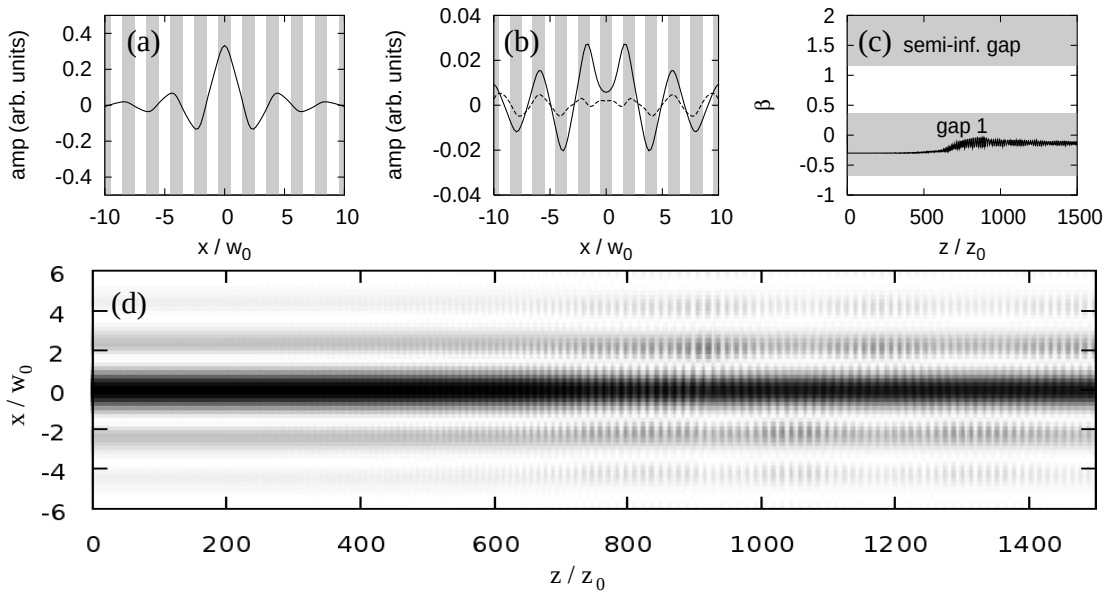

Figure 3.6: Instability of the $B_1^{(def)}$ soliton with $\beta = -0.3$ and $V_{eff} = 0.0003$ ($d = 2w_0$): (a) soliton profile, the gray bars in mark the maxima of δn_p^2; (b) real (–) and imaginary (- -) part of the dominating unstable eigenmode; (c) spatial evolution of the mean propagation constant; (d) view of the decay. Dark gray tones in (d) indicate high intensities.

tons are stable down to very weak lattices ($V_{eff} \approx 0.0001$ and lower). Instabilities occur only in a small range near the lower gap edge (i.e., for solitons with a high total intensity). They finally disappear for $V_{eff} \gtrsim 0.0032$, when the second Bloch band has become small. In contrast to self-focusing media, the unstable regions are very small and resonances in the third band do not seem to occur.

Figure 3.6 shows an unstable $B_1^{(def)}$ soliton with $\beta = -0.3$ and $V_{eff} = 0.0003$. Compared to the focusing case (Figures 3.3 and 3.4), the instability is rather weak. The lattice depth even had to be lowered in order to make it visible at all. The dominating unstable eigenmode is symmetric and leads to intensity oscillations, but the structure of the soliton is *not* destroyed. The propagation constant remains in the first gap, but is shifted into the stable region as the beam radiates some intensity. This seems to be the only kind of instability ocurring in the first gap.

Hence the $B_1^{(def)}$ and the $B_0^{(foc)}$ solitons do not only have the same symmetry (cf. Figure 2.4), but they also show a very similar stability behavior. This "shifted analogy" is somewhat less surprising if one bears in mind that opposite nonlinearities also cause opposite shifts of the propagation constants. Thus the constituting Bloch modes stem from opposite edges of the *same* band. However, the different characters of the nonlinearities also play an important role, so this analogy is not

perfect: The the $B_0^{(foc)}$ solitons are stable within the complete semi-infinite gap, hence the (small) unstable domains of the the $B_1^{(def)}$ solitons [Figure 3.5 (b)] do not have any counterpart. The physical reason for their occurence is that in defocusing media bright solitons cannot exist without a photonic lattice. Therefore they necessarily become unstable, if this lattice is too weak.

One can try to generalize this comparison to the higher order gaps. Regarding size and shape of the unstable regions, Figure 3.5 indeed shows also some similarities between the antisymmetric $B_1^{(foc)}$ and $B_2^{(def)}$ solitons. For both kinds of nonlinearities, they are unstable below a certain lattice strength ($V_{eff} \approx 0.001$ for focusing and $V_{eff} \approx 0.0024$ for defocusing media; the simulations in [46] were carried out below this threshold). At this point a stable interval bifurcates from the upper edge of the respective gaps. For even stronger lattices ($V_{eff} > 0.002$ for focusing and $V_{eff} > 0.0057$ for defocusing media), also the solitons near the lower gap edges become stable. By contrast, the stability thresholds regarding V_{eff} are significantly higher for the $B_2^{(foc)}$ solitons (these are symmetric again).

However, the significance of such comparisons between adjacent gaps is always restricted due to their different size and position in the band-gap spectrum. Since the higher-order gaps are smaller, the variety of possible resonances in the surrounding Bloch bands is bigger. For high potential depths $|\mathrm{Im}(\lambda)|$ may become large, thus others than the adjoining bands have to be considered as well. Hence for a given value of V_{eff}, the stable intervals shrink with an increasing gap order. This effect can be observed in Figure 3.5 (b), where even at $V_{eff} \approx 0.0065$ a new unstable interval begins in the second gap. This happens due to resonances in the fourth Bloch band which still has a considerable width at this lattice strength. By contrast, these do not play a role in the first gap of a focusing medium [Figure 3.5 (a)], so the $B_1^{(foc)}$ solitons are stable throughout the first gap for $V_{eff} \gtrsim 0.0064$.

The decay of the (antisymmetric) unstable $B_2^{(def)}$ solitons is similar to that of the $B_1^{(foc)}$ solitons. The dominating unstable eigenmode is symmetric, and the final state is a slightly oscillating $B_1^{(def)}$ soliton, i.e., the propagation constant is shifted from the decond into the first gap.

The decay of the (symmetric) unstable $B_2^{(foc)}$ solitons is commonly a two-stage process: The first stage is triggered by an antisymmetric unstable eigenmode and leads to an intermediate state in the form of a (likewise antisymmetric) $B_1^{(foc)}$ soliton. But in contrast to the eigenmode shown in Figure 3.2 (c), the maxima of the one occurring here lie closer together, i.e., they do not coincide with the adjacent lattice sites. For low to medium lattice strengths ($V_{eff} \lesssim 0.004$) the $B_1^{(foc)}$ soliton is unstable as well, and a succeeding decay into a stable, but again slightly oscillating $B_0^{(foc)}$ soliton takes place. This second decay is comparable to the one shown in Figure 3.3.

However, for stronger lattices the intermediate $B_1^{(foc)}$ soliton may be stable, so that the decay just ends there. This can be understood by looking at Figure 3.5 (a)

again, where it is shown that for $V_{eff} > 0.004$ the unstable intervals of the $B_1^{(foc)}$ solitons indeed become small compared to the width of the first gap.

For certain combinations of V_{eff} and β it is also possible that the growth rate of the symmetric unstable eigenmode exceeds those of the antisymmetric one right from the start. In this case both stages merge, and the initial $B_2^{(foc)}$ soliton directly decays into a $B_0^{(foc)}$ one.

3.1.3 2D numerical simulations

Having studied the stability of one-dimensional basic solitons so far, we now switch to systems with two transverse dimensions. We start again with a focusing nonlinearity. Analogous to the 1D case, the $B_0^{(foc)}$ solitons are nodeless and thus their stability may be proven using the Vakhitov-Kolokolov criterion. Hence we begin our discussion with the $B_1^{(foc)}$ solitons.

As it can be seen from the Figures 3.7 (a) and (c), they basically constitute the simplest possible, spatially localized 2D extensions of the corresponding 1D solitons. Their profiles are antisymmetric in one direction, whereas they look like fundamental solitons in the other one, thus forming horizontally or vertically oriented excited states. The characteristic signature of finite-gap solitons – the alternating (or staggered) phase – occurs only in the first direction, so only there the beams are guided due to Bragg reflection. The constituting Bloch modes arise from the X symmetry points [Figure 2.3 (d)].

As a consequence of the anisotropy, vertically and horizontally antisymmetric solitons have to be distinguished. The total intensity of the latter is slightly higher due to the special structure of the electric screening field along the c axis [30, 32]. Thus only the *vertically* antisymmetric profiles represent basic solitons. Nevertheless the similarities to the horizontally antisymmetric ones are large, so we discuss both cases in the following. For convenience, we extend the definition of the shortcut $B_n^{(foc)}$ and speak of *vertical* or *horizontal* $B_1^{(foc)}$ solitons, if we refer to the lowest-intensity solitons with the respective orientations.

Figure 3.7 shows both the propagation [(a)-(f)] and the dominating unstable eigenmodes [(g)-(j)] of the two-dimensional $B_1^{(foc)}$ solitons. Since the linear stability analysis presented in section 3.1.1 cannot be applied to the anisotropic model used here, the unstable eigenmodes have to be calculated numerically by orthogonally projecting the amplitude profile obtained at the onset of the instability onto the initial soliton profile.

It can be seen that both the horizontal and the vertical $B_1^{(foc)}$ soliton decay due to a slowly growing, fundamental eigenmode. Consequently, when viewed in the y-z or x-z plane [Figures 3.7 (e) and (f)], their decay has many similarities with Figure 3.3 (b). It also starts with a slowly increasing, alternating pulsing due to the symmetry breaking and it ends up with a slightly oscillating fundamental solitary mode in the semi-infinite gap [Figures 3.7 (b) and (d)]. This kind of decay seems

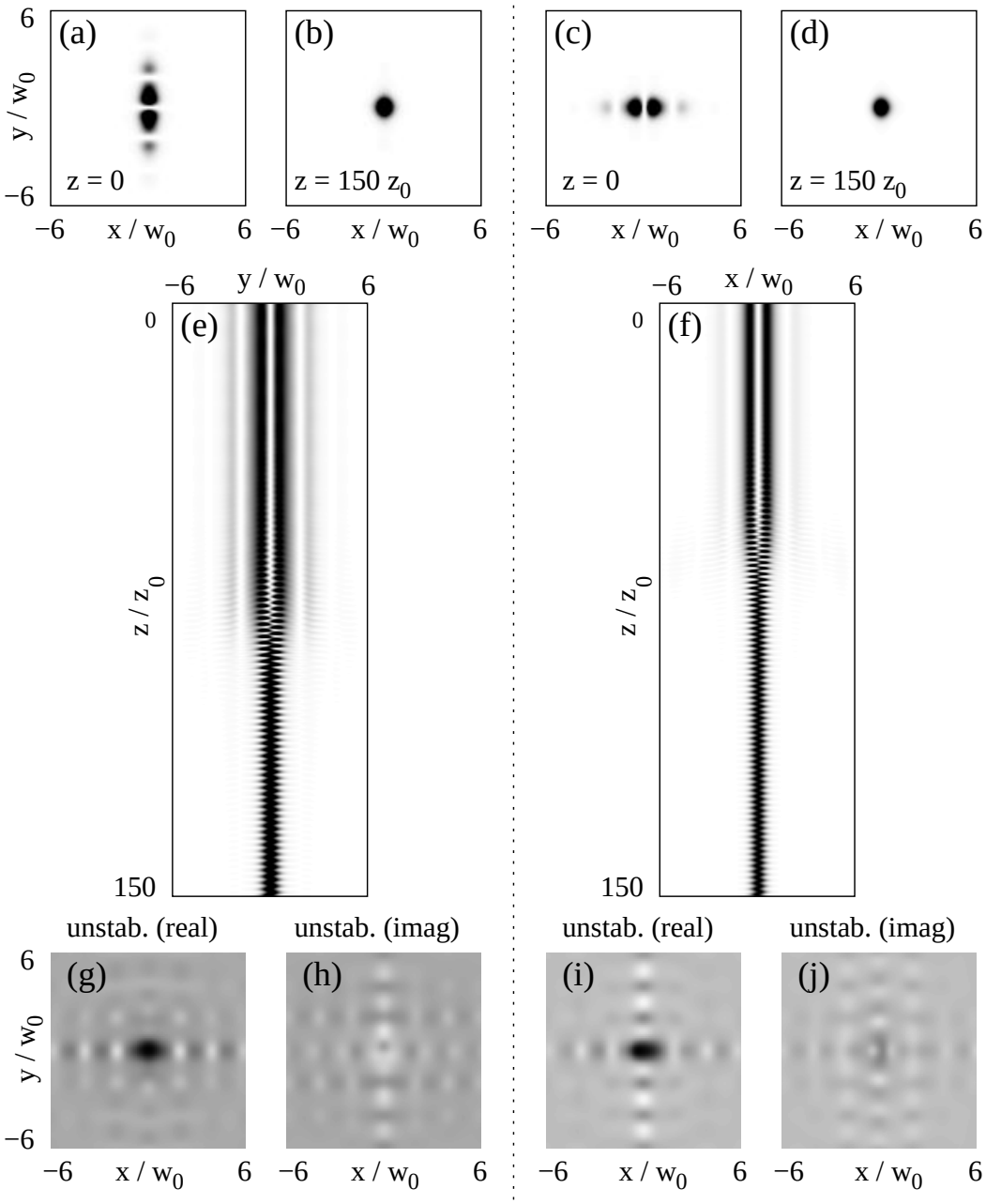

Figure 3.7: Decay of the 2D $B_1^{(foc)}$ solitons with $\beta = 5.5$ and $V_{eff} = 0.0018$ ($d = 2w_0$) for the anisotropic photorefractive nonlinearity. Top: intensity profiles before [(a), (c)] and after [(b), (d)] the decay; middle: cross-sections [(e) y-z plane and (f) x-z plane, respectively]; bottom: real [(g), (i)] and imaginary [(h), (j)] parts of the dominating unstable eigenmodes. Dark (light) gray tones indicate high (low) intensities (a)-(f) or positive (negative) amplitudes (g)-(j).

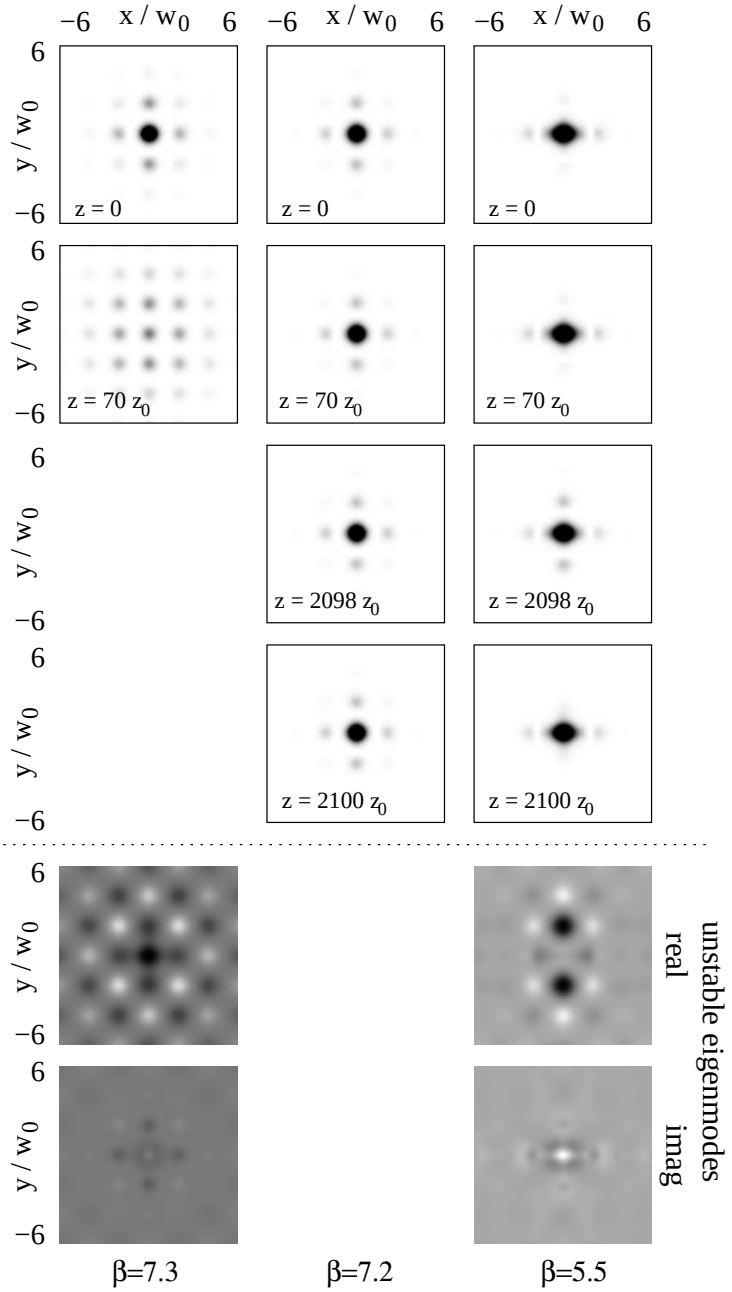

Figure 3.8: Propagation of the 2D $B_1^{(def)}$ solitons for three different values of β (7.3, 7.2 and 5.5) and $V_{eff} = 0.0018$ ($d = 2w_0$) using the anisotropic photorefractive nonlinearity. Upper part: Spatial evolution of the intensity profiles; lower part: dominating unstable eigenmodes. The mode shown in the middle column is stable. Dark (light) gray tones indicate high (low) intensities (upper part) or positive (negative) amplitudes (lower part).

to be the only one occurring for the 2D $B_1^{(foc)}$ solitons. The growth rates of the instabilities are generally higher than those observed in the 1D system.

Apparently, the decay of the vertically antisymmetric solitons sets in a little later. This holds independently of β for the given lattice depth ($V_{eff} = 0.0018$). However, for stronger lattices the situation may be the other way round, when the resonances causing the instabilities are just about to disappear.

For strong lattices ($V_{eff} \gtrsim 0.004$), the vertical $B_1^{(foc)}$ solitons become stable within a small interval near the *upper* edge of the first gap. Stable *horizontal* $B_1^{(foc)}$ solitons require even higher values of V_{eff}, though they show already at $V_{eff} \approx 0.004$ very long, quasi-stable transients for β lying in the *lower* part of the first gap. For the isotropic nonlinearity [equation (2.24)], stable intervals start to occur at similar lattice strengths. In all cases, the stable intervals remain small even at very high lattice strengths.

Like in the 1D system, stable $B_1^{(def)}$ solitons do not require such strong lattices. For $V_{eff} = 0.0018$ (same value as in Figure 3.7), instabilities are observed only for very low (left column of Figure 3.8) and for very high (right column of Fig. 3.8). The latter also occur in the 1D case (cf. Figure 3.6): The structure of the soliton is not destroyed, but starts to oscillate, and the propagation constant is shifted towards the stable region. Due to the anisotropy the oscillation takes place in the y-direction, i.e., the upper and the lower spot appear and disappear periodically (cf. the pictures at $z = 2098z_0$ and $z = 2100z_0$ in the right column of Figure 3.8). Consequently, the real part of the corresponding unstable eigenmode has two maxima at $y = \pm 2w_0$.

However, the instability near the upper egde of the first gap [left column of Figure 3.8, see also Figure 2.3 (b)] seems to occur only in the 2D case. It has also been reported for media with a Kerr-type nonlinearity [52]. In contrast to all other instabilities we have discussed so far, this one is of a non-oscillatory type and does not lead to the formation of a new, stable soliton. The beam is rather diffracted strongly after a certain propagation distance. A slight increment of the soliton intensity (that means, raising the propagation constant a little) is sufficient to stabilize the structure, as shown in the middle column of Figure 3.8.

The phenomena being discussed in this chapter do not crucially depend on the absolute value of the nonlinear coupling constant γ_{nl} (of course it must not be too small). The main results may also be transferred to different nonlinearities of similar shape as long as the refractive index essentially changes monotonically with the intensity (i.e., nonlocal effects must not be too strong). This especially holds for the Kerr nonlinearity, though the instabilities of the non-fundamental basic solitons (as, e.g., the $B_1^{(foc)}$ ones) are much more pronounced in the 2D case (larger growth rates, no stable regions up to very high lattice strengths). However, the catastrophic self-focusing may be suppressed by the lattice.

3.2 Soliton clusters

Up to now we considered only the spatial dynamics of single gap solitons. In the following we investigate the stability of structures which are made up of *multiple* fundamental solitons. At this we assume that the structure itself forms a solitary solution, where all intensity maxima coincide with lattice sites. Such a structure is commonly known as *soliton cluster*, whereas the constituting fundamental solitons are called *lobes* or *spots*.

3.2.1 Amplitude profiles

In this section we restrict our analysis to cases where either all lobes are in phase or adjacent lobes are separated by phase jumps of π. Examples of such clusters with 9 lobes are shown in Figure 3.9, both for a focusing and for a defocusing anisotropic nonlinearity. These solutions are two-dimensional versions of the truncated nonlinear Bloch waves presented in [45]. This name reflects the fact that their profiles can qualitatively be regarded as parts of Bloch waves, which are exponentially damped at the boundaries of the cluster. At this the Bloch waves may be truncated after *any* lattice site; the cluster does not even have to be rectangular [44].

The in-phase clusters stem from the Γ point Bloch waves, whereas the out-of-phase clusters have the same phase profile as the M point Bloch waves. This holds for *both* kinds of nonlinearities – focusing and defocusing ones. Hence the defocusing in-phase and the focusing out-of-phase clusters exemplify that in general there is no simple connection between the curvature of the *linear* dispersion relation [cf. Figure 2.3 (b)] and the existence of gap solitons.

An easy way to confirm these statements is given by looking at the Fourier transforms of the complex amplitude profiles: Since the Bloch functions can be written as a product of a lattice-periodic function and a plane wave function containing the quasi-momentum [cf. section 2.3.1], a significant contribution of a particular Bloch mode with the quasi-momentum (k_x, k_y) also causes a peak in the Fourier spectrum *at the same spatial frequencies*. The Bloch modes from the higher-order bands are mapped onto spatial frequencies outside of the first Brillouin zone (i.e., the Bloch spectrum becomes unfolded). In this spirit the Fourier transform can be used as an easily computable replacement for the Bloch transform, whereas one has to ignore "artificial" peaks arising from the lattice-periodic parts of the Bloch functions. However, their amplitudes are usually not dominating.

From the bottom row of Figure 3.9 one can see that the Fourier spectra of the in-phase profiles indeed have their maxima at the Γ point ($k_x = k_y = 0$), while those of the out-of-phase clusters have theirs at the M points ($\pm k_x = \pm k_y = \pi/d$ due to the sign symmetry in quasi-momentum space). Minor peaks occur also at the X points; they are caused by the finite sizes of the clusters. The corresponding Bloch waves alter their sign only in *one* transverse direction. Especially for small clusters their contribution is needed to obtain approximately equal intensities at

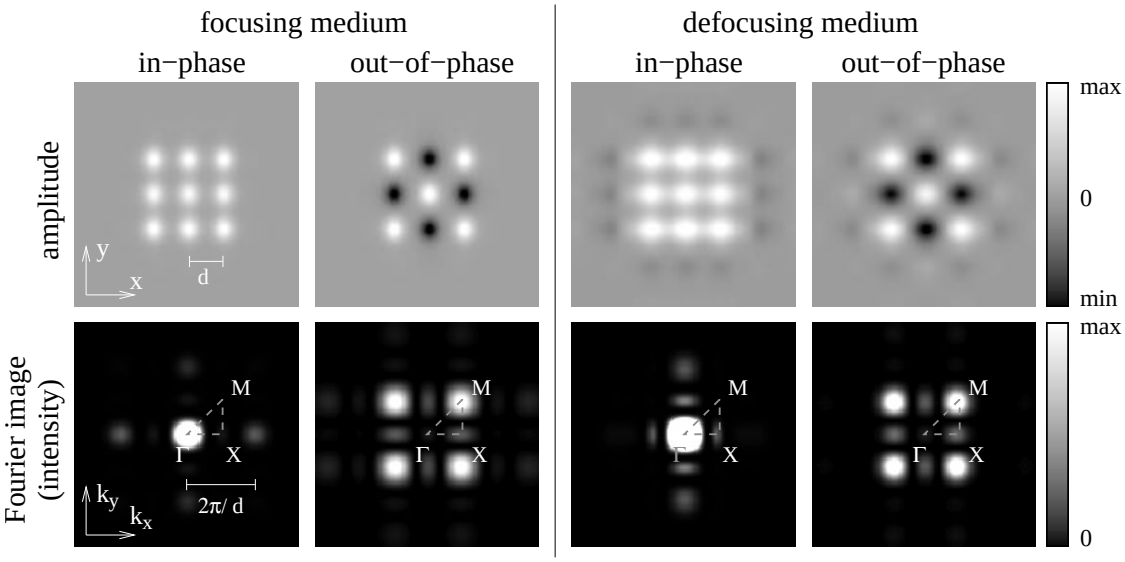

Figure 3.9: Amplitude profiles (top row) and Fourier images (bottom row) of soliton clusters with 9 lobes (anisotropic model, $V_{eff} = 0.0018$). The in-phase profiles arise from Bloch modes near the Γ point, whereas the out-of-phase profiles stem from Bloch modes near the M point.

all lobes.

For the in-phase clusters the spatial frequency of the lattice is directly visible (peaks being $2\pi/d$ apart from the Γ point); for the out-of-phase clusters the corresponding peaks occur at the same distance from the M points (sum frequency), though being less accentuated.

The effects of the anisotropy are subtle: In a *focusing* medium, the anisotropy gives rise to two *minima* of the refractive index in the vicinity of each intensity maximum, which are aligned in x direction [Figure 2.2 (b)]. Therefore the lattice depth is locally *enhanced* in this direction. In a *defocusing* medium the nonlinear effects are reversed, hence the refractive index is *raised* next the intensity maxima, while it is lowered at the centers of the lattice sites. Thus the lattice is partially washed out in x direction.

Since the amplitude profiles must reflect the shape of the refractive index in order to form solitons, these effects also become indirectly visible in their Fourier images. For the in-phase lattices, the peaks corresponding to the x component of the lattice frequency are indeed slightly pronounced in the focusing case, whereas they are diminished in the defocusing case. By contrast, the Fourier spectra of the out-of-phase clusters look almost isotropic. That is because the intensity reaches zero between adjacent lobes, which leads to a suppression of anisotropic and nonlocal effects in the soliton profiles to a certain degree. If the phase profile is distorted however (e.g., due to instabilities), the anisotropy becomes visible again. This is

shown in the next section [cf. Figure 3.11 (a)].

The amplitude profiles of the defocusing clusters show another interesting detail: The amplitude does not decay monotonically beside the outer lobes, but rather features a sign change followed by a smaller peak on the adjacent lattice site. These "side lobes" are characteristic for finite-gap solitons; they also occur for single fundamental solitons in defocusig media [even in 1D, cf. Figure 2.4 (d)].

3.2.2 Stability

The lobes of the above soliton clusters are coupled weakly in the sense that the intensity contribution of a single lobe to the neighboring lattice sites is small. Since instabilities are related to a transfer of intensity between the lobes, it is useful to consider the transverse *intensity current density* $\mathbf{J}$ of the complex optical amplitude $A(x, y)$. This quantity can be introduced in complete analogy with the probability current density of the ordinary Schrödinger equation:

$$\mathbf{J}(x, y) = 2\,\mathrm{Im}\left[A^*(x, y)\boldsymbol{\nabla}_\perp A(x, y)\right]. \tag{3.5}$$

From this equation it immediately follows that $\mathbf{J}$ vanishes for any real amplitude profile. At the outset of the propagation this is also the case for the soliton clusters discussed in the previoud section, since their phases can only take the values 0 or π. In order to decide whether this may change during the propagation, we have to consider small perturbations of them.

Let us consider the focusing in-phase cluster and assume that the middle lobe has a slightly higher intensity than its neighbors. This situation is depicted in Figure 3.10 (a). Since this leads to a small increase of the refractive index, the phase of the middle lobe changes more rapidly. Thus it will be in *advance* after some propagation distance, causing a certain phase gradient: If the amplitudes of the outer lobes are considered to be real (i.e, their phases are 0), the middle lobe receives a complex amplitude with a *positive* imaginary part. Now the vector field $\mathbf{J}$ points, according to Eqn. (3.5), from the outer lobes towards the middle one [Figure 3.10 (a), $z = 9.5z_0$]. Therefore the intensity of the middle lobe further increases, i.e., the initial in-phase cluster is unstable. This argumentation works in a similar way if a *decreased* intensity of the middle (or any other) lobe is assumed initially.

The vertical coupling strength is slightly higher than the horizontal one, because the horizontal lattice depth is increased by the anisotropy (cf. the previous section). Hence the absolute values of $\mathbf{J}$ in Figure 3.10 (a) ($z = 9.5z_0$) are larger in the vertical direction.

The sign of $\mathbf{J}$ changes when the phase difference between the middle lobe and the outer ones exceeds π [Figure 3.10) (a), $z = 12.6z_0$], and some intensity is transferred back towards to outer lobes. However, the symmetry of $\mathbf{J}$ is usually lost after a certain propagation distance due to further instabilities, so there is no recurrence of

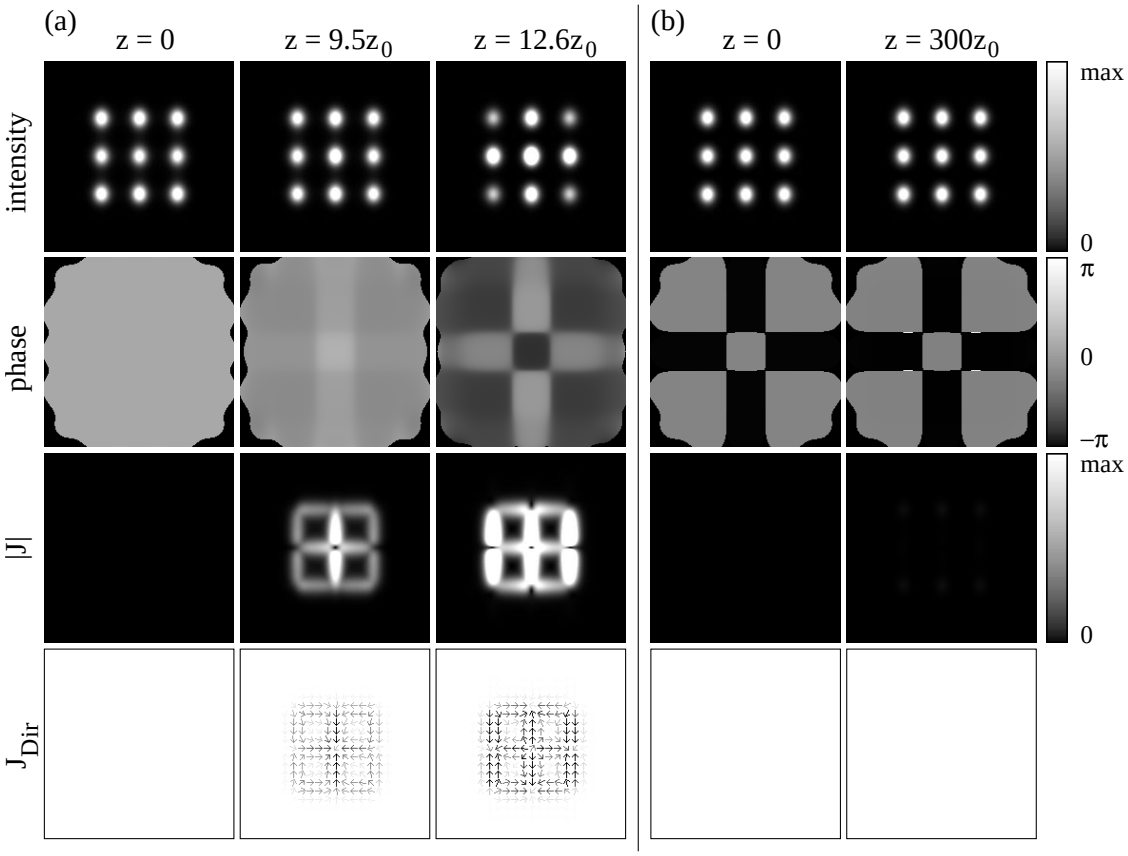

Figure 3.10: Propagation of a focusing 9-lobe soliton cluster ($V_{eff} = 0.0018$, $\beta = 10$, anisotropic model; cf. Figure 3.9) with a phase difference of 0 (left) or π (right) between the lobes. The direction field of $\mathbf{J}$ is denoted by J_{Dir} (dark arrows denote high values of $|\mathbf{J}|$).

the original (i.e., $z = 0$) beam profile in general. Instead, the intensity flux between the lobes becomes irregular, although the profile with nine lobes is maintained if the coupling between them is not too strong.

In order to create a stable cluster, it is necessary to change the direction of $\mathbf{J}$ such that it always counteracts intensity differences between the lobes (then the above discussion on small perturbations just reverses). This is achieved if the phase differences between all lobes are exactly equal to π. By this means, instabilities of the above kind are suppressed for focusing out-of-phase clusters, and the propagation may be stable even over large distances [Figure 3.10 (b)].

A stabilizing effect of alternating $0, \pi$ phase distributions has also been reported for soliton clusters in bulk media [35]. However, in this case the positions of the constituting solitons are not fixed within the cluster, since there is no underlying, static lattice. Hence the above treatment cannot simply be transferred, but the stabilization effect is rather based on the way how the refractive index changes

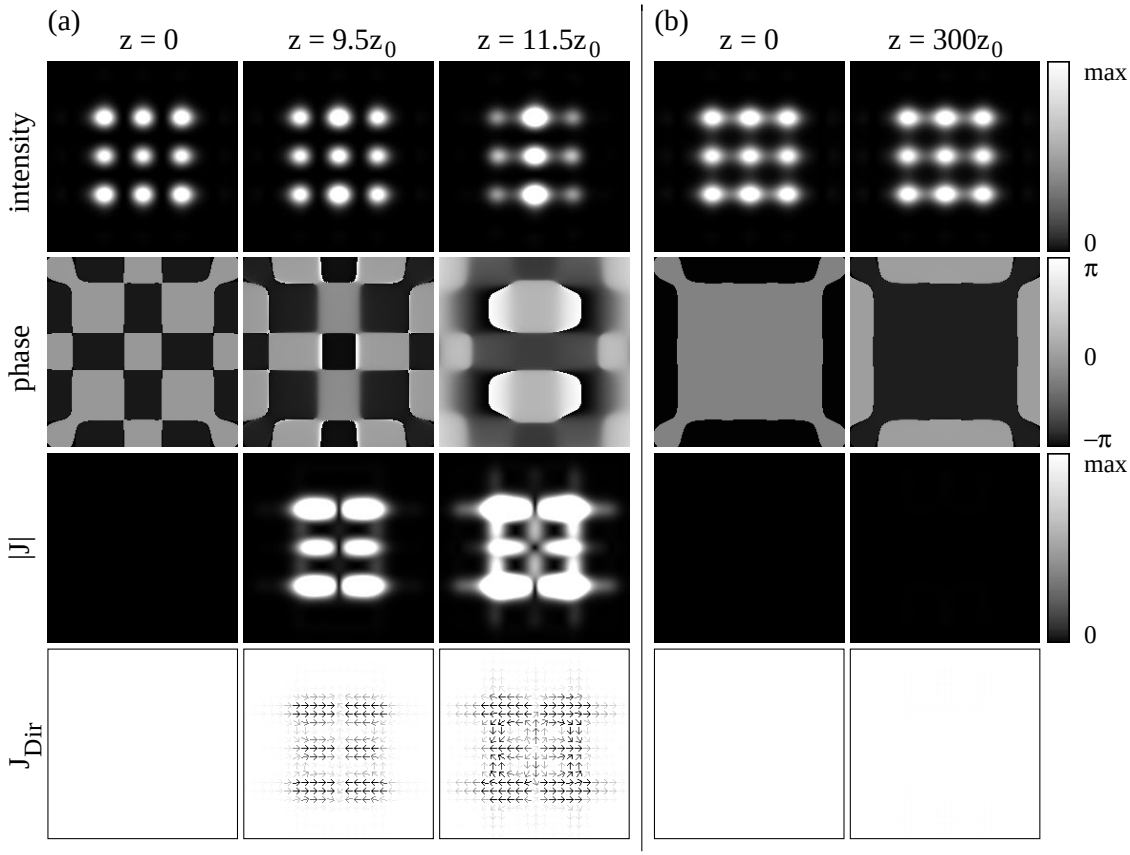

Figure 3.11: Propagation of a defocusing 9-lobe soliton cluster ($V_{eff} = 0.0018$, $\beta = 6$, anisotropic model; cf. Figure 3.9) with a phase difference of π (left) or 0 (right) between the lobes. The direction field of $\mathbf{J}$ is denoted by J_{Dir} (dark arrows denote high values of $|\mathbf{J}|$).

induced by interacting solitons overlap.

If the *sign* of the nonlinearity is changed, a higher intensity of a particular lobe leads to a phase *delay*. Thus the stability arguments are reversed again, stating that defocusing out-of-phase clusters are unstable, whereas defocusing in-phase clusters are stable. As Figure 3.11 shows, these considerations may again be confirmed by numerical simulations. According to the previous section, the lattice depth is decreased in the x direction. Hence the *horizontal* coupling constants between adjacent lattice are larger now [Figure 3.11 (a)], leading again to increased values of $|\mathbf{J}|$ in that direction. In total, the coupling is much stronger than in the focusing case, as one can see by comparing the Figures 3.10 (a) and 3.11 (a). The intensity of the lobes changes considerably ($z = 11.5z_0$). The nine-lobe profile is *not* conserved in the further course of the propagation, i.e., some lobes temporarily or even finally vanish.

4 Gap solitons in optically induced photonic lattices

4.1 Lattice types

As already mentioned in section 2.3.2, the optical induction of *homogeneous* lattices requires a spatially periodic amplitude profile (*lattice wave* A_{latt}), which does not show any diffraction effects while propagating in the linear regime. A survey of suitable profiles is presented in [54], although in a configuration allowing nonlinear self-interaction (i.e., the polarization was taken to be extraordinary). These profiles are briefly recapitulated in Table 4.1, together with the effectively induced changes of the refractive index [cf. Eqns. (2.18) and (2.28)]. The mathematical expressions for A_{latt} are normalized to the amplitude 1. The spatial frequencies of the lattices are denoted by k'_x and k'_y; the respective lattice constants[1] are given by $d_{x,y} = 2\pi/k'_{x,y}$.

It can be seen that in general the profiles of $|A_{latt}|^2$ and δn^2 may differ strongly due to the anisotropic and nonlocal properties of the nonlinearity. In the case of a focusing medium ($E_{ext} > 0$), the refractive index is raised (white areas) in regions where $|A_{latt}|^2$ is large. In regions where $|A_{latt}|^2$ is minimal however, the refractive index may become even lower than in an unilluminated crystal. Thus *defocusing* (black) areas occur as well. For defocusing media things are vice versa, and thus the induced refractive index patterns are inverted.

Since the *isotropic* model states a strictly monotonic relation between $|A_{latt}|^2$ and E_{scr}, the intensity plots of A_{latt} may serve as an (approximate) visualization of the refractive index pattern one would expect in this model.

In the following we discuss the specific properties of the particular lattice types. In doing so, we use a naming scheme which represents a compromise between the underlying symmetry of the lattices and the names used most commonly in the literature. In this context, it is important to note that due to the anisotropy, the refractive index lattices have no further symmetries apart from being invariant under reflections along the coordinate axes. We therefore always refer to the intensity profile of the lattice wave when we speak of lattice symmetries in the following.

4.1.1 Square and rectangular symmetry

We start our discussion with the *square lattice* depicted in the first row of Table 4.1. The intensity profile of the lattice wave consists of a rectangular grid of bright

[1] Throughout this work we always measure both the spatial frequencies of the lattices and their period lengths along the coordinate axes, since the x axis is singled out by the nonlinearity. Hence we also consider only dilations of the lattices along these directions.

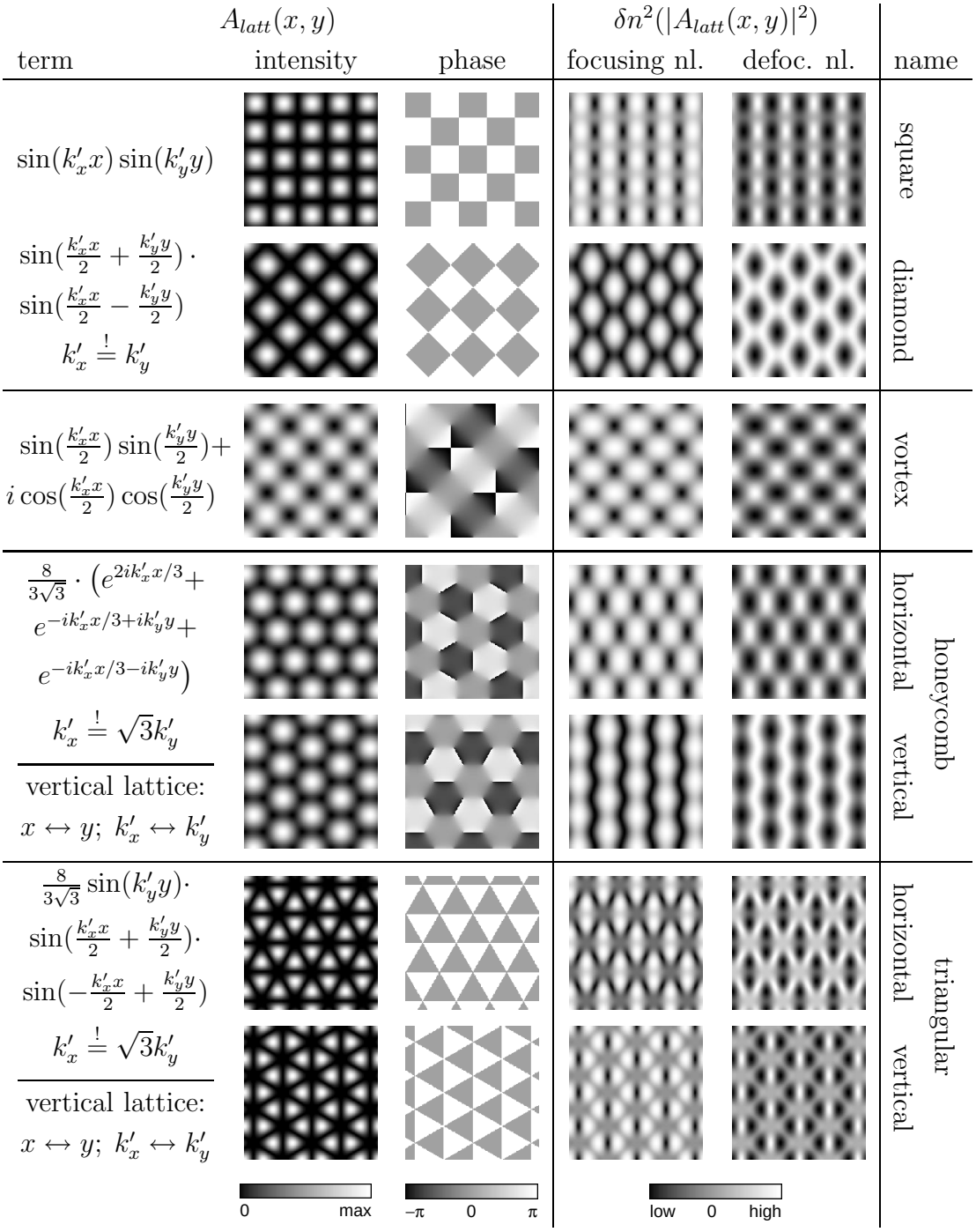

Table 4.1: Survey of some lattice waves propagating without linear diffraction (left) and of the corresponding refractive index patterns (right). For the triangular and honeycomb lattices, only the terms for the horizontal orientations are given in the leftmost column. The corresponding ones for the vertical orientations are obtained by simply exchanging x and y as well as k'_x and k'_y.

spots, where k'_x and k'_y do not need to be equal. The lattice is aligned parallel to the coordinate axes, and the spots are well separated by phase jumps of π. By contrast, the induced refractive index patterns show accentuated vertical stripes which reflect the photorefractive anisotropy. Basically, these patterns can be seen as periodic arrangements of the refractive index change induced by a single Gaussian beam [Figure 2.2 (b)]. Thus the gradient of E_{scr} is large along each row of bright spots, whereas it is much smaller between the rows and in the y direction.

As it has been demonstrated in [37, 41], this can result in effectively one-dimensional lattices even in the experiment. Therefore this lattice type is less suitable for the investigation of more complex solitary structures.

The influence of the anisotropy can be minimized if the square lattice is rotated about 45°. This configuration is also known as *diamond lattice* in the literature. The sites of the corresponding refractive index lattice are still elliptically shaped, but now the depth of the defocusing areas between them is equal along *both* coordinate axes. However, k'_x and k'_y must be equal in this case, since the lattice wave shows diffraction otherwise.

An interesting possibility to combine the advantages of both the square and the diamond lattice is given by the *vortex lattice* shown in the third row of Table 4.1. The lattice wave has a tessellated intensity distribution, while the phase does not simply jump between 0 and π but rather exhibits a singularity at each intensity minimum (hence the name "vortex lattice" [54]). However, this nontrivial phase structure has no counterpart in the refractive index pattern since the latter depends only on the intensity. From a practical point of view, the most striking feature of this lattice is that the refractive index inherits the tessellated structure without major deviations. This offers the possibility to induce a similar lattice for *both* kinds of nonlinearities by simply switching the sign of E_{ext}.

Although a square symmetric vortex lattice is shown in Table 4.1, no restrictions apply to k'_x and k'_y. This is because the corresponding lattice wave is derived from those of the simple square lattice. Changing the spatial frequencies modifies the angles of the elementary cell, so it can be continuously transformed into a lattice with a hexagonal symmetry. Indeed, the shape of the first Brillouin zone is always a hexagon if $k'_x \neq k'_y$.

4.1.2 Hexagonal symmetry

Table 4.1 shows two different lattice types with a hexagonal symmetry: One has a honeycomb structure (rows four and five), while the other is made up of little triangles being arranged to hexagons (these triangles are also found in the phase structure). Unfortunately, *both* have already been called 'triangular lattices' in the literature. In order to guard against misunderstandings, we will use this term *solely* for the latter, as it has been introduced in [54]. In contrast, we will refer to the former as 'honeycomb lattice'.

Since hexagonal patterns are not invariant under rotations about 90°, we have to

distinguish two orientations with respect to the c axis (x direction): A *horizontal* one, where the centers of the underlying hexagons are aligned in *rows*, and a *vertical* one, where they are aligned in *columns*.

The *honeycomb lattices* have already been the subject of several publications [55–57], however solely in connection with the isotropic model. This lattice type is preferred in several experiments, since it can be generated easily by superimposing three plane waves. Similar to the vortex lattice, the phase structure of the lattice wave features singularities. Their centers coincide with the corners of the hexagons, hence these are visible as dark spots in the intensity profile.

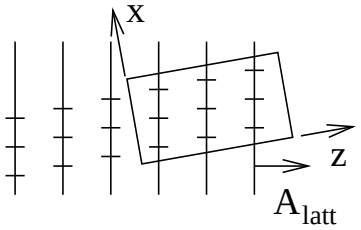

Figure 4.1: Stretched (horizontal) honeycomb lattice: Tilting the crystal in order to compensate for the transversal shift of the lattice structure

In order to completely suppress diffraction effects, the spatial frequencies of the horizontal honeycomb lattice must be at a ratio of $k'_x : k'_y = \sqrt{3} : 1$ (the inverse ratio holds for the vertical orientation). However, it can be easily shown that for all other ratios the diffraction only causes a translation of the otherwise unchanged lattice profile. This translation always takes place along that axis which determines the orientation of the lattice (i.e., the x axis for the horizontal lattice and the y axis for the vertical one). Though it could be compensated for by slightly tilting the crystal (Figure 4.1), it turns out to be practically irrelevant in the majority of cases (the required tilting angle is less than 0.1°, if the lattice period in the direction of translation is larger than 10μm). This is always assumed within this thesis. Tilting the crystal by larger angles ($> 1°$) requires a correction of the ratio $k'_x : k'_y$, since in this case the phase fronts of the propagating lattice wave are no longer parallel to the front and rear facets of the crystal.

With this (rather theoretical) restriction, the honeycomb lattices can be scaled as flexibly as the vortex lattice. For the horizontal orientation, also the refractive index patterns have much in common. By contrast, the vertical orientation leads to vertical stripes in the refractive index, being more similar to the square lattice.

Unlike the honeycomb lattices, the *triangular lattices* have a *real* amplitude distribution, hence their phase profile can only take the values 0 and π. This yields a triangular phase pattern, since the phase alters between adjacent intensity maxima. For the triangular lattices, the differences between $|A_{latt}|^2$ and the refractive index patterns are most distinctive. This results from the fact that each *vertically* aligned "dipole-pair" of the *horizontal* lattice is melted to a single focusing (or defocusing) region with a pronounced elliptical shape. On the contrary, the *horizontal* dipole-pairs of the *vertical* lattice are separated by strongly defocusing (or focusing) regions, so the maxima (or minima) of the refractive index remain

triangular.

The *defocusing, horizontal* triangular lattice does not feature pronounced lattice sites. Consequently, higher order band gaps almost do not occur, even for very high modulation depths. Therefore this lattice type is not well-suited for the investigation of (defocusing) gap solitons.

4.2 Band structure and basic solitons

We now investigate how far the results obtained in chapter 3 can also be transferred to optically induced lattices. In doing so, we focus on the diamond and the vortex lattices (exemplifying square symmetric systems) as well as on the triangular lattices (exemplifying hexagonally symmetric systems). We consider only focusing nonlinearities in this section.

4.2.1 Diamond and vortex lattices

Figure 4.2 compares the band structure of the diamond lattice with that of the square (i.e., $k'_x = k'_y$) vortex lattice. In both cases, $d_x = d_y = 25\mu$m has been assumed.

Since optically induced lattices are controlled via the nonlinearity, they are subject to the photorefractive saturation effect. Hence their depth is limited even for arbitrarily high intensities of A_{latt}, and the same holds also for the number of finite band gaps [Figure 4.2 (a) and (c)]. The only way to obtain deeper lattices consists in raising the external electrical field E_{ext}.

In the following we nevertheless use the quantity $I_{latt} \equiv \max(|A_{latt}|^2)$ as a measure for the lattice strength, because the intensity of A_{latt} is easier accessible in the experiment than the lattice depth V_{eff} [cf. Eqn. (2.29)].

For the diamond lattice, it is possible to obtain more than one finite gap even for $E_{ext} = 2.5$kV/cm, whereas this is not the case for the square vortex lattice. Further details can be gathered from the dispersion relations [Figures 4.2 (b) and (d)], which are shown here for $I_{latt} = 5$. Due to the anisotropy, the first Brillouin zone cannot be reduced further than the shaded triangle outlined in Figure 4.2 (e). However, the M points are still equivalent – they may be mirrored at the Γ point and shifted by $(\pm k'_x, \pm k'_y)$. Although the anisotropic effects seem to be weak for these lattice types (cf. Table 4.1), it can be seen that the dispersion curves along the paths $\Gamma - M_1$ and $M_2 - \Gamma$ are not identical (this is more pronounced for the vortex lattice).

A more distinctive feature of the anisotropy consists in the clear separation of the second and the third dispersion curves (counted from the top) at the $M_{1,2}$ points. The corresponding Bloch modes have a phase profile which is unstaggered in one direction, but staggered in the other one. These Bloch modes form the horizontally or vertically antisymmetric $B_1^{(foc)}$ solitons, which are akin to those

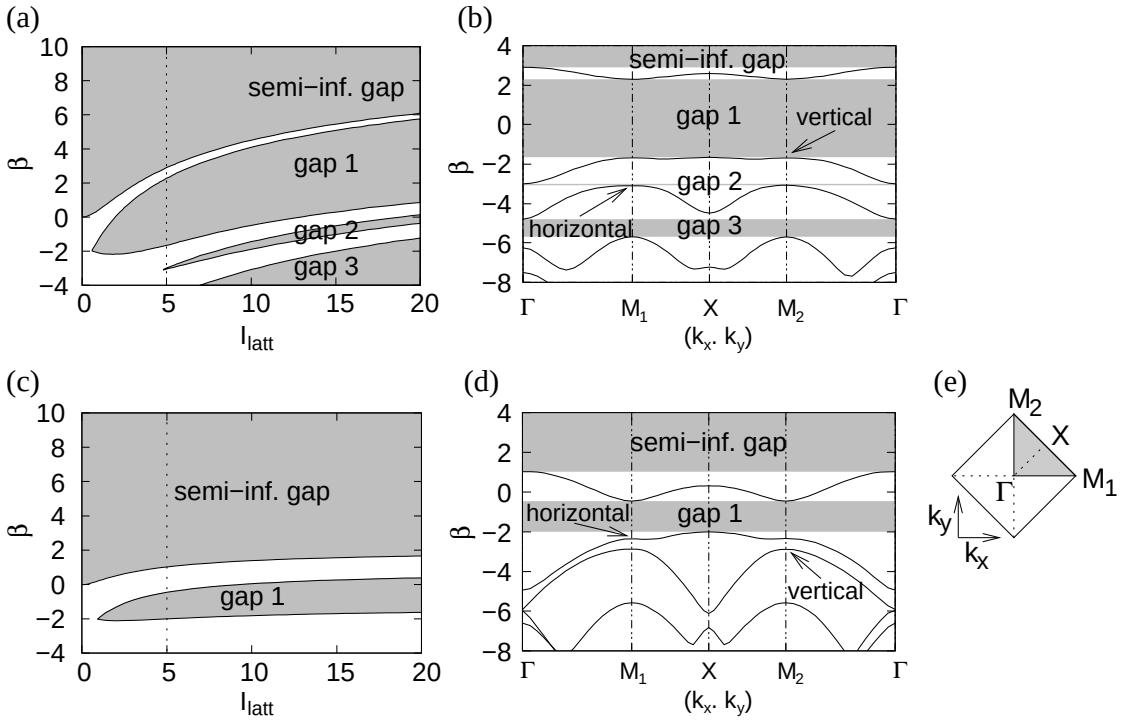

Figure 4.2: Comparison between the diamond lattice (top row) and the square vortex lattice ($k'_x = k'_y$, bottom row) for a focusing nonlinearity ($E_{ext} = 2.5\,\mathrm{kV/cm}$): (a), (c) dependency of the band structure on the lattice strength; (b), (d) band structure [$I_{latt} = 5$, dotted lines in (a) and (c)]; (e) first Brillouin zone. The order of the Bloch bands connected to the horizontal and vertical $B_1^{(foc)}$ solitons is different in both cases.

obtained in section 3.1.3. They occur in different order in the diamond and in the vortex lattice. If the system were isotropic, their propagation constants at the $M_{1,2}$ points would be identical.

In the diamond lattice, the separation of the horizontal and vertical Bloch modes is more pronounced. Here even an additional band gap (gap 2) arises between them for $I_{latt} \gtrsim 5$. The propagation constants of the vertically alternating Bloch modes are higher. Consequently, the vertical $B_1^{(foc)}$ solitons have lower total intensities. This differs from the square vortex lattice, where the basic solitons in the first gap are given by the horizontal $B_1^{(foc)}$ solitons. Also the additional band gap does not occur for $I_{latt} < 20$, if $E_{ext} \lesssim 4.5\mathrm{kV/cm}$.

Intuitively, these facts can be understood to a certain extent by having a closer look at the shape of the lattice sites (cf. Table 4.1). For the diamond lattice, these are clearly stretched in the y direction, whereas the opposite is true for the vortex lattice. In the latter case, the elliptic shape is less pronounced however.

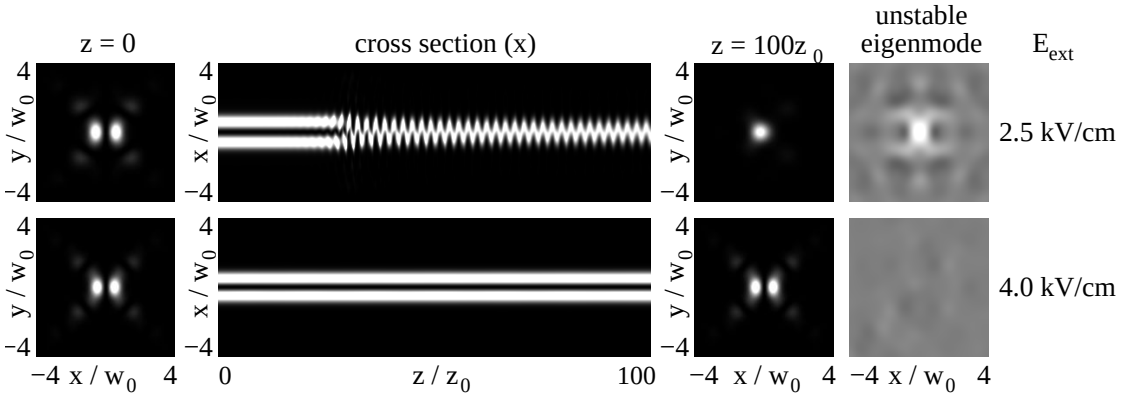

Figure 4.3: Horizontal $B_1^{(foc)}$ solitons in the square vortex lattice ($I_{latt} = 5$, $\beta = -1.2$). Top row: Unstable propagation and decay into stable $B_0^{(foc)}$ soliton for $E_{ext} = 2.5\,\mathrm{kV/cm}$. Bottom row: Stable propagation for $E_{ext} = 4.0\,\mathrm{kV/cm}$. The plots of the unstable eigenmodes show only the (dominating) real part; a 50% gray level denotes a zero amplitude. In all other cases light gray tones denote high intensities.

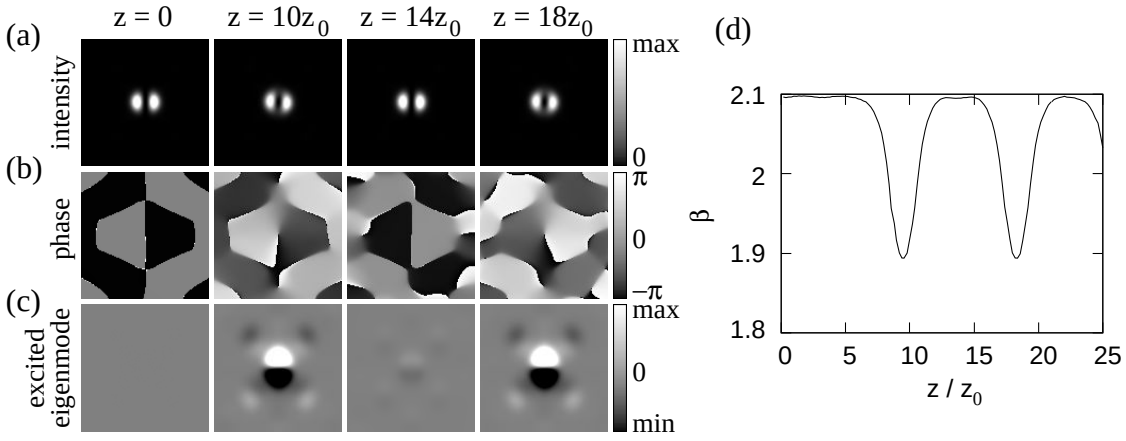

Figure 4.4: Horizontal $B_1^{(foc)}$ solitons in the diamond lattice [$E_{ext} = 4.0\,\mathrm{kV/cm}$, $I_{latt} = 5$, $\beta = 2.1$]: The excitation of a vertical antisymmetric eigenmode leads to a stationary, periodic occurence of a phase singularity. (a) intensity profile; (b) phase structure; (c) real part of the excited eigenmode; (d) propagation constant over propagation distance.

Hence it might be suspected that the instabilities of the vertical $B_1^{(foc)}$ solitons are weaker in the diamond lattice and stronger in the vortex lattice, whereas the situation should be the other way round for the horizontal $B_1^{(foc)}$ solitons.

But investigating this question in more detail, one finds that the horizontal $B_1^{(foc)}$ solitons are always unstable even in the vortex lattice if $E_{ext} = 2.5\text{kV/cm}$. Their decay is very similar to the ones discussed in chapter 3; it is triggered by the bell-shaped, fundamental eigenmode and leads to a stable $B_0^{(foc)}$ soliton. An example for $I_{latt} = 5$ and $\beta = -1.2$ is shown in the top row of Figure 4.3. If E_{ext} is raised to 4kV/cm however, the horizontal $B_1^{(foc)}$ solitons may become stable within a certain interval near the lower edge of the first gap (bottom row of Figure 4.3).

In the diamond lattice, the horizontal $B_1^{(foc)}$ solitons are indeed highly unstable for $E_{ext} = 2.5\text{kV/cm}$. The beam is horizontally displaced after a relatively short propagation distance ($z \lesssim 5z_0$), and the major part of the intensity is diffracted subsequently.

For $E_{ext} = 4\text{kV/cm}$ the nonlinear effects become strong enough to hold the beam on the initial lattice site. In this case, the *second* gap is large enough to support stable, horizontal $B_2^{(foc)}$ solitons[2] near the lower edge. For higher intensities, the fundamental eigenmode becomes unstable again, and the already well-known decay into a $B_0^{(foc)}$ soliton follows.

This is also the predominant decay scheme of the horizontal $B_1^{(foc)}$ solitons. However, for certain values of β the growth rate of a *vertically antisymmetric* eigenmode may become larger than those of the fundamental one. This eigenmode corresponds to a *vertical* $B_1^{(foc)}$ soliton. As shown in Figure 4.4, it does *not* necessarily lead to an immediate transformation into a $B_0^{(foc)}$ soliton. Instead, the excited eigenmode periodically dies out after a certain propagation distance ($z = 14z_0$) and becomes excited again ($z = 18z_0$). This behavior is also reflected in the propagation constant [Figure 4.4 (d)]. Usually it is only transient and passes into the decay scheme described previously, since the excitation of the *fundamental* eigenmode is only delayed. However, there are cases in which these transients last very long ($> 500z_0$); this holds particularly for the one depicted in Figure 4.4.

The excitation of the vertically antisymmetric eigenmode also leads to a qualitative change in the phase profile [Figure 4.4 (b), $z = 10z_0$ and $z = 18z_0$]: Since its propagation constant differs from that of the soliton itself, a certain phase delay arises between both profiles after a certain propagation distance. This involves a screw-like phase profile with a branch cut and a *singularity* in its center. Hence the integral over the phase along a closed path containing the center does not yield zero anymore, but rather $2\pi \cdot m$ ($m \in \mathbb{Z}$). Such a structure is called a *vortex* with the topological charge m (here we have $|m| = 1$). The vortex periodically appears and disappears together with the vertically antisymmetric eigenmode, each time

[2] For this lattice type, the horizontal $B_1^{(foc)}$ solitons can be seen as a continuation of the horizontal $B_2^{(foc)}$ ones into the first gap.

changing the sign of its charge. The properties of vortices on single lattice sites are discussed in more detail in chapter 6.1.2, including the example presented here.

Interestingly, the vertical $B_1^{(foc)}$ solitons *alone* are unstable as well. This does not only hold for the parameters used in Figure 4.4, but in fact no stable regime has been found for $I_{latt} \leq 5$ and $E_{ext} \leq 4$kV/cm. A stabilization could only be achieved by increasing I_{latt} to 10 ($E_{ext} = 2.5$kV/cm). The decay of the unstable vertical $B_1^{(foc)}$ solitons is generally triggered by the fundamental eigenmode again, thus yielding a stable $B_0^{(foc)}$ soliton at the end.

Being in line with the above supposition, vertical $B_1^{(foc)}$ solitons are even worse supported by the square vortex lattice. They feature strong instabilities up to $E_{ext} = 4$kV/cm, often the beam is pushed away from the initial lattice site followed by a complete decay due to diffraction. This is the usual scenario for low and medium beam intensities, i.e., away from the upper edge of the gap. For high intensites, the leading unstable eigenmode may correspond to a horizontal $B_1^{(foc)}$ soliton in its phase and shape. This again leads to the transient appearance of a vortex, though this state is less robust here than in the diamond lattices discussed above (Figure 4.4). Nevertheless, the transient vortex may transform via an unstable horizontal $B_1^{(foc)}$ soliton into a stable $B_0^{(foc)}$ one.

4.2.2 Horizontal triangular lattice

The band structure of the horizontal triangular lattice ($d_x = 30\mu$m, $E_{ext} = 2.5$kV/cm) is shown in Figure 4.5. The first Brillouin zone is a regular hexagon, which can be reduced to a trapezoid by exploiting the mirror symmetries in the Bloch space [Figure 4.5 (c)]. Again, the $M_{1,2}$ points are equivalent.

A detailed view of the dispersion relation is depicted in Figure 4.5 (b) for $I_{latt} = 1.67$. The Bloch modes from the first four bands represent *localized states*, i.e., their intensity profiles do not have any maxima in the areas between the lattice sites[3]. They may be compared with the lowest-order modes of a linear waveguide – TEM_{00}, TEM_{01}, TEM_{02}, and TEM_{10} in order of descending β. This also holds for the phase profiles at the Γ and $X_{1,2}$ points, which only take the values 0 or π. The phase profiles at the $M_{1,2}$ points contain singularities however, thus being more complicated.

The pronounced anisotropy favors those higher-order Bloch modes, which represent *vertically* excited states (i.e., which are associated with TEM_{0i} modes at the lattice sites). These have significantly higher propagation constants than the Bloch modes representing *horizontally* excited states (TEM_{i0} modes). Therefore the individual dispersion curves become separated by band gaps at relatively low lattice strengths already, so the total number of band gaps is rather high [Figure 4.5 (a), not all of them shown for $I_{latt} > 3.5$]. This is a specific feature of the horizontal

[3] such states correspond to *bound lattice states* in the quantum mechanical picture

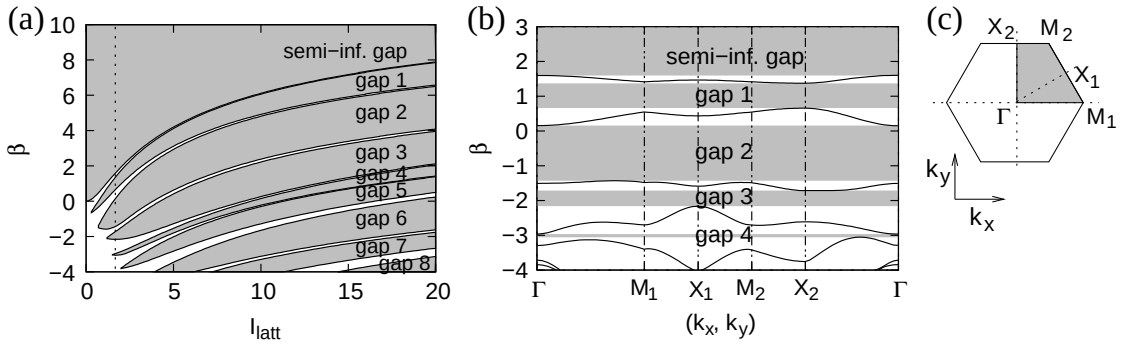

Figure 4.5: Horizontal triangular lattice (focusing nonlinearity, $E_{ext} = 2.5\,\mathrm{kV/cm}$): (a) dependency of the band structure on the lattice strength; (b) band structure [$I_{latt} = 1.67$, dotted line in (a)]; (c) first Brillouin zone.

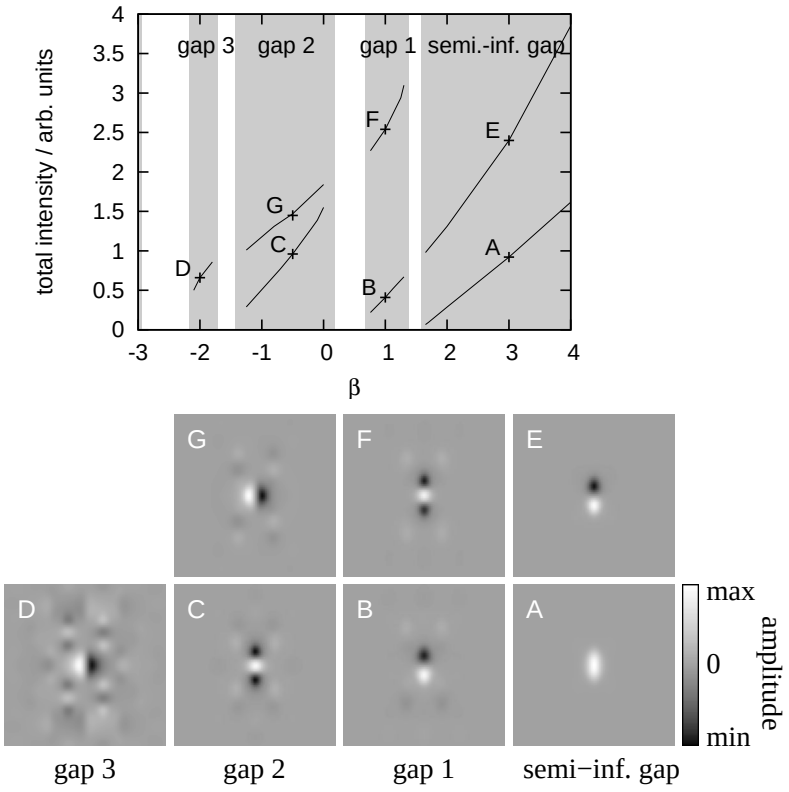

Figure 4.6: Total intensities (black lines) and amplitude profiles of the focusing basic solitons (A-D) and their "continuations" (E-G) across Bloch bands (horizontal triangular lattice, $E_{ext} = 2.5\,\mathrm{kV/cm}$, $I_{latt} = 1.67$). The profiles A and B are dynamically stable.

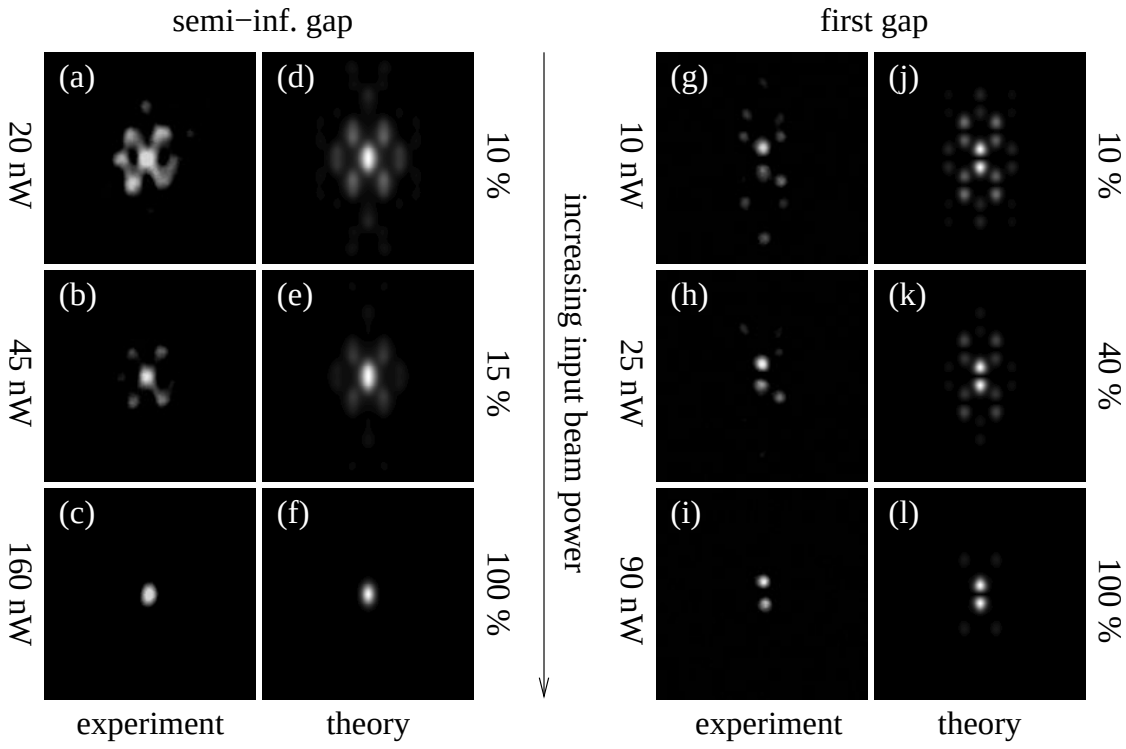

Figure 4.7: Formation of basic solitons [$B_0^{(foc)}$, (a)-(f) and $B_1^{(foc)}$, (g)-(l)] in the horizontal triangular lattice ($z_{max} = 20\,\mathrm{mm}$): Comparison between theory and experiment for different beam powers. The percentages beside the theoretical pictures refer to the relative intensities with respect to the solitary beams shown in (f) and (l). Light gray tones denote high intensities. Experimental pictures by courtesy of Patrick Rose [42].

triangular lattice in combination with a focusing nonlinearity[4]. Therefore this lattice type is well-suited for studying solitons in higher-order gaps.

The basic solitons associated with the first four bands are shown in Figure 4.6 (profiles A-D). The fundamental ones (A) arise from the Γ point, whereas the $B_1^{(foc)}$ solitons (B) originate from the X_2 point. Despite the relatively weak lattice, also the latter are dynamically stable for $0.9 \lesssim \beta \lesssim 1.2$ (this interval covers nearly 50% of the first gap). This remarkable property may be ascribed basically to the pronounced elliptic shape of the lattice sites.

The $B_2^{(foc)}$ solitons (C) possess *three* vertically aligned intensity maxima at the center lattice site. They oriniginate from the vicinity of the Γ point, hence they are

[4]The corresponding *defocusing* lattice exhibits only a small number of band gaps, even at very high lattice strengths. This is due to the relatively small areas of a high refractive index, see Table 4.1.

symmetric along *both* coordinate axes, just like the fundamental solitons. Though being unstable for $I_{latt} = 1.67$, they become stable as well at higher lattice strengths ($I_{latt} = 5$ is sufficient).

The enhanced stability of the $B_1^{(foc)}$ and $B_2^{(foc)}$ solitons at moderate values of I_{latt} and E_{ext} is another distinctive feature of the horizontal triangular lattice. It does not occur in a horizontal honeycomb lattice of the same geometry. However, in this lattice type $B_1^{(foc)}$ solitons may nevertheless turn out to be *practically* stable over short propagation distances. This has been demonstrated experimentally in [55].

Basic solitons with a *horizontally* antisymmetric amplitude profile occur in the third band gap for the first time. They are shown in Figure 4.5 (D). Though being unstable for $I_{latt} = 1.67$, even these can be stabilized by raising the lattice strength to $I_{latt} = 5$. This fact is remarkable with regard to the *vertical* elliptic shape of the lattice sites. It is a consequence of the rather narrow Bloch bands, leading to a quite efficient suppression of resonances with unstable eigenmodes.

All of the basic solitons in the first three finite gaps have (non-basic) continuations in the adjacent gaps (profiles E-G in Figure 4.6). The continued $B_2(foc)$ solitons (F) appear to be unstable up to very high values of I_{latt} and E_{ext}. By contrast, the continued $B_1^{(foc)}$ solitons (E) and can be stabilized in the semi-infinite gap for $I_{latt} = 5$, if E_{ext} is increased to $E_{ext} = 4\mathrm{kV/cm}$ and β is not too high. The same holds for the continued $B_3^{(foc)}$ solitons (G) in the second gap.

The $B_0^{(foc)}$ and $B_1^{(foc)}$ solitons of the horizontal triangular lattice have also been realized in the experiment [42]. Figure 4.7 shows their gradual formation in comparison with the theory as the input beam power is being increased. The total propagation distance (crystal length) was 20 mm in both cases.

The experimental $B_0^{(foc)}$ soliton has been excited by a Gaussian input beam, whereas a dipole input beam created with the aid of a vortex mask was used to realize the $B_1^{(foc)}$ soliton. The theoretical pictures were obtained by using true soliton profiles, which were scaled according to the specified percentages. In doing so the values have not been chosen to exactly resemble the experimental power ratios, but they rather have been adjusted with a view to maximize the visual agreement with the experimental pictures. Also the other parameters have been optimized to that effect ($E_{ext} = 1.5\,\mathrm{kV/cm}$ and $I_{latt} = 1$ for the $B_0^{(foc)}$ soliton; $E_{ext} = 2.5\,\mathrm{kV/cm}$ and $I_{latt} = 1.67$ for the $B_1^{(foc)}$ soliton); they were altered between the experiments as well. However, one has to bear in mind that a *quantitative* agreement between theory and experiment cannot be expected in general due to the arguments given at the end of section 2.2.

The *qualitative* agreement is very good in both cases. Minor deviations occur especially in the low-intensity regime. The diffraction of the Gaussian beam was slightly more pronounced in the experiment, while it turned out to decrease rather quickly with increasing intensities in the numerical simulations [the beam power was more than doubled from Figure 4.7 (a) to (b), but only raised by 50% from (d) to (e)]. Similar effects have been observed when the simulations were repeated

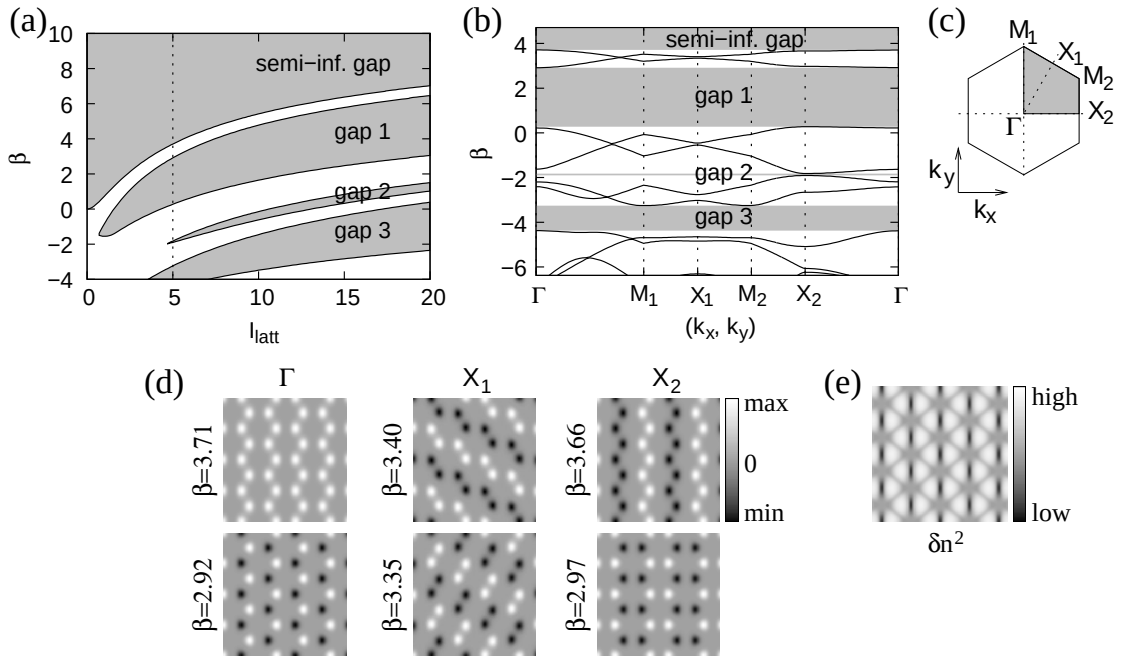

Figure 4.8: Vertical triangular lattice (focusing nonlinearity, $E_{ext} = 2.5\,\mathrm{kV/cm}$): (a) dependency of the band structure on the lattice strength; (b) band structure [$I_{latt} = 5$, dotted line in (a)]; (c) first Brillouin zone; (d) Bloch modes (amplitude profiles) from the first band at the Γ, X_1, and X_2 points; (e) lattice structure (δn^2).

with Gaussian beams.

By contrast, the diffraction of the dipole beam was weaker in the experiment. In this case higher powers were required in the simulations in order to reproduce the intermediate states [factor 4 between Figure 4.7 (j) and (k), but only factor 2.5 between (g) and (h)]. The low-intensity pictures (a), (d), (g), and (j) reflect the structure of the underlying Bloch modes. This confirms that indeed the *second* band has been excited by the dipole beam in the experiment.

4.2.3 Vertical triangular lattice

When looking at the band structure of the vertical triangular lattice [Figure 4.8 (a),(b)], two things are conspicuous: On the one hand there are less finite gaps than in the horizontal triangular lattice, and on the other hand the dispersion curves occur in pairs, which do not split up even at high values of I_{latt}.

The reason for both lies in the special structure of the lattice sites, which consist of two complementary, focusing "triangles" being separated by a strongly defocusing region [Figure 4.8 (e)]. Hence each Bloch mode occurs twice, one time with the

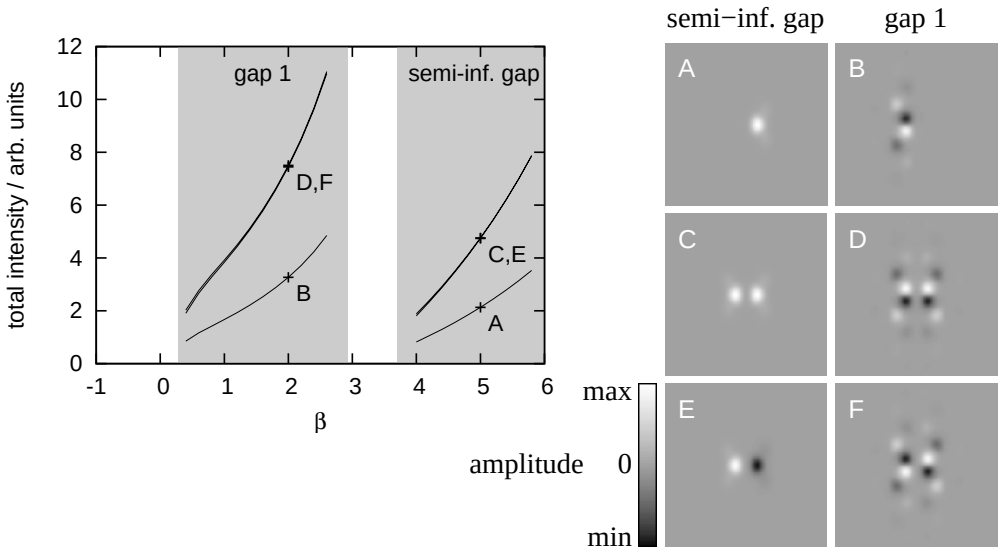

Figure 4.9: Total intensities (black lines) and amplitude profiles of the focusing basic (A,B) and higher-order (C-F) solitons in the vertical triangular lattice ($E_{ext} = 2.5\,\mathrm{kV/cm}$, $I_{latt} = 5$). The profiles A and B are dynamically stable.

same phase profile at *both* parts of the lattice sites, and another time with a phase difference of π between them. Due to the very low refractive index at the centers of the sites, the intensity of localized Bloch modes is also low there even if *no* phase jump occurs. Therefore Bloch modes, which differ only in whether showing such on-site phase jumps or not, have almost identical propagation constants [compare, e.g., the Γ point modes with the X_2 point modes in Figure 4.8 (d)].

By contrast, the refractive index *between* the lattice sites is higher. Thus a more significant contribution to the propagation constant of a particular mode arises from the phase difference between adjacent focusing areas of *different* lattice sites: If the phase is continuous, the intensity of a localized mode may take considerable values even between the sites, whereas a phase jump of π always implies a zero in the intensity profile. This can be seen when comparing Γ point modes or the X_2 point modes in Figure 4.8 (d) *among themselves*.

Due to the symmetry of the lattice, there are always points in each band where the number of phase jumps between adjacent lattice sites is the *same* for a pair of Bloch modes differing only in the occurrence of on-site phase jumps. Since such modes are (almost) degenerate, they are not separated by band gaps. This holds, for example, for the X_1 point modes. Because the (two-dimensional) dispersion relation is continuous along arbitrary paths in the Bloch space, which connect *all* modes shown in Figure 4.8 (d), also the Γ and the X_2 point modes cannot be separated by gaps.

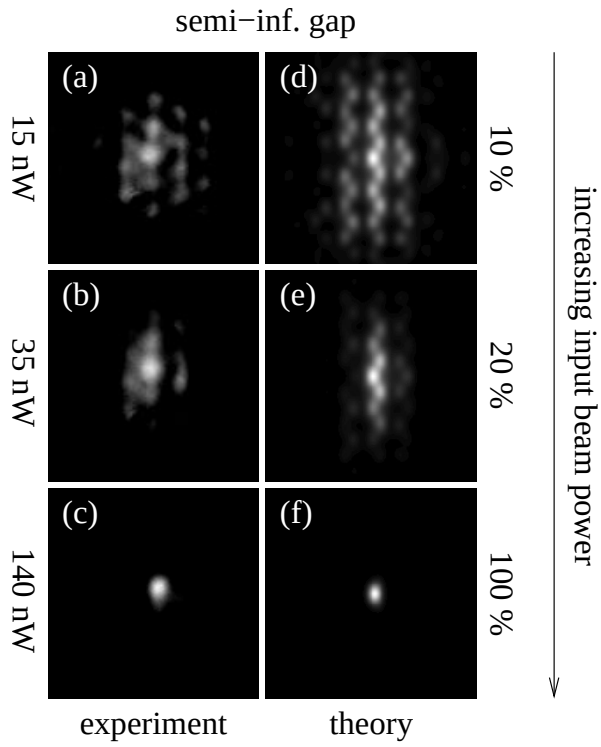

Figure 4.10: Formation of a fundamental ($B_0^{(foc)}$) soliton in the vertical triangular lattice ($z_{max} = 20\,\mathrm{mm}$). The percentages beside the theoretical pictures refer to the relative intensities with respect to the solitary beam shown in (f). Light gray tones denote high intensities. Experimental pictures by courtesy of Patrick Rose [42].

The special structure of the lattice sites is also reflected in the shape of the supported gap solitons [Figure 4.9]. The basic solitons of the semi-infinite and the first gap are given by the profiles A and B. Though they arise from only *one* part of a lattice site, it is always possible to mirror them onto the other part. Hence two other solitons can be derived from each basic one, which again differ only in either having an on-site phase jump (profiles E and F) or not (profiles C and D). The total intensity of those solitons is not affected by the phase jump, as it can be seen from the existence curves in the left part of Figure 4.9. For $I_{latt} = 5$, they turn out to be unstable however, in contrast to the basic ones.

Due to the quite low refractive index at the centers of the sites, vertical structures are favored by this lattice type (the refractive index gradient in that direction is smaller). This does not only become apparent from the orientation of the basic $B_1^{(foc)}$ solitons (B), but it is also visible when studying the gradual formation of fundamental solitons.

Similarly to the horizontal triangular lattice, this has been done both theoretically and experimentally by considering different input beam powers (Figure 4.10). At low intensities [cases (a),(d) and (b),(e)], it can be seen that the vertical diffraction dominates indeed. Nevertheless the focusing parts of the individual lattice sites are still distinguishable, even if the "zigzag" structure arising from the hexagonal symmetry is less pronounced in the experiment.

The theoretical parameters used are $E_{ext} = 1.5\,\mathrm{kV/cm}$ and $I_{latt} = 1$; again the values have been adjusted to match the experiment. In this case even the quantitative agreement is good.

4.3 Soliton clusters

Having studied single gap solitons in optically induced lattices, we now address the question whether it is possible to construct stable clusters of them in the same way as in the additive $\cos^2$ lattice (section 3.2). We do this exemplarily for the square vortex lattice.

We start with a *focusing out-of-phase* cluster with 9 lobes (Figure 4.11). As in section 4.2.1, we use a lattice strength of $I_{latt} = 5$. The amplitude profile [Figure 4.11 (c)] corresponds to a truncated $M_{1,2}$ point Bloch wave from the first band, hence the structure propagates in the semi-infinite gap ($\beta = 3$). The refractive index [Figure 4.11 (d)] is raised only at the centers of the lattice sites, since nonlocal effects lead to a diminution at the adjoining areas in x direction [cf. Fig. 2.2 (b)]. Compared to the additive $\cos^2$ lattice, the coupling between the lattice sites is much stronger in this example.

As Figure 4.11 (a) shows, the cluster does not propagate stable for $E_{ext} = 2.5\,\mathrm{kV/cm}$. At $z \approx 100 z_0$ slight oscillations of the lobes become visible, which finally lead to a destruction of the entire structure ($z \approx 170 z_0$). Subsequently most of the intensity is diffracted, whereas a certain part may be trapped as separated, fundamental solitons (in this example two of them occur in the final state).

The occurrence of this instability demonstrates that the reasoning given in section 3.2 provides only a *necessary* stability criterion. It does not cover the case that small perturbations of the intensity profile may become overcompensated if the coupling between the lattice sites is strong. This leads to intensity oscillations with growing amplitudes. However, the corresponding growth rates are usually much smaller than those obtained for the non-oscillatory instabilities of *focusing in-phase* clusters, which are highly unstable also in the square vortex lattice.

The oscillatory instability presented here may be suppressed by increasing the lattice strength. Figure 4.11 (b) shows that the out-of-phase cluster becomes stable for $E_{ext} = 4\,\mathrm{kV/cm}$ (due to the different band structure, a higher value was chosen also for β). This is not self-evident, since raising E_{ext} also increases the influence of the nonlinearity.

For *defocusing* nonlinearities, the results of section 3.2 state that in order to

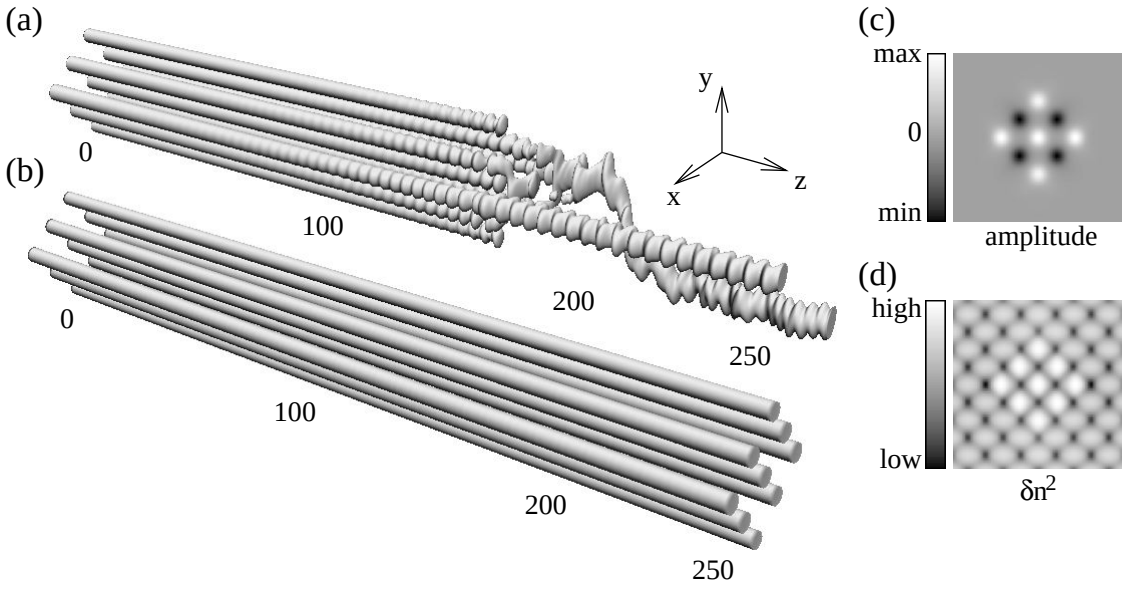

Figure 4.11: Out-of-phase soliton clusters in the square vortex lattice (focusing nonlinearity, $I_{latt} = 5$): (a) unstable propagation for $E_{ext} = 2.5\,\mathrm{kV/cm}$ and $\beta = 3$; (b) stabilization for $E_{ext} = 4\,\mathrm{kV/cm}$ and $\beta = 5$; (c) amplitude profile and (d) induced refractive index change (δn^2, including the probe beam) for $E_{ext} = 2.5\,\mathrm{kV/cm}$. z is measured in units of z_0.

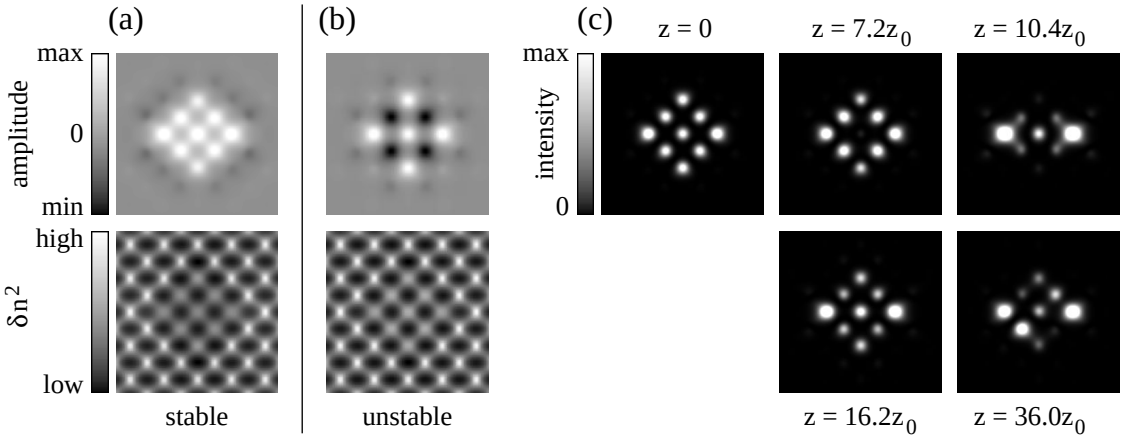

Figure 4.12: Soliton clusters in the square vortex lattice (defocusing nonlinearity, $E_{ext} = -2.5\,\mathrm{kV/cm}$, $\beta = -1$, $I_{latt} = 6$): (a) stable in-phase cluster; (b) unstable out-of-phase cluster (c) spatial evolution of the intensity profile of the out-of-phase cluster

obtain stable clusters, all lobes should have the same phase. Such structures can also be found in the square vortex lattice [Figure 4.12 (a)], again showing the characteristic side lobes of defocusing clusters which arise from the staggered phase structure of the underlying Bloch modes.

Also in this case the coupling between the lobes is rather strong. In combination with the anisotropy, this leads to a non-uniform intensity distribution: In the y direction, the middle lobes are brighter than the outer ones. However, this does *not* lead to different propagation constants within the cluster. It rather indicates that the picture of weakly coupled, identical lobes breaks down in this case due to nonlocal effects.

The *defocusing in-phase* cluster turns out to be stable for $I_{latt} = 6$ (case depicted here). Nevertheless, for weaker lattices ($I_{latt} = 5$) slight instabilities in the form of intensity oscillations occur also here, but only after long propagation distances ($z \gtrsim 300 z_0$). Hence they are different from the fast-growing modulational instability of the *defocusing out-of-phase* cluster [Figure 4.12 (b)]. The latter is especially pronounced for this lattice type due to the strong coupling: Some of the lobes almost vanish after short propagation distances ($z = 7.2 z_0$, $z = 10.4 z_0$) already. Nevertheless, the remaining intensity is still strong enough to preserve the phase information at the respective lattice sites. Therefore the original intensity profile becomes approximately restored at $z = 16.2 z_0$. In the further course of the propagation, this interplay is soon interrupted by a symmetry breaking ($z = 36.0 z_0$), even though the 9-lobe profile is maintained.

The results obtained in this section hold in a similar way also for clusters with more than 9 lobes. They may be transferred to other lattices as well, provided that the coupling between the lobes is not too strong.

5 Gap vortices and vortex clusters

The phase profiles of soliton clusters are not restricted to the values 0 and π, but they may also contain singularities. Such structures are commonly known as *vortex clusters*. As already mentioned in section 4.2.1 (Figure 4.4), vortices are connected with screw-like phase profiles yielding non-zero closed path integrals around the center. According to the definition (3.5), every continuous phase gradient involves a non-vanishing current density $\mathbf{J}$. Hence a vortex represents a circular intensity flow, which is associated with a certain angular momentum.

Due to the analogy between the propagation equation (2.11) and the Schrödinger equation, the total angular momentum L of a two-dimensional light distribution $A(x, y)$ can be defined equivalent to L_z in standard quantum mechanics:

$$L = \frac{1}{i} \int_{-\infty}^{\infty} \int_{-\infty}^{\infty} \left[A^*(x,y)\, x\, \partial_y A(x,y) - A^*(x,y)\, y\, \partial_x A(x,y) \right] \, \mathrm{d}x\mathrm{d}y. \tag{5.1}$$

In our scaling, a *homogeneous* vortex with the charge n possesses an angular momentum $L = n$. By contrast, for vortex clusters usually $|L| < |n|$ holds, even if they contain only one singularity. In this latter case, the angular momentum is most expressive. Since there is no continuous rotational invariance in the presence of a photonic lattice, this quantity is not conserved if the cluster becomes unstable. Therefore changes in the topological structure can be detected as changes in L. However, if the intensity distribution itself becomes non-stationary (i.e., the spots start to move around during the propagation), L does not necessary approach zero even if all vortices have disappeared.

Vortex clusters can be constructed by utilizing the fact that the phases of the individual lobes can be chosen quite independently, if the coupling between them is weak enough. They are *discrete* realizations of singular phase profiles spanning multiple lattice sites, whereas the phase is almost constant across each lobe [39,40]. This is contrary to the vortex shown in Figure 4.4 (b), which is located at a *single* lattice site.

Within this thesis, we use the expression *vortex cluster* for structures with one or more vortices, which are composed of *fundamental* gap solitons (lobes). These propagate always in the semi-infinite gap for focusing media, and in the first one for defocusing media. The term *gap vortex* has originally been introduced for a vortex cluster with a *single* phase singularity [58]. In the following we expand this definition to include both vortex clusters containing a *single* vortex and *non-discrete* (e.g., single-site) vortices in arbitrary band gaps.

5.1 Necessary stability criterion

In order to be dynamically stable[1], all intensity flows must be balanced within a gap vortex or a vortex cluster. Provided that the lattice is deep enough, two adjacent lobes can be treated approximately as bell-shaped intensity profiles with the homogeneous phases ϕ_1 and ϕ_2, which are coupled only by means of their evanescent fields. Under this assumption, a simple phase condition can be derived for a stable vortex cluster, as we will briefly sketch in the following.

Since the intensity is low in the region between the lobes, the total optical amplitude can be written as a linear superposition:

$$A(x) = A_1 e^{i\phi_1} e^{-\xi(x+\delta x)} + A_2 e^{i\phi_2} e^{\xi(x-\delta x)} \quad \text{for} \quad |x| \ll \delta x. \tag{5.2}$$

Herein we chose (without loss of generality) an 1D notation where the lobes are located at $x = \pm\delta x$; the 2D generalization is straightforward. The real constants A_1 and A_2 are proportional to the maximum amplitudes of the lobes. Hence we obtain with the definition (3.5)

$$\begin{aligned} J_x &= 2\mathrm{Im}(A\partial_x A^*) = 2\mathrm{Im}\left(\xi A_1 A_2 e^{-2\delta x}\left(e^{i(\phi_1-\phi_2)} - e^{i(\phi_2-\phi_1)}\right)\right) \\ &= 4\xi A_1 A_2 e^{-2\delta x}\sin(\phi_1 - \phi_2). \end{aligned} \tag{5.3}$$

Therefore the intensity flow between the two lobes is proportional to the sine of their phase difference. The same result is obtained in two transverse dimensions after integrating along the y axis.

The intensity flows within a cluster are balanced, if the intensities of the lobes do not change in the course of the propagation. Hence the sum of all intensity flows must vanish for each lobe [59]:

$$\sum_{i=1}^{N} c_{ij}\sin(\phi_i - \phi_j) \stackrel{!}{=} 0 \quad \text{for all } i \text{ with } 1 \le i \le N. \tag{5.4}$$

Herein all constants of proportionality have been collected to the coupling coefficients c_{ij}, where i and j denote the respective lobes. All lobes must have equal intensities, since otherwise their propagation constants would be different, and the phase differences could no longer be preserved. The c_{ij} may be determined by assigning well-defined phases to the lobes and calculating the resulting intensity flows numerically. However, the approximate formula given for them in [59] is not applicable for the anisotropic model (2.23).

5.2 Elementary vortex clusters (focusing nonlinearity)

The simplest vortex clusters consist of three lobes forming a triangle [Fig. 5.1 (a)]. They are obtained most naturally in lattices with a regular hexagonal symmetry,

[1] We call a vortex *stable*, if both its intensity and its phase distribution are conserved during the propagation.

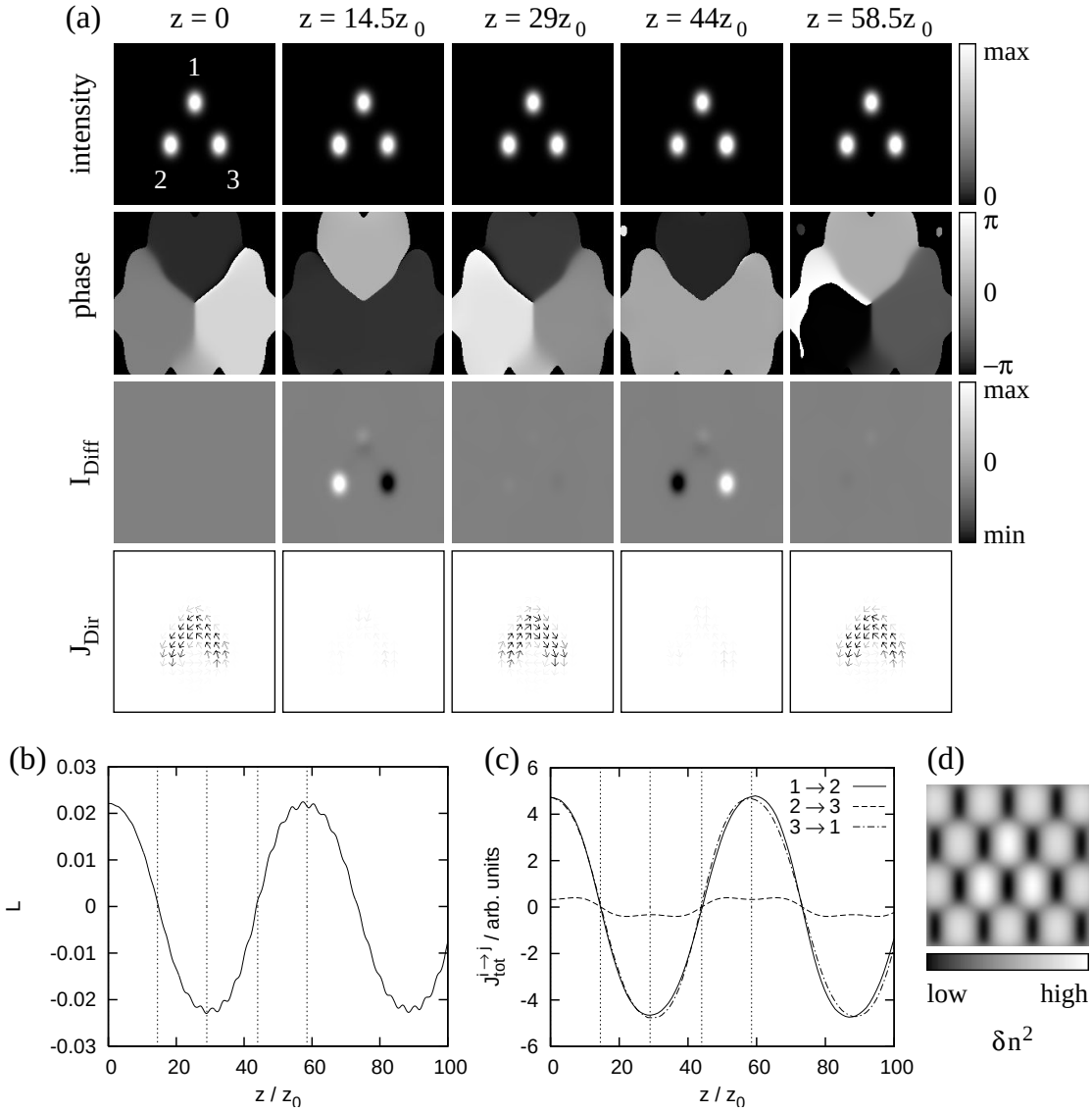

Figure 5.1: Charge flipping effect for an elementary vortex cluster (3 lobes, initial phase difference $2\pi/3$, $\beta = 5$) in the horizontal honeycomb lattice (focusing nonlinearity, $E_{ext} = 2.5\,\mathrm{kV/cm}$, $I_{latt} = 4$, $k'_x/k'_y = \sqrt{3}$). (a) from top to bottom: intensity, phase, difference to the initial intensity profile [$I_{Diff} = I(z) - I(z=0)$], and direction field of the intensity current density $\mathbf{J}$ (dark arrows indicate high values of $|\mathbf{J}|$); (b) angular momentum; (c) total intensity flux between the lobes; (d) induced refractive index change (δn^2, including the probe beam). Vertical lines in (b) and (c) indicate the positions depicted in (a).

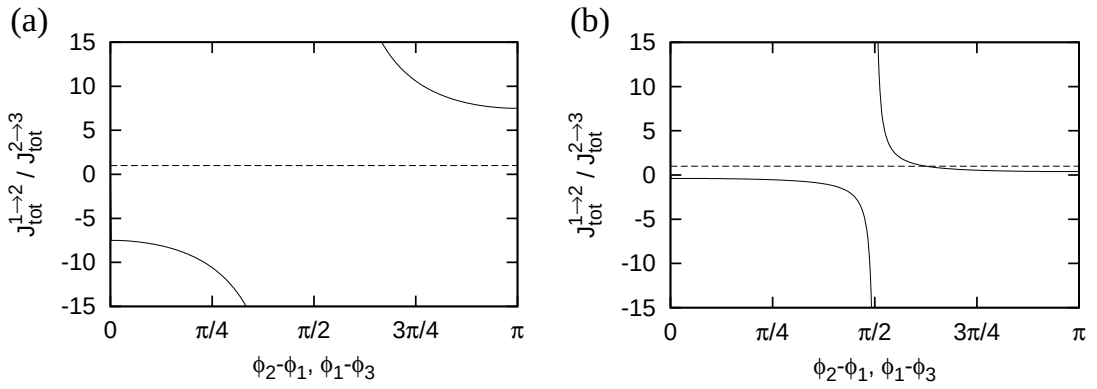

Figure 5.2: Ratio of the total intensity fluxes in dependence of the phase differences between the lobes ($\phi_2 - \phi_1 = \phi_1 - \phi_3$): (a) regular honeycomb lattice ($k'_x/k'_y = \sqrt{3} \approx 1.73$); (b) stretched honeycomb lattice ($k'_x/k'_y = 2.75$). Other parameters as in Figure 5.1. The dashed lines correspond to a balanced intensity flow ($J_{tot}^{1\to2}/J_{tot}^{2\to3} = 1$).

such as in the (unstretched) horizontal honeycomb lattice [57]. In this case the lattice sites form *equilateral* triangles. Hence for an isotropic nonlinearity, all coupling coefficients c_{ij} are equal, and the flow condition (5.4) can be fulfilled easily by setting all phase differences equal to $2\pi/3$.

However, this is not the case for the anisotropic model. As it can be seen from the Figures 5.1 (a) [J_{Dir} at $z = 0$] and (d), the refractive index is much lower between the lobes 2 and 3 than between 1 and 2 or 1 and 3. Thus, we have $c_{12} = c_{13} \gg c_{23}$ for $d_x = 30\mu$m and $k'_x/k'_y = \sqrt{3}$ (unstretched lattice). Since the phase differences between all lobes were chosen to be initially equal, the ratio c_{12}/c_{23} is given by the ratio $J_{tot}^{1\to2}/J_{tot}^{2\to3} \approx 15$ at $z = 0$ [Figure 5.1 (c)]. Herein $J_{tot}^{i\to j}$ denotes the total intensity flow between the lobes i and j. It is determined numerically by calculating the path integral $J_{tot}^{i\to j} = \int_S \mathbf{J}\mathrm{d}\mathbf{s}$, where the path S is the half line starting at the vortex center and crossing the connecting line of the lobes i and j in the middle.

The unequal coupling constants lead to a net transfer of intensity from lobe 3 to lobe 2 via lobe 1, since the phase singularity is positive [see the direction field J_{Dir} in Figure 5.1 (a)]. Hence the intensity of lobe 2 slowly increases in the course of the propagation, while lobe 3 becomes darker. The flow condition (5.4) is still fulfilled for the lobe 1 however, so its intensity remains almost unchanged.

Due to the focusing nonlinearity, the propagation constants of the lobes increase or decrease in the same way as their intensities. Hence the phase differences $\phi_2 - \phi_1$ and $\phi_1 - \phi_3$ increase as well, while $\phi_3 - \phi_2$ becomes smaller. According to equation (5.3), this finally leads to a decrease of the intensity flow between *all* lobes as $\phi_2 - \phi_1, \phi_1 - \phi_3 \to \pi$ and $\phi_3 - \phi_2 \to 0$. At $z \approx 14.5 z_0$, all $J_{tot}^{i\to j}$ are zero, and the phase singularity has disappeared. However, the slight intensity difference between the lobes 2 and 3 is still there, so the change of the phase differences goes on, and

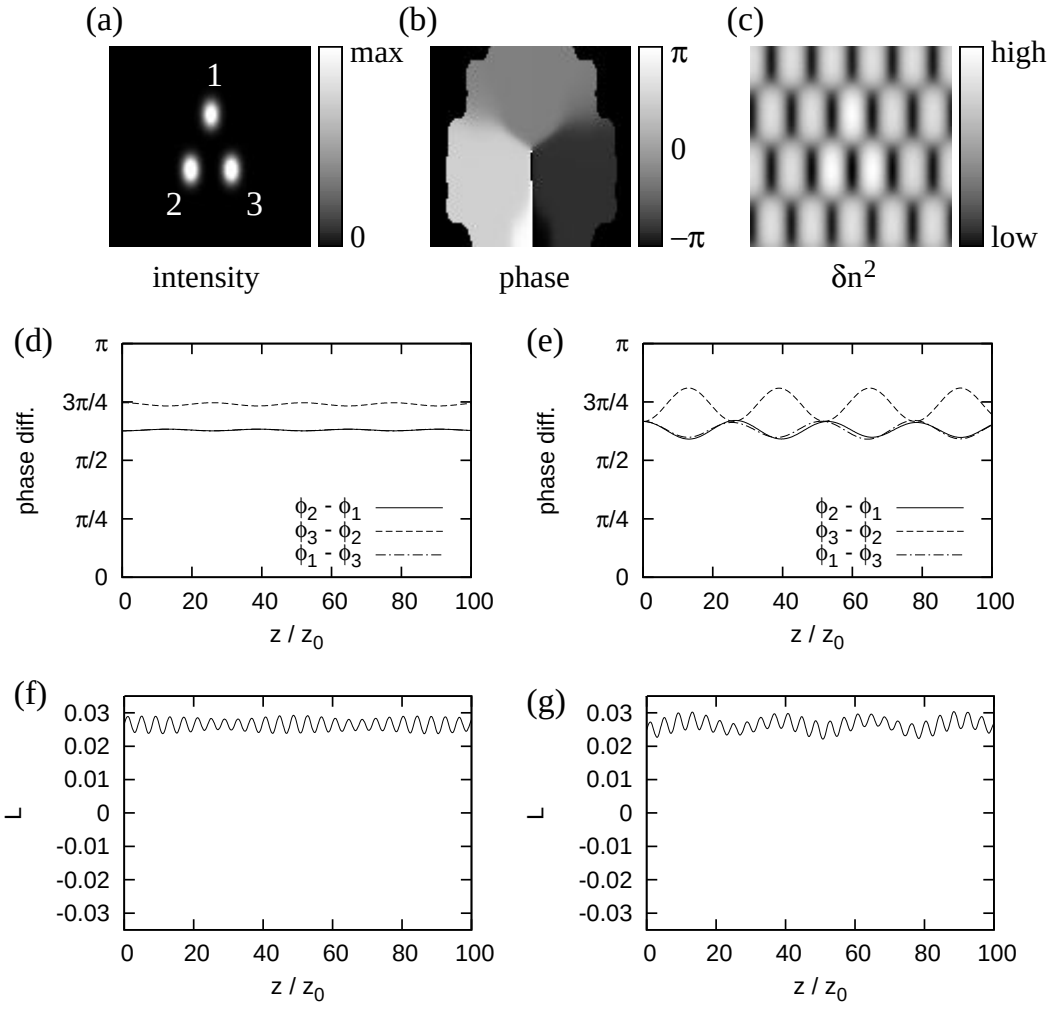

Figure 5.3: Stretched honeycomb lattice ($k'_x/k'_y = 2.75$, $E_{ext} = 2.5\,\mathrm{kV/cm}$, $I_{latt} = 4$): (a) intensity, (b) phase, (c) induced refractive index change (δn^2, including the probe beam), (d) phase differences, and (e) angular momentum for a stable vortex cluster ($\beta = 5$) with an adjusted phase profile ($\phi_2 - \phi_1 = \phi_1 - \phi_3 = 0.627\pi$); (e), (g) same as (d) and (f) for an initial phase difference of $2\pi/3$ between all lobes.

a new phase singularity with an opposite sign arises. This coincides with a change of sign of the total angular momentum [Figure 5.1 (b)]. The directions of the intensity flows are reversed as well, so the intensity difference decreases again until the original situation has been restored ($z \approx 29 z_0$), but with an inverted phase structure. Since the system still features a mirror symmetry along the vertical axis through the vortex center, the above process proceeds in a reversed manner, until the initial state is restored again, this time *including* the sign of the vortex ($z \approx 58.5 z_0$).

This phenomenon is called *charge flipping*. It has been first published in [59] in the context of asymmetric vortices, using isotropic lattices and nonlinearities. In this example the intensity flows were balanced, so the charge flipping effect had to be triggered by an external, finite perturbation. Subsequently, the phenomenon was also observed in simulations and experiments with ring vortices in square lattices [60]. In our case it recurs over many periods, while the period length remains almost constant.

This raises the question, whether it is possible at all to create a *stable* vortex in a strongly anisotropic lattice, i.e., to fulfill the condition (5.4) for all lobes. Figure 5.2 (a) shows that this is not the case for the situation depicted in Figure 5.1: Obviously, the differences $\phi_2 - \phi_1$ and $\phi_1 - \phi_3$ have to be equal in order to retain the mirror symmetry given by the lattice. The ratio $J_{tot}^{1\to2}/J_{tot}^{2\to3}$ is always larger than 1 however, although it decreases monotonically as $\phi_2 - \phi_1 \to \pi$.

This result agrees with [59], which states that a vortex solution of equation (5.4) with $c_{12} = c_{13}$ exists only, if $c_{12}/c_{23} < 2$. This cannot be achieved for a regular honeycomb lattice however, so the ratio k'_x/k'_y has to be increased in order to reduce the (relative) distance between the lobes 2 and 3. As shown in Figure 5.2 (b), a nontrivial solution of (5.4) is found indeed for $k'_x/k'_y = 2.75$ (corresponding to $d_x = 20\mu$m and $d_y = 55\mu$m). The corresponding vortex is depicted in Figure 5.3 (a) and (b); the respective phase differences are $\phi_2 - \phi_1 = \phi_1 - \phi_3 = 0.627\pi$ and $\phi_3 - \phi_2 = 0.746\pi$. The stretched profile of the lattice is clearly visible [Figure 5.3(c)].

Apart from slight, but stationary oscillations of the angular momentum [Figure 5.3(f)], this vortex propagates stable indeed. When crossing the dashed line in Figure 5.2 (b), the ratio $J_{tot}^{1\to2}/J_{tot}^{2\to3}$ is always changed such that small phase perturbations are balanced. This is demonstrated in the Figures 5.3 (e) and (g) by setting all initial phase differences equal to $2\pi/3$ again (all other parameters remain unchanged). Now small oscillations around the stationary values are visible, but charge flips still do not occur. In this example, they cannot be induced for *any* choice of the initial phase differences yielding a phase singularity, as long as $\phi_2 - \phi_1 = \phi_1 - \phi_3$. However, this becomes possible for $\phi_3 - \phi_2 \approx \pi$, if the ratio c_{12}/c_{23} is still less than, but close to 2.

Since the essential dynamics are described by the relations (5.3) and (5.4), the actual shape of the lattice is less decisive for the dynamics than its geometry: Similar results can be obtained for stretched vortex lattices (see chapter 4.1) as well. The same holds for the triangular lattices, though the quotient k'_x/k'_y cannot be varied in this case. This results in a rather fixed ratio c_{12}/c_{23}, being either much greater than 2 (horizontal triangular lattices) or much less than 2 (vertical triangular lattices). Hence only in the latter case stable vortex clusters can be found. These are composed of the fundamental solitons shown in Figure 4.9 A, thus only one half of each lattice site is occupied. However, the large difference of c_{12} and c_{23} requires a strongly adjusted phase profile, resulting in $\phi_3 - \phi_2 \approx \pi$.

Therefore these vortices are quite sensitive against small perturbations, since the singularity is lost if $\phi_3 - \phi_2 < \pi$. This leads to a bad localization of the vortex centers.

5.3 Multivortex clusters

5.3.1 Clusters with triangular shape

Having studied the charge flipping effect of elementary vortex clusters, we now consider structures with multiple phase singularities. Figure 5.4 exemplarily shows a triangular cluster with 15 lobes and 16 vortices (10 positive and 6 negative ones). It can be regarded as a continuation of the 3-lobe cluster; the negative vortices are obtained as mirror images of the positive ones. Such structures arise from the $M_{1,2}$ point Bloch waves in the first band. Being another example of truncated nonlinear Bloch waves, they may take arbitrary sizes and shapes. Many of them are stable in combination with isotropic nonlinearities [57], as long as the the phase differences between lobes on adjacent lattice sites equal $2\pi/3$.

Such structures can also be stabilized in anisotropic media, if – according to the previous section – a lattice with appropriate c_{ij} is chosen. However, the charge flipping processes may become rather complex for *regular* (i.e., unstretched) honeycomb lattices. This is demonstrated in Figure 5.4, using the same parameters as in Figure 5.1. The initial phase differences between adjacent lobes have been set equal to $2\pi/3$.

Due to the strong anisotropy, there is no effective intensity transfer along horizontal lines (i.e., parallel to the x axis). This leads to a zigzag-shaped intensity flow along each row of lobes. Since all initial phase differences are equal, the same holds for $J_{tot}^{i\to j}$ between two diagonally adjacent lobes along these zigzag lines. Thus the net change of intensity almost vanishes for the inner lobes, which have an *even* number of diagonal neighbors (two for the bottom row and for the topmost lobe, otherwise four). However, this number is *odd* for the lobes at the left and the right borders of the cluster, hence their intensities cannot remain constant. In agreement with the positive total charge (+4) and the positive angular momentum of the cluster, the net intensity flow points away from the right border and towards the left one.

Of course, this picture holds in a strict sense only for $z = 0$, as the phase differences are altered owing to the transfer of intensity. At $z = 17z_0$, the phase difference between the inner part of the cluster and the left and right borders has become equal to π. Consequently, there is no exchange of intensity between them anymore, and the outer vortices have vanished. According to the above picture, the intensity differences are less pronounced in the inner part, where the phase differences are closer to the initial ones yet. Hence the cluster transiently resolves into a smaller one, consisting of six inner lobes and four vortices, and a boundary

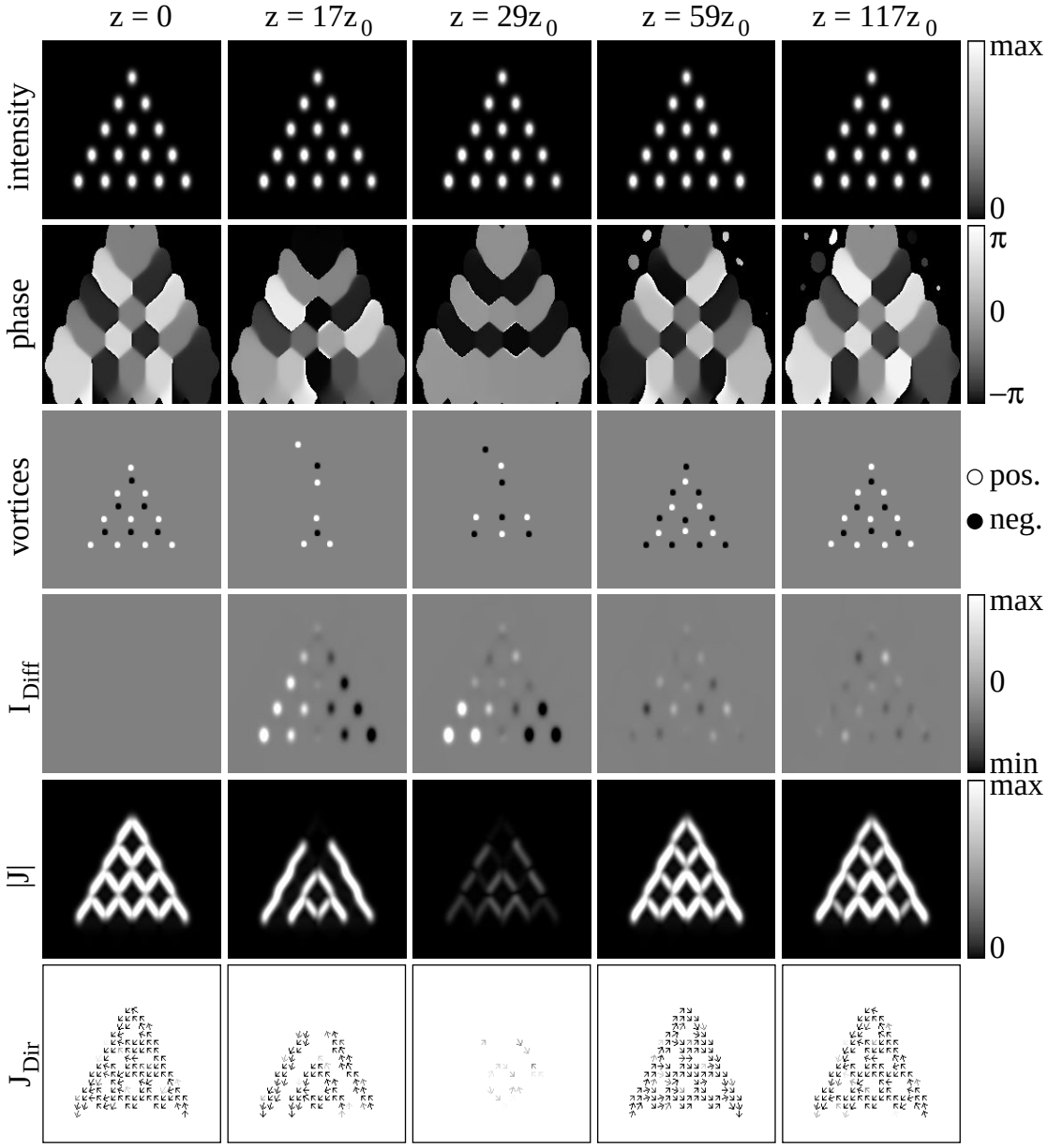

Figure 5.4: Charge flipping effect for a vortex cluster with 15 lobes (16 vortices, total charge 4, initial phase difference $2\pi/3$) in the regular, horizontal honeycomb lattice (other parameters as in Figure 5.1). From top to bottom: intensity, phase, positions of the vortex centers, difference to the initial intensity profile $[I_{Diff} = I(z) - I(z = 0)]$, $|\mathbf{J}|$, and direction field of $\mathbf{J}$ (dark arrows indicate high values of $|\mathbf{J}|$);

part. Now the intensity flow is unbalanced for the boundary lobes of the *inner* cluster as well, thus leading to a further shift of intensity from the right to the left within that structure. This process stops at $z = 29z_0$, when the phase difference between all rows of lobes has approximately reached π. Since this does not hold exactly, there are still some vortices present, which are just about to reverse their signs.

Subsequently, the shifting of the phases proceeds mirror-inverted due to the changed propagation constants, similar to the 3-lobe cluster shown in Figure 5.1. At $z = 59z_0$, the original intensity profile has been largely restored, whereas all vortices have changed their signs. Now the reversed process sets in, until the original structure is recovered at $z = 117z_0$. Also in this case the charge flipping cycle periodically repeats several times, despite the complexity of the underlying steps.

Similar processes are also observed for larger clusters with a triangular shape. The charge inversion always starts at the left and the right borders, and the cluster subsequently resolves into smaller ones as soon as the exchange of intensity with the borders has become small. The initial state periodically recurs after a constant propagation distance.

5.3.2 Clusters with hexagonal shape

In the previous section we have seen that it is crucial for the dynamics of a vortex cluster, whether a lobe has an odd or an even number of neighbors. In this context we count only those lobes as neighbors, which have a significant, *direct* exchange of intensity with the considered lobe.

For clusters with a *triangular* shape, the number of neighbors is always even, if all c_{ij} are equal. Hence in order to obtain a stable cluster, all $J_{tot}^{i\to j}$ have to be made equal as well by choosing an appropriate phase profile. This is still possible if the c_{ij} along the c axis differ from those along the diagonal directions, provided that they are not more than twice as high.

This is crucially different for clusters with a *hexagonal* shape, such as the one shown in Figure 5.5 (a)-(c) [61]. This cluster consists of seven lobes, six outer ones arranged in a hexagon around the center one. The phase profile again follows that of the $M_{1,2}$ point Bloch modes, thus forming three positive and three negative vortices.

In this case the outer lobes have *three* neighbors, whereas the inner one has six; again all c_{ij} presumed to be equal. Therefore a balanced intensity flow can be achieved only, if the flows between the center lobe and each outer one are exactly twice as high as those among the outer lobes themselves. Being subject to this constraint, the flow condition (5.4) permits stable vortex solutions only if all c_{ij} are equal.

For the horizontal honeycomb lattice and the parameters given in Figure 5.5 (h)-(n), this can be achieved if $k'_x/k'_y \approx 2.5$ ("stretched" honeycomb lattice, in this

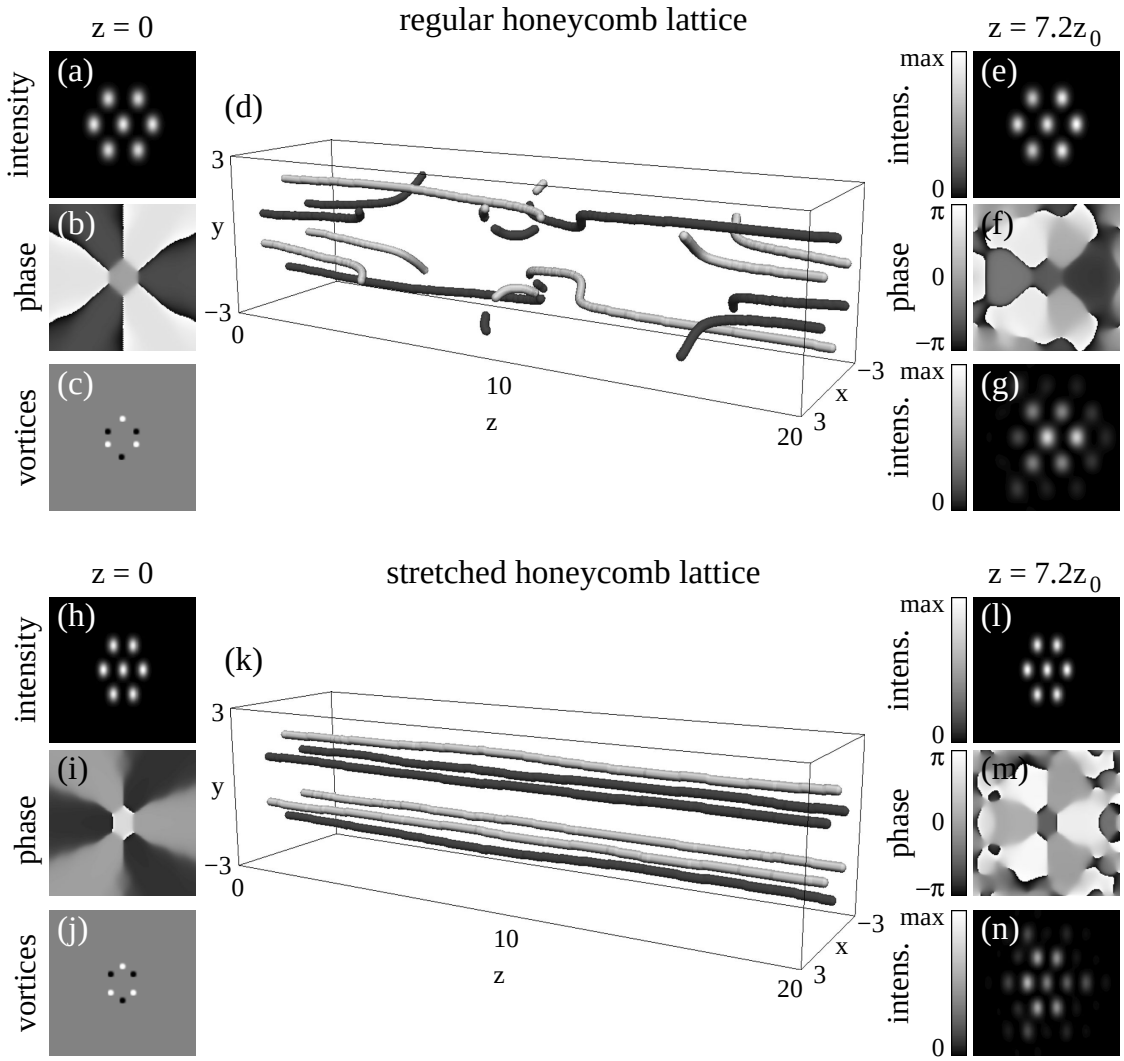

Figure 5.5: Stabilization of a vortex cluster with 7 lobes and 6 vortices (total charge 0).
Top part: Unstable propagation in a regular honeycomb lattice (E_{ext} = 1.5 kV/cm, $I_{latt} = 1$, $\beta = 1.5$). (a)-(c) intensity, phase, and vortex distribution (black = negative charge, white = positive charge) of the input beam (d) vortex dynamics, (e) and (f) intensity and phase after propagation in the nonlinear regime, (g) intensity after propagation in the low-intensity (quasi-linear) regime [the pictures (e)-(g) are taken at $z = 7.2z_0$].
Bottom part: Stable propagation in a stretched honeycomb lattice ($k'_x/k'_y = 2.5$, $E_{ext} = 2.5\,\mathrm{kV/cm}$, $I_{latt} = 1$, $\beta = 3$). The pictures (h)-(n) correspond to (a)-(g). z is measured in units of z_0; x and y are measured in units of w_0.

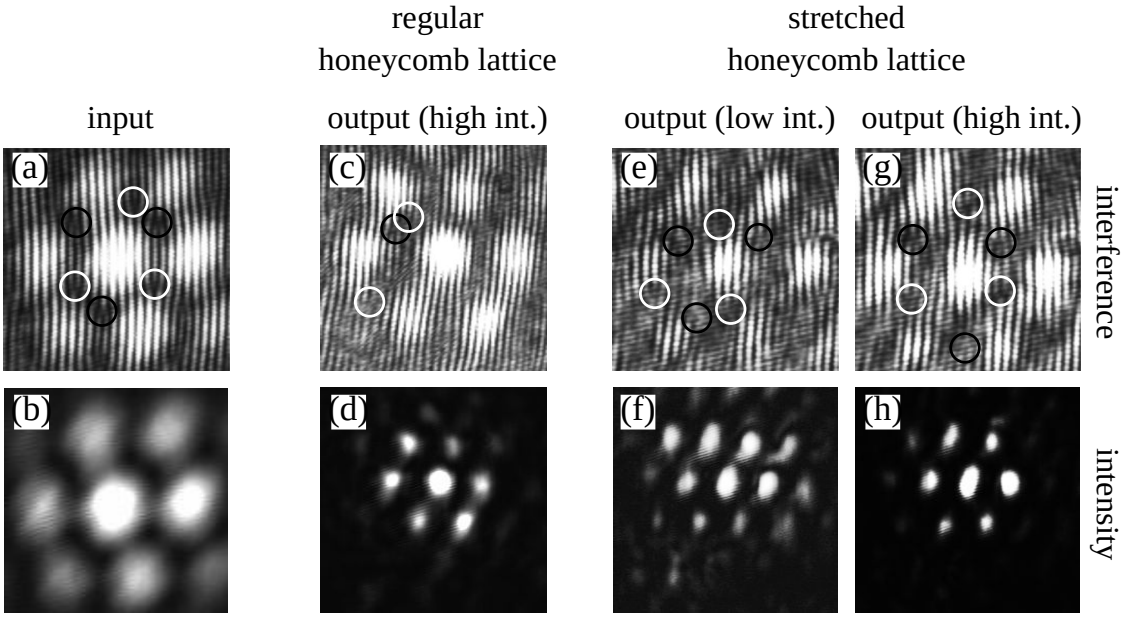

Figure 5.6: Experimental realization of the 7-lobe cluster. Top row: interference of the probe beam with a tilted plain wave; positive (negative) vortices appear as (inverted) Y-shaped forks. They are marked by white (black) circles if they lie inside the cluster. Bottom row: intensity profiles of the probe beam; light gray tones denote high intensities. (a), (b) input beam; (c), (d) output beam for the regular honeycomb lattice; (e), (f) output beam for the stretched honeycomb lattice ($k'_x/k'_y \approx 2.5$) in the low-intinsity (quasi-linear) regime; (g), (h) same as (e), (f) in the high-intensity (nonlinear) regime. The total propagation distance was 15 mm ($\approx 5.4 z_0$). Pictures by courtesy of Bernd Terhalle [61].

example $d_x = 20\mu$m and $d_y = 50\mu$m have been used). As it can be seen from the vortex trajectories (k) and the beam profile at $z = 7.2z_0$ [(l), (m)], the propagation is indeed stable in this case.

The diffraction image (n) has been calculated for an identical phase profile, though assuming that the total intensity is very low. Thus it confirms that self-guiding effects play an important role in (l) and (m). The phase differences between the lobes are *not* equal to $2\pi/3$ in order to fulfill the special flow constraint for the outer lobes.

Since this flow constraint cannot be fulfilled for *any* phase distribution in a *regular* honeycomb lattice, a more complicated vortex dynamics is expected in this case. This is demonstrated in Figure 5.5 (a)-(g), where all initial phase differences have been set equal to $2\pi/3$. The four vortices at the sides of the structure leave the cluster rather soon [Figure 5.5 (d), $z \approx 4z_0$)], so that at $z = 7.2z_0$ only the top and bottom vortices remain [situation in Figure 5.5 (e) and (f)]. Subsequently, these remaining vortices change their signs in a rather complex process around $z \approx 10z_0$: After four pairs of new vortices have been created near the boundaries of the cluster, one vortex of each pair immediately leaves the cluster. Two of the remaining four new vortices annihilate with the original top and bottom ones, whereas the other two inherit the top and bottom positions with reversed signs. At $z \approx 16.5z_0$, also the four vortices at the sides reappear with altered signs. They arise from pair creations outside of the cluster.

Hence, also in this case a complete charge flip of the cluster is observed, which is reversed again in the further course of the propagation (the latter is not shown here). As explained in section 5.2, this is a direct consequence of the anisotropic nonlinearity. In the stretched honeycomb lattice [Figure 5.5 (a)-(g)], even a "non-adjusted" phase distribution with $2\pi/3$ phase differences does not lead to a charge flip scenario.

Figure 5.5 (d) shows another special feature of the 7-lobe cluster, which is caused by the vanishing total charge: The resulting total angular momentum of zero is maintained throughout the propagation, hence positive and negative vortices enter or leave the cluster always in pairs. However, in this example the lattice is too weak to hold the cluster permanently together; at $z \approx 130z_0$ the intensity profile becomes destroyed due to modulational instabilities (not shown here). This can be prevented for stronger lattices.

The numerical parameters chosen in Figure 5.5 have been adjusted in order to match the experiments depicted in Figure 5.6. These confirm the significant difference between the regular and the stretched honeycomb lattice: Within the former [Figure 5.6 (c), (d)], it was not possible to conserve the six vortices of the input beam [(a), (b)]. Nearly all of them left the structure or disappeard by pair annihilation. Moreover, the phase structure of the ouput beam turned out to be very sensitive to small perturbations.

On the contrary, the vortex profile became rather robust when the lattice was

stretched in the y direction [Figure 5.6 (g), (h)], though no special phase adjustments had been made to the input beam, so the intensity flow was not completely balanced. In combination with the results obtained in the unstretched lattice, this is a direct experimental proof that anisotropic effects play an important role also in the horizontal honeycomb lattice.

Additionally it was proven that the total propagation distance (15 mm, approximately corresponding to $5.4z_0$) was long enough to show nonlinear effects: Lowering the input intensity indeed lead to a pronounced diffraction of the beam [Figure 5.6 (f)], while the positions of the vortices changed noticeably (e). Nevertheless, the original vortex profile can be identified yet.

5.4 Defocusing vortex clusters

The stability properties of a vortex cluster with three lobes fundamentally change, if the sign of the nonlinearity is altered (Figure 5.7). Even though the ratio of the coupling strengths of $c_{12}/c_{23} \approx 0.85$ in this example does allow a balanced intensity flow for $\phi_2 - \phi_1 = \phi_1 - \phi_3 = 0.64\pi$, the system does not remain in such a state if started with that phase distribution. Instead, the vertical mirror symmetry implied by $\phi_2 - \phi_1 = \phi_1 - \phi_3$ is broken right from the start, and the vortex is lost rather soon ($z \approx 12.8z_0$) as $\phi_3 - \phi_2$ becomes larger than π [phase jump $\pi \rightarrow -\pi$, vertical line of the dashed curve in Figure 5.7 (c)]. In contrast to focusing clusters with an unbalanced intensity flow, the vortex is *not* recovered, neither with a positive nor with a negative charge[2].

In this example the initial value of $J_{tot}^{2\rightarrow3}$ is slightly smaller than those of $J_{tot}^{1\rightarrow2}$ and $J_{tot}^{3\rightarrow1}$. Similar scenarios occur however, if $J_{tot}^{2\rightarrow3} > J_{tot}^{1\rightarrow2} = J_{tot}^{3\rightarrow1}$, with the only exception that $\phi_3 - \phi_2$ initially decreases, while the other phase differences increase. Nevertheless, the vortex vanishes also in this case.

Hence the fixed point corresponding to $J_{tot}^{1\rightarrow2}/J_{tot}^{2\rightarrow3} = 1$ [cf. Figure 5.2 (b)] is obviously unstable in conjunction with defocusing nonlinearities. This can be understood in the following way: Let us assume that $J_{tot}^{1\rightarrow2} = J_{tot}^{3\rightarrow1}$ (vertical mirror symmetry) at first. If $J_{tot}^{2\rightarrow3}$ is slightly smaller (i.e., the above fraction is slightly larger than 1), the second lobe will gain some intensity during the propagation, whereas the third one becomes darker. This is the initial situation in Figure 5.1 (cf. the pictures at $z = 12z_0$). Due to the *defocusing* nonlinearity, the propagation constant of the brighter lobe is *decreased* however, while that of the darker lobe is increased. This leads to a diminution of the phase differences $\phi_2 - \phi_1$ and $\phi_1 - \phi_3$, hence $\phi_3 - \phi_2$ grows until reaching π. At this point the direction of $J_{tot}^{2\rightarrow3}$ reverses, and the vortex is lost.

A similar scenario is obtained, if $J_{tot}^{2\rightarrow3}$ is initially taken to be larger than $J_{tot}^{1\rightarrow2} = J_{tot}^{3\rightarrow1}$. In this case $\phi_3 - \phi_2$ decreases, whereas $\phi_2 - \phi_1$ and $\phi_1 - \phi_3$ grow.

[2]For different parameters the vortex may transiently reappear, but only as a consequence of already irregular phase dynamics. These cases are rare however.

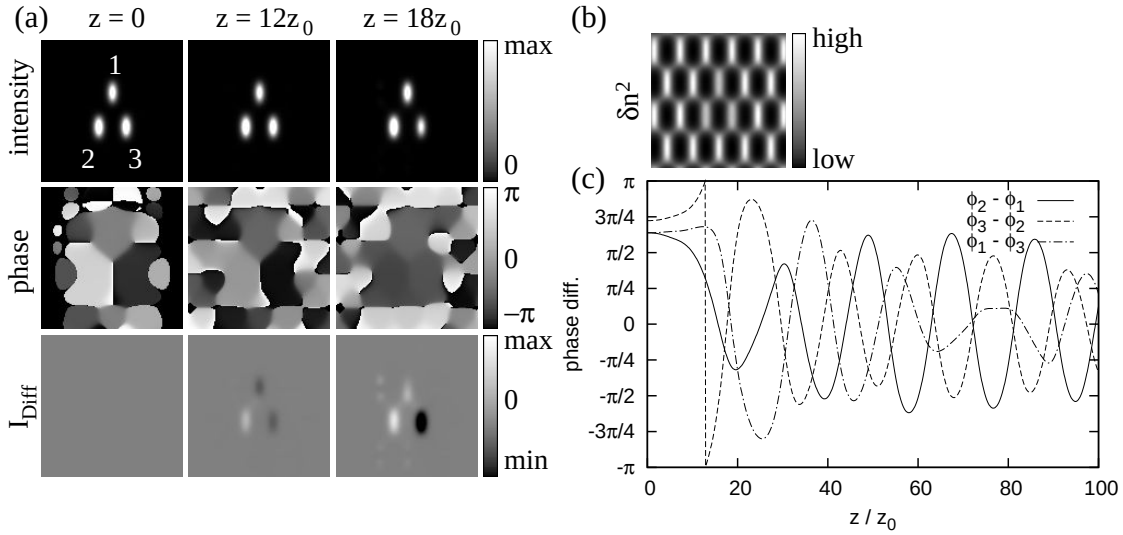

Figure 5.7: Defocusing vortex cluster in a stretched honeycomb lattice ($k'_x/k'_y = 2.5$, $E_{ext} = -2.5\,\mathrm{kV/cm}$, $I_{latt} = 4$, $\beta = 2$). (a) from top to bottom: intensity, phase, and difference to the initial intensity profile [$I_{Diff} = I(z) - I(z = 0)$], (b) induced refractive index change (δn^2, including the probe beam), (c) phase differences.

In order to understand the vertical symmetry breaking in Figure 5.7, we have to consider a small perturbation of the equality $\phi_2 - \phi_1 = \phi_1 - \phi_3$. Let us assume, without loss of generality, that the right hand side is slightly larger. This implies that $J_{tot}^{3\to1} < J_{tot}^{1\to2}$, since both phase differences are larger than $\pi/2$ [cf. equation (5.3)]. Then the sum of the intensity flows away from and towards lobe 1 is negative; thus it becomes darker. Since this leads to an increase of its propagation constant, $\phi_1 - \phi_3$ increases as well, while $\phi_2 - \phi_1$ becomes smaller – the perturbation grows.

Together with the instability triggered by $J_{tot}^{2\to3} \lesssim J_{tot}^{1\to2} = J_{tot}^{3\to1}$, this is also observed in Figure 5.7 (c) for $z \leq 12.8 z_0$ (i.e., until the vortex is lost). As described above, the former leads to an additional, overall increase of $\phi_3 - \phi_2$ and to an overall decrease of the other phase differences.

5.5 Ring-shaped vortex clusters

One conclusion from the stability analysis in the previous section is that *defocusing* vortex clusters, which contain phase differences being *greater* than $\pi/2$, are dynamically unstable within the scope of the approximation (5.3). This is due to the fact that the sign of $\partial J_{tot}^{i\to j}/\partial(\phi_i - \phi_j)$ changes for $\phi_i - \phi_j = \pi/2$. Hence defocusing clusters with a balanced intensity flow should be stable, if all phase differences between adjacent lobes are *less* than $\pi/2$.

Additionally, the stability argument depends on the slope of the relation between

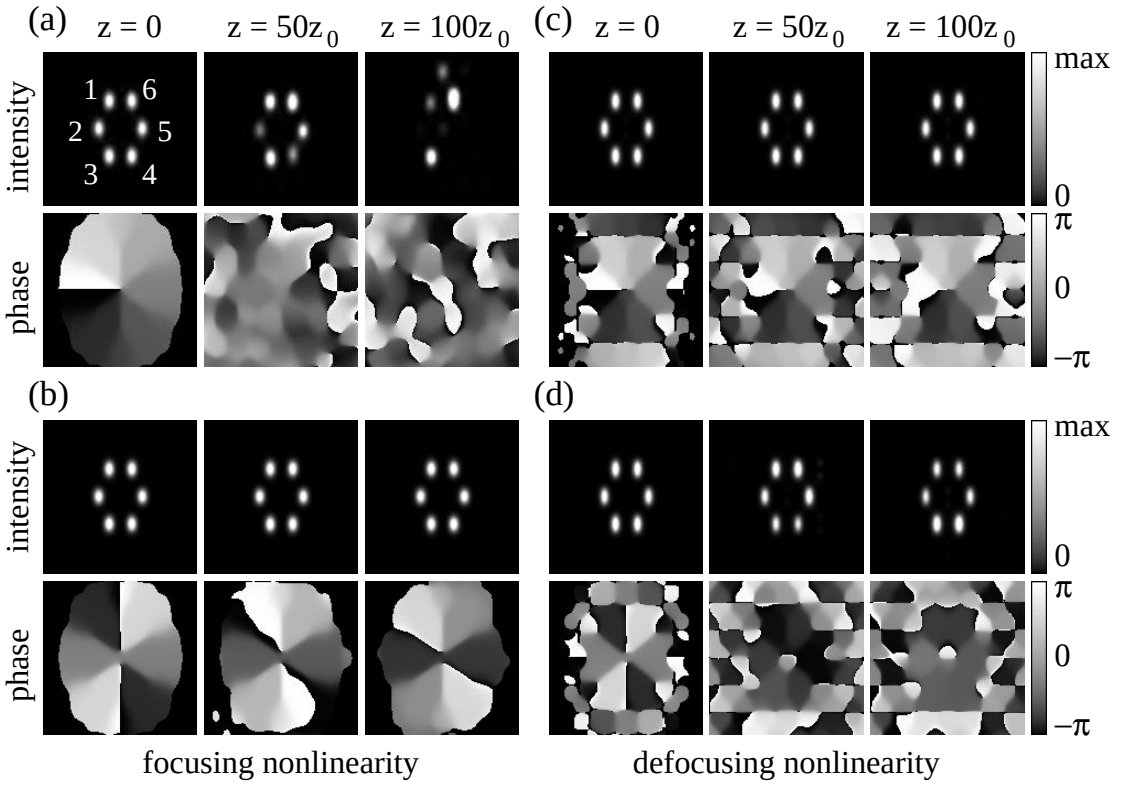

Figure 5.8: Ring-shaped vortex clusters in a stretched honeycomb lattice ($k'_x/k'_y = 2.5$). Left column [(a), (b)]: focusing nonlinearity ($E_{ext} = 2.5\,\mathrm{kV/cm}$, $I_{latt} = 1$, $\beta = 3$); Right column [(c), (d)]: defocusing nonlinearity ($E_{ext} = -2.5\,\mathrm{kV/cm}$, $I_{latt} = 4$, $\beta = 2$). Top part: total charge 1 (phase differences along the ring are less than $\pi/2$); Bottom part: total charge 2 (phase differences along the ring are larger than $\pi/2$).

the intensities and the propagation constants of the lobes. Since the sign of that slope is *different* for focusing media, the stability behavior is exactly the opposite in this case. Therefore *focusing* vortex clusters are expected to be stable if all phase differences between adjacent lobes are *larger* than $\pi/2$.

In Figure 5.8 these results are verified for a ring-shaped vortex cluster, which consists of 6 lobes being arranged in a hexagon. In all cases the lattice geometry (stretched honeycomb lattice with $k'_x/k'_y = 2.5$) is the same; the intensity flow is initially balanced. The total charge of the cluster is given by the sum of the phase differences along the ring. If these are larger then $\pi/2$, the total charge is 2 (bottom row in Figure 5.8); if they lie between 0 and $\pi/2$, the total charge is 1 (top row).

In the case of a focusing nonlinearity, the single-charged cluster (a) is indeed unstable. The unstable distribution of the intensity flows causes strong intensity

modulations of the lobes. For the parameters chosen in this example, the profile of the cluster is destroyed even completely; this latter fact may be prevented for stronger lattices however.

By contrast, the doubly-charged cluster (b) is stable. Though this fully agrees with the above considerations, it is still a remarkable phenomenon that raising the topological charge may increase the stability. This has no counterpart in homogeneous media, where the growth rate of the modulational instability of ring vortices increases with the vorticity [62]. The stability of focusing higher-order vortices has already been demonstrated in combination with square lattices [63], both for the Gross-Pitaevskii equation and for optically induced lattices in photorefractive media (in the latter case, the isotropic model (2.24) was used). Again, the constraint $\phi_i - \phi_j > \pi/2$ was met for adjacent lobes i, j.

For a defocusing nonlinearity, things are indeed vice versa: Now the single-charged cluster (c) is stable, whereas the doubly-charged one (d) is unstable. In contrast to (a), the hexagonal structure of the cluster is not destroyed in the latter case. The vortex dynamics in (d) is more complicated than that of the unstable 3-lobe cluster considered in the previous section. Over large distances the total charge is zero, though one or more vortex pairs may occur inside the structure (one pair is also visible in Figure 5.8 (d) in the middle of the cluster [$z = 50z_0$ and $z = 100z_0$]). However, the total charge may temporarily take on other values than zero, when vortices enter or leave the structure (not shown here).

6 Stability of symmetric gap vortices

In the previous chapter we have seen that in order to be dynamically stable, vortex clusters have to fulfill a simple phase condition [equation (5.4)]. This can be achieved very easily for symmetric 4-lobe clusters, if the lobes are arranged in a rhombus whose diagonals are parallel to the coordinate axes (see Figure 6.1 (a) for example). In this case, all phase differences between adjacent lobes can be set equal to $\pi/2$, thus forming a vortex with the charge 1. Such a configuration is also known as *offsite vortex*, since the singularity lies between the lattice sites. The offsite vortices discussed in this chapter are fundamental in that sense that they represent the closest pack of lobes, which carries a phase singularity while retaining both the horizontal and the vertical mirror symmetry of the lattice. Additionally, the intensity flow is balanced *independently* of the ratio k'_x/k'_y for many lattice types.

Due to their high symmetry, the offsite vortices with 4 lobes represent a marginal case in view of the qualitative stability analysis presented in the sections 5.4 and 5.5. Actually, the intensity flow remains balanced for an *arbitrary* phase difference $\phi_2 - \phi_1$, if $\phi_1 = \phi_3 - \pi$ and $\phi_2 = \phi_4 - \pi$ [59]. Moreover, the condition (5.4) is only a *necessary* stability criterion.

Hence the stability properties of such structures are not fully covered by the arguments given in chapter 5. They rather depend on more complicated nonlinear effects. Within the *isotropic* model, a linear stability analysis has unveiled that symmetric 4-lobe vortices may be stable for intermediate values of β and I_{latt}, whereas they become unstable if one or both of these parameters take very low or high values [64]. Stable, symmetric 4-lobe vortices were also found in the experiment [39, 40].

In the following we investigate the stability properties of symmetric gap vortices in the anisotropic model. In doing so, we concentrate on offsite vortices with 4 lobes in combination with both signs of the nonlinearity. Additionally, we consider focusing vortices in the first gap, which are located on a *single* lattice site (i.e., they do not represent clusters). The results are based on numerical simulations in all cases [65], since the anisotropic model (2.10) is not well-suited for a linear stability analysis (due to the nonlocality, the expression $\partial E_{nl}(I)/\partial I$ is not well-defined).

6.1 Focusing media

6.1.1 Semi-infinite gap

Except for the square lattice, all lattice types collected in Table 4.1 support focusing, symmetric offsite vortices with 4 lobes and a balanced intensity flow. Figure

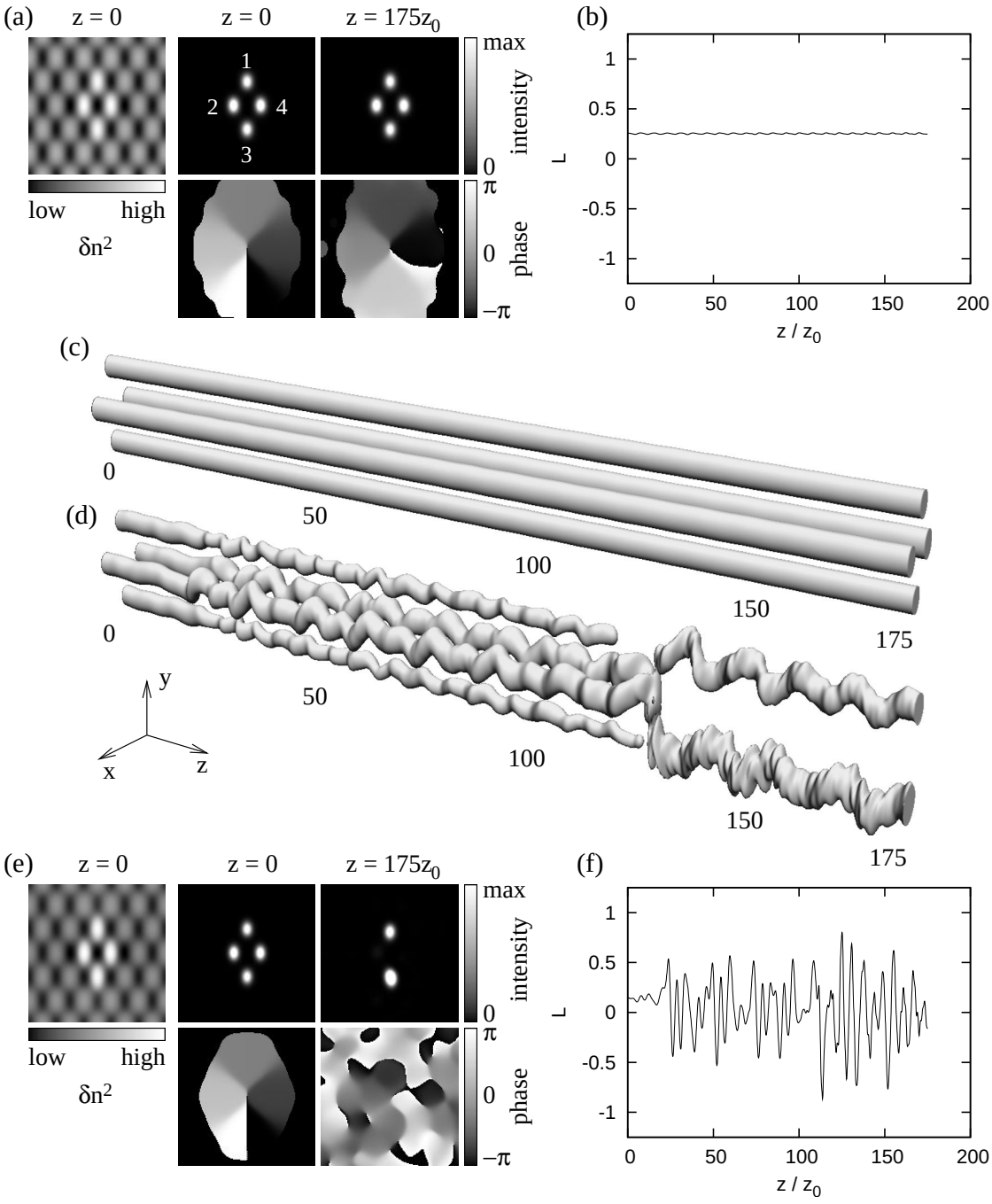

Figure 6.1: Symmetric 4-lobe vortex clusters in the unstretched horizontal honeycomb lattice (focusing nonlinearity, $E_{ext} = 1.5\,\mathrm{kV/cm}$, $I_{latt} = 1$). (a) initial refractive index (δn^2, including the probe beam), intensity and phase profiles before ($z = 0$) and after ($z = 175 z_0$) the propagation, (b) angular momentum, and (c) isointensity surface for $\beta = 1.5$ (z is measured in units of z_0). (d), (e), and (f): same as (c), (a), and (b) for $\beta = 3$.

6.1 exemplifies this for the unstretched honeycomb lattice with $d_x = 30\mu$m and $k'_x/k'_y = \sqrt{3}$. Even if the lattice strength is relatively weak ($I_{latt} = 1$, $E_{ext} = 1.5\,\mathrm{kV/cm}$), the vortices are found to be stable for $\beta_{min} = 1 \lesssim \beta \lesssim 2.5 = \beta_{max}$ [Figure 6.1 (a)-(c); the semi-infinite gap begins at $\beta \approx 0.62$]. For lower or higher values of β (i.e., for very low or high total intensities) the symmetric 4-lobe vortices become unstable, as shown in Figure 6.1 (d)-(f) for $\beta = 3$. This is fully consistent with the results obtained for square lattices within the *isotropic* model [64], which also predict both a lower and an upper threshold intensity for the occurence of stable vortices.

The existence of the upper threshold β_{max} can be understood easily: For high intensities of the vortex, the influence of the lattice is too low to suppress the typical modulational instabilities occuring also in homogeneous media. In our case, another effect arises from the anisotropy however: If the lattice is very weak in relation to the vortex, the system resembles a homogeneous medium, which does not support anisotropic vortices at all. Hence there is an additional threshold $\beta^{(2)}_{max} > \beta_{max}$, above which symmetric gap vortices do not exist at all, i.e., the soliton condition (2.32) cannot be fulfilled. For the parameters in Figure 6.1, $\beta^{(2)}_{max} \approx 5$. This is no issue in isotropic media however, where the symmetric 4-lobe vortices approach ring vortices at high values of β [64].

Already at $\beta = 3$, the instability is strong enough to influence the intensity profile as well [Figure 6.1 (d)-(f)]: At $z \approx 20z_0$, all lobes start to show strong oscillations. Subsequently the charge of the vortex flips several times, but not in a periodic way. At $z \approx 100z_0$ the phase singularity finally disappears, shortly thereafter ($z \approx 111z_0$) the lobes 2 and 4 melt with the lobes 1 and 3. This is a clear effect of the relatively weak lattice. The new state with only two lobes is stable, though the oscillations do not die down. The number of the lobes in the final state depends on the parameters. Especially for higher values of β also decays into more than two lobes occur. Since the trapping effect of the lattice is very low in this regime, these may start to move around in the transverse plane.

Similar effects are also observed for the other lattice types from Table 4.1, such as the horizontal triangular lattice or the vortex lattice. In general, the symmetric 4-lobe vortices can be stabilized by increasing the nonlinear effects (i.e., by raising E_{ext}). This is especially efficient for lattices with a hexagonal symmetry of the underlying lattice wave (i.e., $k'_x/k'_y = \sqrt{3}$). In this case, the values $E_{ext} = 2.5\,\mathrm{kV/cm}$ and $I_{latt} = 4$ are sufficient to obtain large stable regions, both for the horizonal honeycomb lattice and for the two other lattice types mentioned above.

By contrast, a square lattice geometry (i.e., $k'_x/k'_y = 1$) leads to a significant destabilization of the symmetric 4-lobe vortices for all lattices (both the existence and the stability thresholds are lowered drastically). In the vortex lattice, the external electrical field even has to be raised to $E_{ext} = 4\,\mathrm{kV/cm}$ in order to reach stable regimes. In the horizontal honeycomb lattice, stable symmetric 4-lobe vortices can still be observed for $E_{ext} = 2.5\,\mathrm{kV/cm}$; nevertheless the stable region is

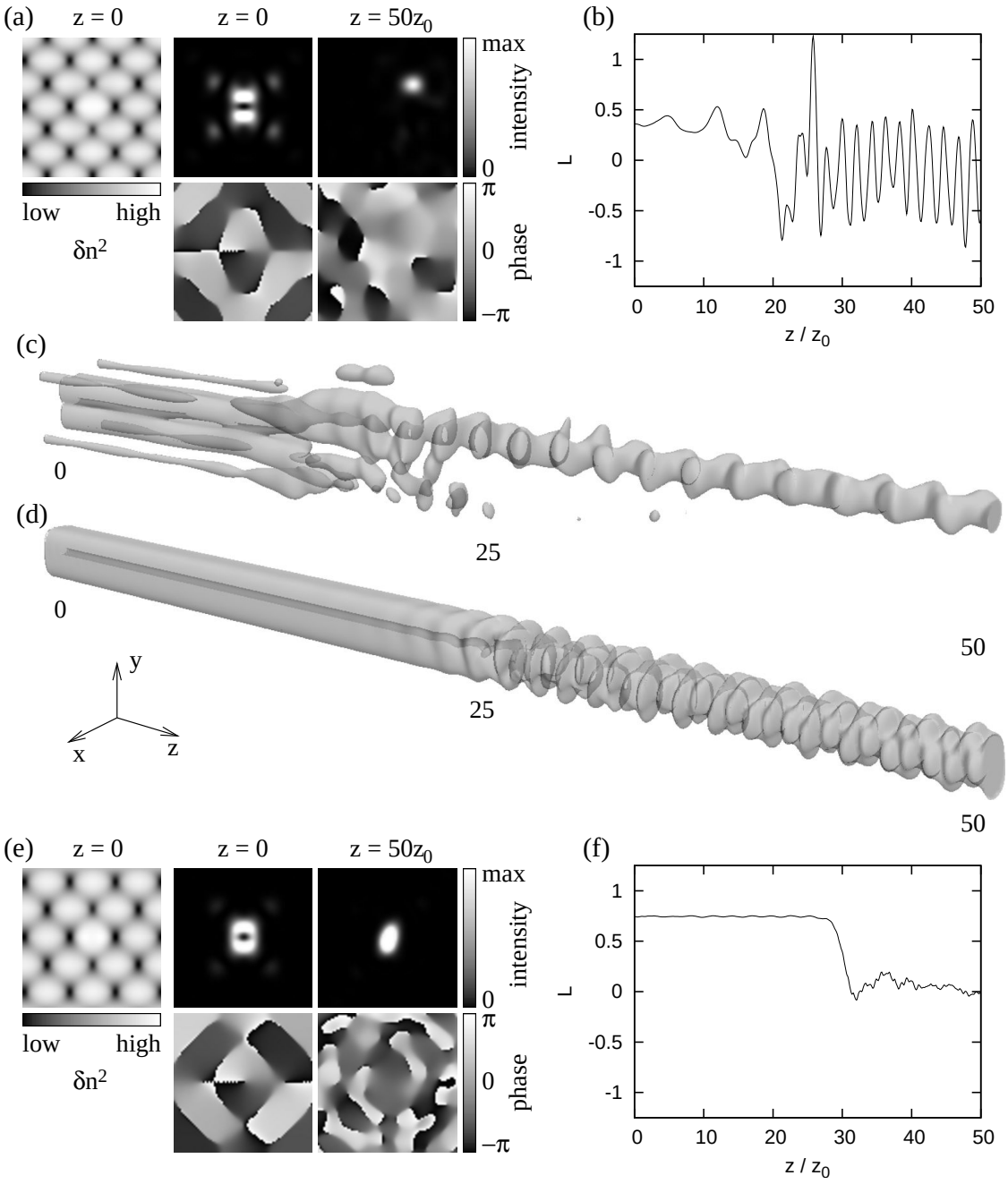

Figure 6.2: Ring-shaped vortices in the first gap of a (stretched) vortex lattice (focusing nonlinearity, $E_{ext} = 2.5\,\mathrm{kV/cm}$, $I_{latt} = 10$). (a) initial refractive index (δn^2, including the probe beam), intensity and phase profiles before ($z = 0$) and after ($z = 50z_0$) the propagation, (b) angular momentum, and (c) transparent isointensity surface for $\beta = -1.0$ and $k'_x/k'_y = 1$ (z is measured in units of z_0). (d), (e), and (f): same as (c), (a), and (b) for $\beta = 0$ and $k'_x/k'_y = 1.2$. See Figure 6.3 for the band structure diagrams.

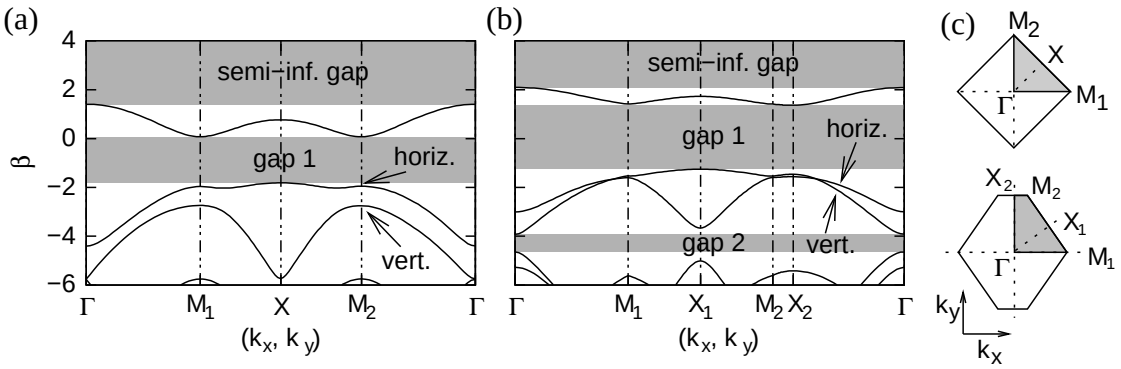

Figure 6.3: Band structure diagrams for the lattices from Figure 6.2 ($E_{ext} = 2.5\,\mathrm{kV/cm}$, $I_{latt} = 10$). (a) regular vortex lattice ($d_x = d_y = 2.5$); (b) stretched vortex lattice ($d_x = 2.5$, $d_y = 3$); (c) first Brillouin zones: regular lattice (top), stretched lattice (bottom).

much smaller also in this case. In this sense, focusing 4-lobe vortices are slightly better supported by the honeycomb lattice.

6.1.2 First gap

Vortex clusters are not the only way of realizing phase singularities in photonic lattices. As we have already seen in section 4.2.1 (Figure 4.4), gap vortices may also appear in the form of intensity profiles, which are localized at a *single* lattice site. These are closely related to vortices in homogeneous media. Like those, they are obtained by superimposing a horizontally and a vertically antisymmetric (Bloch) mode, both being $\pi/2$ out of phase. In contrast to the vortex clusters, the resulting phase profile is continuous; it always features a phase jump of π when crossing the vortex center along an arbitrary straight line. The intensity profile is ring-shaped, since the intensity approaches zero in the vicinity of the singularity.

The underlying Bloch modes arise from the second Bloch band, hence such vortices propagate in the first gap in the case of a focusing nonlinearity. One of their most striking properties is that they exist in *anisotropic* media as well. This is a remarkable difference to ring vortices in homogeneous media.

Although the vortex shown in Figure 4.4 arises only transiently from a dipole-like soliton, ring-shaped gap vortices form an own class of gap solitons. One example in a square-symmetric (i.e., $k'_x = k'_y$) vortex lattice is shown in the Figures 6.2 (a)-(c). Due to the anisotropy, the intensity is not constant along the vortex ring: The vertically antisymmetric Bloch mode is much more pronounced, since the corresponding propagation constants are lower in the linear band-gap spectrum [Figure 6.3 (a)]. Consequently, a higher intensity is needed in order to obtain equal

nonlinear propagation constants for all constituting Bloch modes [65].

Beside the ring, also four minor intensity maxima are visible at the adjacent lattice sites. These are the first maxima of four rapidly decaying, oscillating tails, which are the key signature of gap solitons in the vicinity of a band edge (as we have seen in Figure 3.1, these tails may become far-reaching if the gap is narrow).

As it can be seen, the vortex shown in the Figures 6.2 (a)-(c) is highly unstable. This is not surprising however, since the $B_1^{(foc)}$ solitons are unstable as well in a similar parameter regime (see chapter 4.2.1). At $z \approx 16z_0$, the structure breaks up into several spots, which are drifting away from the original lattice site due to the initial angular momentum. Subsequently most of the intensity is diffracted, whereas the remaining part finally merges in a single, oscillating spot resembling a $B_0^{(foc)}$ soliton. The initial phase singularity has been lost; nevertheless strong oscillations are also visible in the plot of L, since the final spot does not sit on the center (original) lattice site. Akin to the decays of the $B_1^{(foc)}$ solitons, the propagation constant is shifted into the semi-infinite gap.

The strong anisotropic shape of the gap vortex discussed above can be balanced by stretching the lattice along the y axis (i.e., by decreasing k_y'). To this end, one can try to equalize the propagation constants of the horizontally and the vertically antisymmetric Bloch modes [Figure 6.3 (b)]. In doing so the vicinity of the X_2 point is relevant, since the ring-shaped gap vortices originate from there (if $k_x'/k_y' = 1$, the M_2 and the X_2 point coincide).

However, the linear band gap spectrum is only a hint, since the superposition principle does not hold in the nonlinear regime. Additionally, the relevant Bloch modes are distributed over a relatively large region, whereas the propagation constants can be made equal only along an one-dimensional line in the two-dimensional Bloch space. Hence the anisotropy is always visible in the intensity profile of the resulting vortex.

This can be seen clearly in Figure 6.2 (e) ($k_x'/k_y' = 1.2$), although the ring is already more homogeneous in this case than for $k_x'/k_y' = 1$. The instability is weaker in the stretched lattice, nevertheless the vortex decays again into an oscillating $B_0^{(foc)}$ soliton ($z \approx 27z_0$). However, this soliton is located on the original lattice site; there is also much less intensity diffracted than in the non-stretched lattice.

The initial angular momentum is much higher; it can be made nearly equal to 1 if the ratio k_x'/k_y' is further increased. In this case, the *horizontally* antisymmetric Bloch modes dominate the intensity profile. However, this does not significantly increase the stability.

Nevertheless, there are special cases in which anisotropic gap vortices may become stable indeed. One example can be found in the diamond lattice by starting from the parameters used in Figure 4.4 and looking for a solitary gap vortex by solving equation (2.32) (Figure 6.4).

The obtained structure has several striking features, even apart from its stabil-

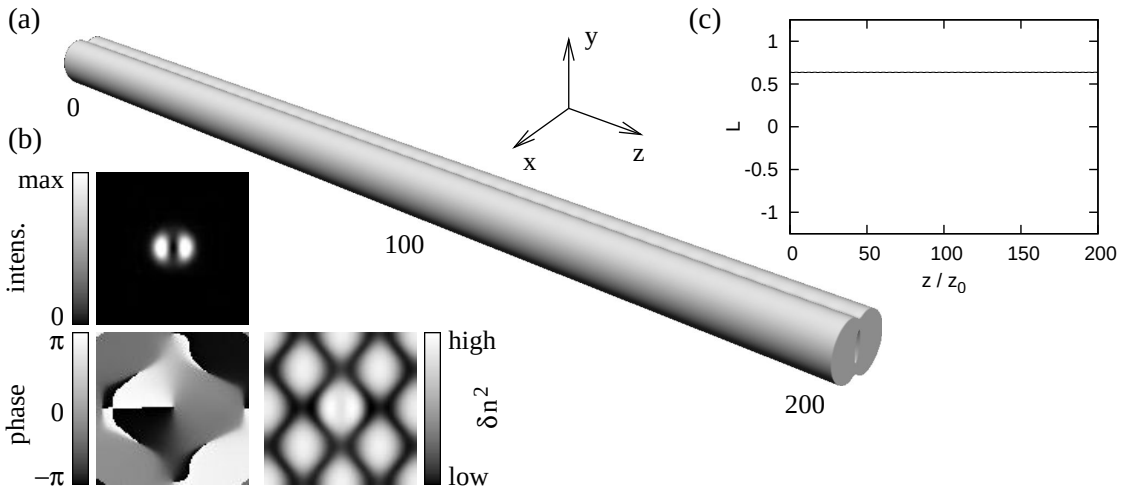

Figure 6.4: Stable anisotropic gap vortex in the diamond lattice (focusing nonlinearity, first gap, $E_{ext} = 4\,\mathrm{kV/cm}$, $I_{latt} = 5$, $\beta = 2.1$). (a) isointensity surface (z is measured in units of z_0); (b) intensity, phase and induced refractive index change (δn^2, including the soliton); (c) angular momentum. See also Figure 4.4.

ity: The contribution of the vertically antisymmetric Bloch modes is very weak, so the structure almost looks like a horizontal dipole. However, the total angular momentum is rather high; additionally the phase profile clearly shows the vortex. Moreover, the area of attraction is relatively large. This has already been demonstrated in Figure 4.4: Neither the horizontal nor the vertical $B_1^{(foc)}$ soliton alone is stable. In the case of the horizontal one a weak, vertically antisymmetric eigenmode (periodically) becomes excited in the course of the propagation, whereas the vertical one decays into a fundamental $B_0^{(foc)}$ soliton. Thus this system represents a rare example of a vortex which arises *autonomously*.

6.2 Defocusing media

Symmetric 4-lobe vortices can also be realized in combination with defocusing nonlinearities [65]. The concept is similar to their focusing pendants, i.e., also the defocusing vortices represent marginally stable solutions in the sense of the chapters 5.4 and 5.5. Their propagation constants lie in the first gap however, hence their stability properties are additionally influenced by finite-gap effects.

In the following, we again concentrate on offsite vortices. In principle, these are supported by all lattices which possess a sufficiently large first gap. For example, this is the case for the diamond, the vortex, and the horizontal honeycomb lattices, but *not* for the horizontal triangular lattice (cf. section 4.1.2). Also the square

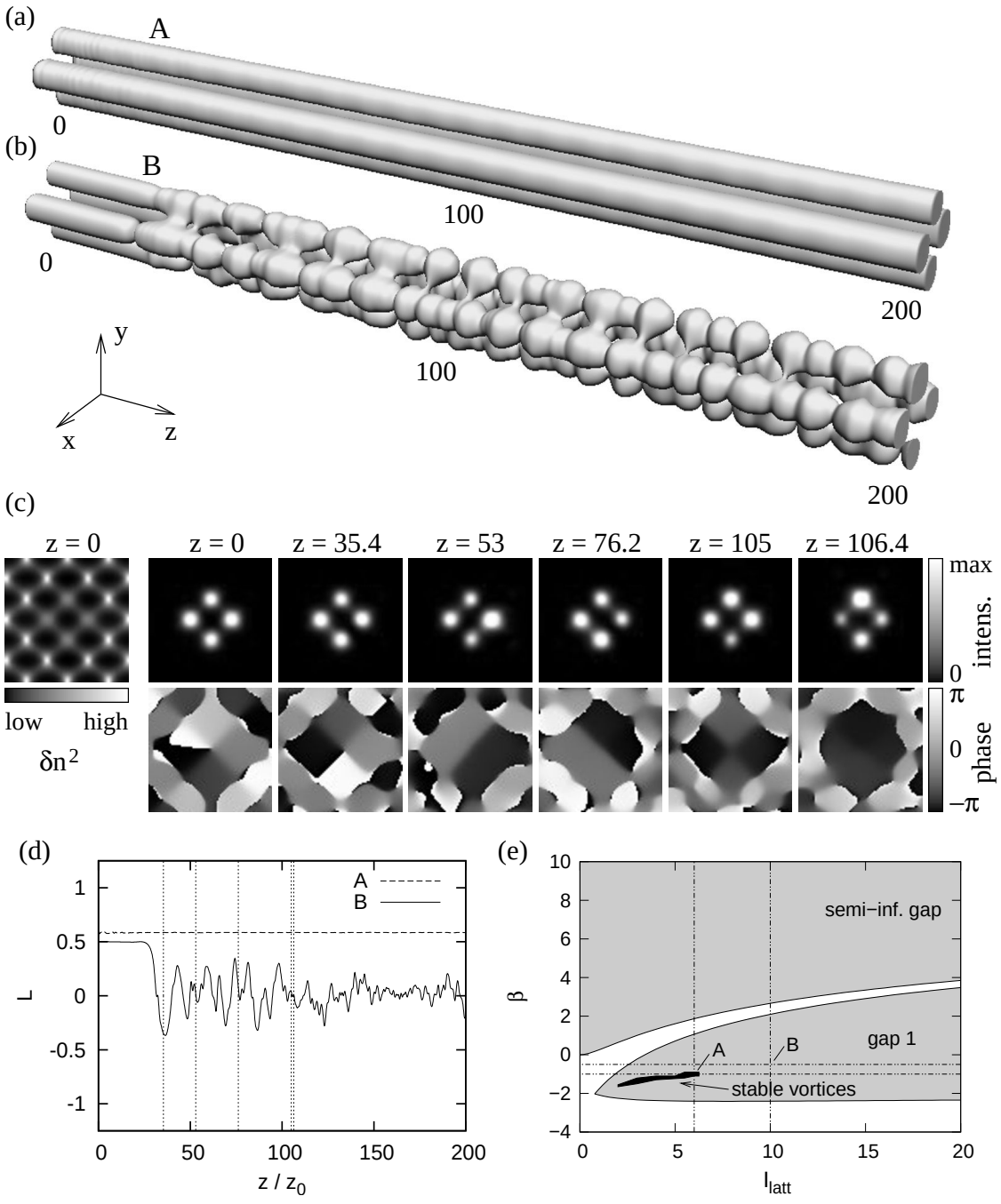

Figure 6.5: Symmetric 4-lobe vortex cluster in the nonstretched vortex lattice (defocusing nonlinearity, $E_{ext} = 2.5\,\mathrm{kV/cm}$). (a), (b) isointensity surface for $I_{latt} = 6.25$, $\beta = -1.0$ (A, stable) and $I_{latt} = 10$, $\beta = -0.5$ (B, unstable); (c) initial refractive index (δn^2, including the probe beam), intensity and phase profiles of B for several propagation distances; (d) angular momentum [vertial lines mark the positions of the pictures in (c)]; (e) region of stable 4-lobe clusters. z is measured in units of z_0.

lattice is not well-suited due to the same reasons as in the focusing case.

Figure 6.5 (c) shows a symmetric 4-lobe vortex ($E_{ext} = 2.5\,\mathrm{kV/cm}$, $I_{latt} = 10$, $\beta = -0.5$) in a defocusing vortex lattice with $k'_x/k'_y = 1$. As it can be seen from the isointensity surface (b) and the angular momentum plot (d), the vortex is unstable for these parameters. The intensity profile with the four lobes is maintained however, though the intensity transfer between them is rather high. Therefore single lobes repeatedly vanish for short distances [Figure 6.5 (b)].

The more interesting dynamics takes place in the phase profile however [Figure 6.5 (c)]: After the first instability has set in ($z \approx 27z_0$), the charge of the initial vortex soon becomes inverted ($z = 35.4z_0$) via an intermediate state with a homogeneous phase ($z \approx 32z_0$, not shown here). Subsequently, the vortex finally disappears after a sequence of some further, less pronounced charge flips. The beam then undergoes several dynamic transitions between the states shown in the rightmost four pictures in Figure 6.5 (c): Either all lobes are in phase, or pairs of adjacent or opposed lobes have the same phase, while the phase difference *between* these pairs is equal to π. All of these in-phase or pairwise out-of-phase states also exist as independent, solitary solutions (quadrupole solitons). However, only the in-phase quadrupole is stable in general. This is also the dominating state when the propagation is calculated over very large distances ($z \gg 200z_0$), although the remaining phase fluctuations die out very slowly.

Depending on the initial values of I_{latt} and β, not all of the states shown in Figure 6.5 (c) do occur. Especially the initial charge flip(s) may be missing. In this case, the vortex is lost from the very beginning, and the transitions between the different quadrupole states immediately follow. There are also many cases, in which not all kinds of the out-of-phase quadrupoles occur. Particularly, the transitions between the modes, where adjacent ($z = 53z_0$, $z = 76.2z_0$) or opposed ($z = 105z_0$) lobes are in phase, are rare.

Within a small region, the symmetric 4-lobe vortices are stable [black area in Figure 6.5 (e)]. This region is bounded due to several reasons: On the one hand, both a lower and an upper stability threshold for the total intensity (or the propagation constant) also exist in the defocusing case. On the other hand, the stability is limited due to finite-gap effects: The chance that an internal mode of the initial vortex causes a resonance in a Bloch band and hence becomes unstable, is higher if the gap is small (cf. chapter 3).

Again, the ratio k'_x/k'_y strongly affects the stability of the vortices (Figure 6.6). If the lattice is stretched along the y axis (i.e., $k'_x/k'_y > 1$), the stable region disappears even though the first gap becomes larger [Figure 6.6 (a),(b)]. By contrast, the stable region can be enlarged significantly by stretching the lattice along the x axis [i.e., $k'_x/k'_y < 1$, Figure 6.6 (c),(d)]. This is just contrary to the focusing case.

The total intensity of the vortices is much higher if $k'_x/k'_y < 1$. Hence the requirement of a certain minimal intensity obviously overrides the finite-gap effects when stable vortices are sought. This is corroborated by the fact that both the

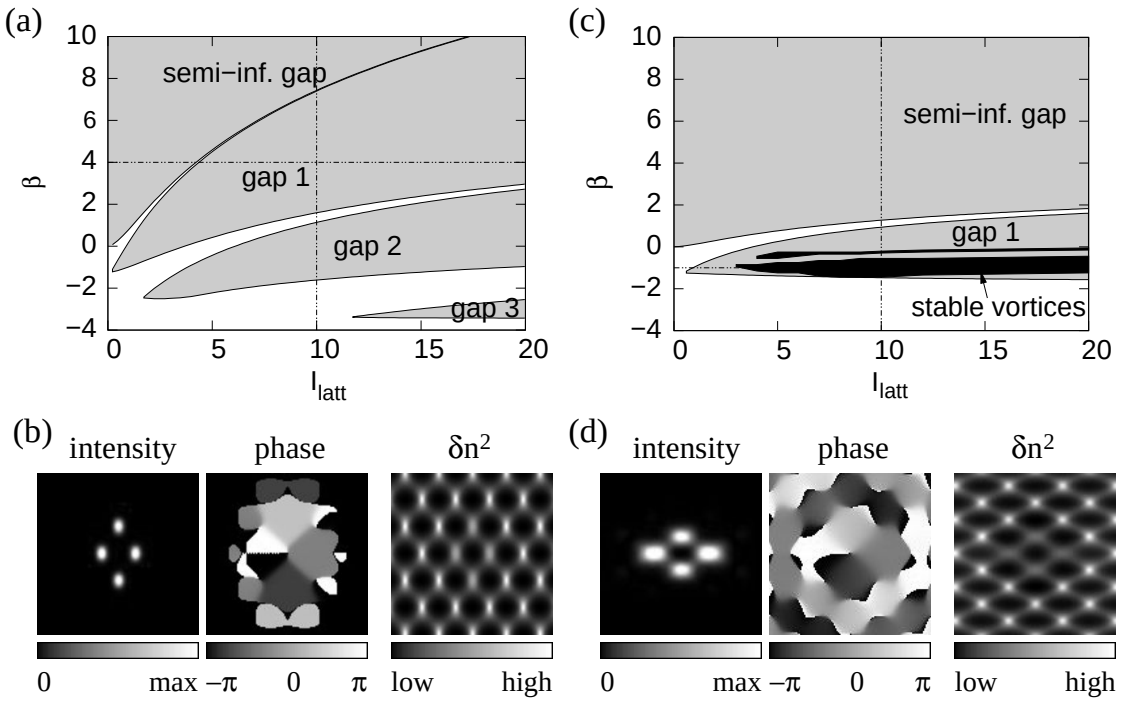

Figure 6.6: Symmetric 4-lobe vortex cluster in the stretched vortex lattices (defocusing nonlinearity, $E_{ext} = 2.5\,\mathrm{kV/cm}$). Left part: $k'_x/k'_y = 1.6$; (a) band-structure, (b) intensity, phase, and initial refractive index (δn^2, including the probe beam), of an unstable gap vortex with $\beta = 4$ and $I_{latt} = 10$. Right part: $k'_x/k'_y = 0.625$; (c) band structure and regions of stable vortices, (d) same as (b) for a stable vortex with $\beta = -1$ and $I_{latt} = 10$.

stable regimes and the total intensities becomes smaller, if E_{ext} is increased. This holds rather independently of the ratio k'_x/k'_y. Consequently, the stable regions may be enlarged by *decreasing* E_{ext}, which is another difference to the focusing case. Of course, E_{ext} must remain high enough in order to stay in the nonlinear regime.

Nevertheless, the finite-gap effects are still clearly visible in Figure 6.6 (c): The stable region consists of *two* parts, being separated by a small, "unstable stripe". This is a typical signature of a resonance occuring in an adjacent Bloch band. Similar phenomena are also visible in the second band in Figure 3.5 (b).

Additionally, the stable vortices are characterized by a relatively large angular momentum. Thus in many cases, it seems to be possible to translate the minimal intensity (lower stability threshold) into a minimal angular momentum, although the relation between these two quantities is complicated in general. A detailed discussion of this question has to be left to future investigations however. The upper intensity threshold for stable vortices cannot be translated this way.

The phenomena discussed in this section are not restricted to the vortex lattice. Comparable results are also obtained for the horizontal honeycomb lattice, though the support (i.e., the size of the stable regions) of *defocusing* symmetric gap vortices is slightly better in the vortex lattice. Again, this is contrary to the focusing case.

7 Summary and outlook

In modern optics, periodically modulated structures are omnipresent. Commonly known as *photonic crystals*, they constitute the optical analog of crystal structures in solid state physics. However, in contrast to the latter they may be homogeneous in one ("2D lattices") or even two ("1D lattices") spatial dimensions. The periodicity results in a band structure similar to solid states, so that linear light propagation becomes impossible if the corresponding wave vectors lie within certain, "forbidden" intervals (photonic band gaps).

Photonic crystals may either be prefabricated (i.e., the refractive index structure is static) or optically induced. The latter can be realized in a rather flexible and reversible way in *photorefractive media*. To this end, an *ordinarily* polarized lattice beam is used. Although this beam itself propagates in a *linear* regime, it induces *nonlinear* changes to the refractive index seen by an *extraordinarily* polarized probe beam. If the lattice beam features a diffraction-compensated, periodic amplitude profile, a two-dimensional photonic lattice is obtained which is homogeneous in the propagation direction.

Since the probe beam *does* experience nonlinear self-interaction, it can be used to excite transversally localized structures within this lattice. These structures always propagate within a (linear) photonic band gap; hence they are called *gap solitons*. In contrast to solitons in homogeneous media, gap solitons occur both for focusing and for defocusing nonlinearities.

The stability properties of gap solitons are the key issue of this thesis, both within statically imprinted photonic lattices and within optically induced ones. Special interest in this topic arises from a close analogy to Bose-Einstein condensates (BEC) in periodic, optical potentials (traps). Both systems can be described by a (generalized) nonlinear Schrödinger equation. Although the pronounced anisotropy of the photorefractive nonlinearity has no exact counterpart in the context of BEC, fundamental results can still be transferred between both systems.

The simplest gap solitons are those with the lowest total intensity. Within this thesis they are called *basic solitons*. The basic solitons in the *lowest accessible* band gap, i.e., the semi-infinite one for focusing and the first one for defocusig media, are of particular interest. Since they can be associated with nonlinear ground states in the quantum mechanical picture, they are called *fundamental* (gap) solitons. In chapter 3, it is shown for statically imprinted photonic lattices that only these fundamental solitons are dynamically stable within a large parameter regime. By contrast, the basic solitons in the other, higher-order band gaps represent excited states, which become stable only for relatively strong photonic lattices. If they are unstable, they stepwise decay into the basic solitons of the lower-order gaps.

Usually this decay ends with a stable, fundamental soliton if no other stable basic solitons exist.

Chapter 4 compares several lattice types which are suitable for the optical induction technique (diffraction-free propagation). It is shown that in this case the influence of the photorefractive anisotropy is much larger than for statically imprinted lattices. This influence can be minimized for square-symmetric lattices, if the edges of the elementary cell are rotated about 45° compared to the coordinate axes. Nevertheless, the anisotropic effects are still significant when comparing the stability of horizontally and vertically oriented basic solitons.

For other lattice types, such as the so-called *triangular lattices*, the anisotropy even becomes the dominating effect. This is in full agreement with the experiment.

Whereas in homogeneous photorefractive media this anisotropy prevents the existence of solitons carrying a topological charge (so-called *vortex solitons*), it is shown in the chapters 5 and 6 that this is not the case in the context of photonic lattices. Such *gap vortices* may be realized on single lattice sites as well as in the form of soliton clusters. It is demonstrated that both kinds can be dynamically stable. Moreover, the single-site vortices may even be attractors for simpler, but unstable gap solitons which *do not* carry a topological charge.

In order to obtain stable vortex *clusters*, a special phase condition has to be fulfilled however. Otherwise the internal intensity flow is no longer balanced, which may lead to a periodically flipping of the vortex charge. This also holds for clusters containing multiple vortices, where rather complicated mechanisms may finally lead to periodic charge flips of each single vortex.

Moreover, for a special type of multivortex cluster consisting of seven lobes and containing six vortices, it can be shown that the phase condition cannot be fulfilled if the underlying lattice has an exactly hexagonal symmetry. This is a direct consequence of the anisotropic nonlinearity. Corresponding numerical simulations, indicating that such clusters may become stable only if the lattice is slightly stretched, are confirmed by experiments.

Based on the phase condition, a qualitative stability analysis reveals in connection with a focusing nonlinearity that ring-shaped vortex clusters with six lobes, which contain *two identical* phase singularities, may be stable whereas their single-charged counterparts are unstable. This behavior depends on the phase differences between the single lobes; it is reversed for defocusing nonlinearities. These are striking results, since in homogeneous media higher topological charges usually lead to stronger instabilities.

By contrast, the stability behavior of highly symmetric gap vortices with a phase difference of $\pi/2$ between adjacent lobes is very complex. Although it is shown in chapter 6 that these are stable typically for intermediate lattice strengths and intensities of the probe beams, an in-depth discussion of this topic would require a complete linear stability analysis. However, this is an unsolved problem up to now since there is no closed expression for the anisotropic photorefractive nonlinearity

yet. Due to the additionally nonlocal properties of this nonlinearity, such an analysis would involve methods being far beyond the scope of this thesis. Therefore this point has to be left open for future investigations. However, such an analysis certainly would provide deep insights not only into the dynamics of anisotropic gap vortices, but also into the properties of nonlocal media in general.

Another open question is, whether it is possible to establish a general link between the total angular momentum and the lower stability threshold (related to the intensity) of gap vortices. Although the results presented in chapter 6 suggest that also a certain *minimal angular momentum* is needed in order to obtain stable vortices, there is no systematic investigation of this question yet.

Zusammenfassung

In der modernen Optik sind periodische Strukturen, häufiger auch als *photonische Kristalle* bezeichnet, allgegenwärtig. Sie stellen das optische Gegenstück zu den Kristallgittern in Festkörpern dar. Im Gegensatz zu diesen können sie jedoch entlang einer oder sogar zweier Raumrichtungen homogen sein. In diesem Fall spricht man von 2D- bzw. 1D-Gittern. Ähnlich wie Festkörper besitzen photonische Kristalle eine Bandstruktur: Liegt der Wellenvektor einer Lichtverteilung innerhalb bestimmter, „verbotener“ Intervalle (sogenannter photonischer Bandlücken), so ist keine lineare Lichtausbreitung möglich.

Photonische Kristalle können entweder vorgefertigt sein (die entsprechende Struktur des Brechungsindexes ist dann statisch) oder optisch induziert werden. Letzteres ist recht einfach und reversibel in *photorefraktiven Medien* möglich. Zu diesem Zweck wird ein *ordentlich* polarisierter „Gitterstrahl“ verwendet. Obwohl dieser selbst *linear* propagiert, induziert er eine *nichtlineare* Änderung des Brechungsindexes, der für einen *außerordentlich* polarisierten „Teststrahl“ gilt. Besitzt der Gitterstrahl ein beugungskompensiertes, periodisches Amplitudenprofil, so erhält man ein zweidimensionales photonisches Gitter, welches entlang der Propagationsrichtung homogen ist.

Da der Teststrahl nichtlinearer Selbstwechselwirkung ausgesetzt ist, kann er dazu verwendet werden, transversal lokalisierte Strukturen innerhalb des Gitters anzuregen. Diese Strukturen propagieren grundsätzlich innerhalb einer (linearen) photonischen Bandlücke, weshalb sie auch als *Gap-Solitonen* (von engl. gap = Lücke) bezeichnet werden. Im Gegensatz zu Solitonen im homogenen Medien treten Gap-Solitonen sowohl im Zusammenhang mit fokussierenden, als auch mit defokussierenden Nichtlinearitäten auf.

Die Stabilitätseigenschaften von Gap-Solitonen, sowohl im Zusammenhang mit statisch realisierten, als auch mit optisch induzierten photonischen Gittern, sind das zentrale Thema der vorliegenden Arbeit. Dieses Thema ist von besonderem Interesse aufgrund einer engen Analogie zu Bose-Einstein-Kondensaten (BEC) in periodischen optischen Potentialen (Fallen). Beide Systeme können durch eine (verallgemeinerte) nichtlineare Schrödinger-Gleichung beschrieben werden. Obwohl die ausgeprägte Anisotropie der photorefraktiven Nichtlinearität kein exaktes Gegenstück im Bereich der BEC besitzt, lassen sich grundlegende Ergebnisse zwischen beiden System übertragen.

Die einfachsten Gap-Solitonen sind diejenigen mit der niedrigsten Gesamtenergie. Im Rahmen dieser Arbeit werden sie auch als (engl.) *basic solitons* bezeichnet. Von besonderem Interesse sind dabei diejenigen *basic solitons*, welche in der *niedrigsten erreichbaren* Bandlücke liegen, d.h. in der semi-infiniten für fokussierende und in

der ersten für defokussierende Medien. Diese können in der quantenmechanischen Betrachtungsweise mit nichtlinearen Grundzuständen identifiziert werden, weshalb sie auch als *fundamentale* (Gap-)Solitonen bezeichnet werden. In Kapitel 3 wird für statisch realisierte photonische Gitter gezeigt, daß nur diese fundamentalen Gap-Solitonen innerhalb eines größeren Parameterbereiches dynamisch stabil sind. Die *basic solitons* in den höheren Bandlücken stellen dagegen angeregte Zustände dar, welche nur für relativ starke photonische Gitter stabil werden. Falls diese instabil sind, zerfallen sie schrittweise in die *basic solitons* der niedrigeren Bandlücken. Üblicherweise endet dieser Zerfall mit einem stabilen, fundamentalen Soliton, falls keine anderen stabilen *basic solitons* existieren.

In Kapitel 4 werden einige Gittertypen miteinander verglichen, welche sich für die optische Induktion eignen (beugungsfreie Propagation). Es wird gezeigt, daß in diesem Fall der Einfluß der photorefraktiven Anisotropie deutlich stärker als bei statisch realisierten Gittern ist. Für Gitter mit quadratischer Symmetrie kann dieser Einfluß minimiert werden, indem die Kanten der Elementarzelle um 45° gegenüber den Koordinatenachsen gedreht werden. Dennoch werden die anisotropen Effekte deutlich, was sich unter anderem beim Vergleich der Stabilitätseigenschaften horizontaler und vertikaler *basic solitons* zeigt.

Für andere Gittertypen, wie zum Beispiel den soganneten *Dreiecksgittern*, ist die Anisotropie sogar der dominierende Efekt. Dies ist in vollständiger Übereinstimmung mit dem Experiment.

In homogenen photorefraktiven Medien können sogenannte *Vortex-Solitonen*, das heißt Solitonen, die eine topologische Ladung tragen, aufgrund der Anisotropie nicht existieren. Dies ist jedoch möglich im Zusammenhang mit photonischen Gittern, wie in den Kapiteln 5 und 6 gezeigt wird. Solche (engl.) *gap vortices* können entweder auf einzelnen Gitterplätzen oder in Form von Soliton-Clustern realisiert werden. Es wird gezeigt, daß beide Arten stabil sein können. Darüber hinaus kann die erstere auch einen Attraktor für einfachere, jedoch instabile Gap-Solitonen darstellen. Diese müssen selbst keine topologische Ladung besitzen.

Stabile Vortex-*Cluster* müssen jedoch eine besondere Phasenbedingung erfüllen. Andernfalls ist der interne Intensitätsfluß nicht ausgeglichen, was zu einer periodischen Ladungsumkehr des Vortexes führen kann. Dies gilt auch für Cluster, die mehrere Vortices enthalten. In diesem Fall führen relativ komplizierte Mechanismen dazu, daß sich die Vorzeichen aller Einzelladungen periodisch umkehren.

Für einen speziellen Multivortex-Cluster mit sechs Vortices, welcher aus sieben Einzelsolitonen (engl. *lobes*) besteht, kann gezeigt werden, daß sich die Phasenbedingung nicht erfüllen läßt, falls das zugrundeliegende Gitter eine exakt hexagonale Symmetrie besitzt. Dies ist eine direkte Konsequenz der Anisotropie der Nichtlinearität. Entsprechende numerische Simulationen deuten darauf hin, daß derartige Cluster nur stabil sein können, falls das Gitter leicht gestreckt wird. Dies wird durch Experimente bestätigt.

Aufbauend auf der Phasenbedingung ergibt eine qualitative Stabilitätsanalyse,

daß ringförmige Vortex-Cluster mit sechs „lobes“ im Zusammenhang mit einer fokussierenden Nichtlinearität stabil sein können, falls diese *zwei gleichartige* Phasensingularitäten besitzen. Ihre einfach geladenen Gegenstücke sind hingegen instabil. Dies hängt mit den Phasendifferenzen zwischen den lobes zusammen; für defokussierende Nichtlinearitäten kehren sich die Stabilitätsverhältnisse um. Diese Ergebnisse sind deshalb bemerkenswert, da in homogenen Medien höhere topologische Ladungen üblicherweise zu größeren Instabilitäten führen.

Im Gegensatz dazu besitzen Gap-Vortices mit hoher Symmetrie, die eine Phasendifferenz von $\pi/2$ zwischen benachbarten lobes aufweisen, ein äußerst komplexes Stabilitätsverhalten. Obwohl in Kapitel 6 gezeigt wird, daß diese normalerweise für mittlere Gitterstärken und Intensitäten des Probenstrahls stabil sind, ist für eine tiefergehende Betrachtung eine vollständige lineare Stabilitätsanalyse notwendig. Dies ist jedoch ein bis heute ungelöstes Problem, da noch kein geschlossener Ausdruck für die anisotrope photorefraktive Nichtlinearität gefunden werden konnte. Aufgrund der zusätzlich nichtlokalen Eigenschaften der Nichtlinearität würde eine solche Analyse Methoden erfordern, die den Rahmen dieser Arbeit sprengen würden. Dieser Punkt muß daher zukünftigen Untersuchungen überlassen werden. Diese würden jedoch tiefe Einblicke nicht nur in die Dynamik anisotroper Gap-Vortices, sondern auch generell in die Eigenschaften nichtlokaler Medien ermöglichen.

Eine weitere offene Frage ist diejenige nach einem Zusammenhang zwischen dem Gesamtdrehimpuls und der unteren Stabilitätsschwelle (bezogen auf die Intensität) von Gap-Vortices. Obwohl die in Kapitel 6 vorgestellten Ergebnisse nahelegen, daß auch ein *minimaler Drehimpuls* für stabile Vortices nötig ist, steht eine systematische Untersuchung dieses Punktes noch aus.

A Numerical calculation of gap solitons

In order to determine the (complex) amplitude profile $a(\mathbf{r}_\perp)$ of a gap soliton, one has to solve the Eqn. (2.31) or (2.32), depending on whether the lattice is statically imprinted or optically induced. Although there are several ways how to do this numerically, a special treatment is required since there is no closed expression for the nonlinearity in the case of the anisotropic model (2.23).

Additionally, it should be possible to specify the propagation constant β as a parameter at the outset (β must not lie within a band). This is especially important, if a solitary solution in a particular (finite) band gap is sought. Hence algorithms taking the total intensity $\int |a(\mathbf{r}_\perp)|^2 \mathrm{d}\mathbf{r}_\perp$ as a parameter instead are not appropriate for our purposes.

In the following, we briefly introduce two methods which fulfill these requirements while having proven to be rather fast and reliable in practice.

A.1 Gradient-based methods

Particularly with regard to gap vortices an algorithm is desirable, which is able to calculate *arbitrary* non-fundamental solitons from appropriate initial conditions. Such an algorithm has been presented in [66] for *local* nonlinearities. It is based on minimizing an error functional $F(a)$, which is constructed from the Eqn. (2.31) by taking the integral of the squared absolute value of the left hand side:

$$F[a] \stackrel{\text{def}}{=} \int |Ga(\mathbf{r}_\perp)|^2 \, \mathrm{d}\mathbf{r}_\perp \tag{A.1}$$

with the nonlinear operator

$$G \stackrel{\text{def}}{=} -2\beta + \boldsymbol{\nabla}_\perp^2 + k_0^2 w_0^2 \, \delta n_p^2(\mathbf{r}_\perp) - \gamma_{nl} E_{scr}(|a|^2). \tag{A.2}$$

A similar definition can be formulated for Eqn. (2.32). Obviously $F[a] \geq 0$, where the equality holds if and only if $a(\mathbf{r}_\perp)$ is a solitary solution. Therefore *any* solitary solution with a given propagation constant β can be found as a local minimum of F.

Starting from an appropriate initial condition $a_0(\mathbf{r}_\perp)$, the following descent method may be formulated [66]:

$$a_{n+1} = a_n - s \cdot \nabla_S F[a_n] \equiv a_n - s \cdot (1 - \boldsymbol{\nabla}_\perp^2)^{-1} \nabla F[a_n]. \tag{A.3}$$

Herein $\nabla_S F$ is denoted as *Sobolev gradient*, whereas the "ordinary" gradient ∇F is defined to be the functional derivative $\delta F[a_n]/\delta a_n$. The step width s is a positive

real number which has to be chosen small enough in order to obtain convergence against a solitary solution. Taking the Sobolev gradient instead of the ordinary funtional derivative significantly improves the convergence of the method.

The functional derivative $\delta F[a_n]/\delta a_n$ reads

$$\frac{\delta F[a_n]}{\delta a_n} = G^2 a_n + \left.\frac{\partial E_{scr}(I)}{\partial I}\right|_{I=|a_n|^2} \cdot (a_n^* G a_n + (G a_n)^* a_n) a_n. \tag{A.4}$$

Herein the partial derivative $\partial_I E_{scr}(I)$ is well-defined only if $E_{scr}(I)$ is *local*, i.e., a pointwise mapping $I \mapsto E_{scr}(I)$. This is not the case for the anisotropic model however.

Nevertheless, it turns out in practice that the convergence behavior does not crucially depend on this term. Therefore the derivative may be approximated by the one obtained within the *isotropic* model (2.24), *as long as the anisotropic model (2.23) is used in the definition of* G (so that $F[a] = 0$ still indicates that $a(\mathbf{r}_\perp)$ is an anisotropic soliton). This means,

$$\left.\frac{\partial E_{scr}(I)}{\partial I}\right|_{I=|a_n|^2} = -\frac{\gamma_{nl} E_{ext}}{\left(1+|a_n|^2\right)^2} \tag{A.5}$$

may be used for statically imprinted lattices [Eqn. (2.31)], whereas

$$\left.\frac{\partial E_{scr}(|A_{latt}|^2 + I)}{\partial I}\right|_{I=|a_n|^2} = -\frac{\gamma_{nl} E_{ext}}{\left(1+|A_{latt}|^2+|a_n|^2\right)^2} \tag{A.6}$$

may be used for optically induced ones [of course, Eqn. (A.2) has to be replaced by $G \stackrel{\text{def.}}{=} -2\beta + \boldsymbol{\nabla}_\perp^2 - \gamma_{nl} E_{scr}(|A_{latt}|^2 + |a|^2)$ in this case, cf. Eqn. (2.32)].

This yields a rather fast but still reliable algorithm, which is capable of finding a large variety of anisotropic gap solitons. It has been used to calculate most of the solitary profiles presented within this work. However, there is *no a priori guarantee* that the iteration (A.3) converges against a solitary solution for an (arbitrary) initial profile a_0. The approximations (A.5) and (A.6) slightly enhance the sensitivity to a_0 if a particular solitary solution is sought. Using an adaptive control of the step width s significantly decreases the computation time needed while increasing the robustness of the method.

A.2 Petviashvili methods

The approximations (A.5) and (A.6) raise the question, whether there is a more general algorithm for finding (gap) solitons that can also handle nonlocal nonlinearities without any further approximations. Such an algorithm has originally been proposed for homogeneous systems by Petviashvili in 1976 [67]. It is characterized by a very fast convergence, although it is restricted to fundamental solitons in the

majority of cases. An application of this method to (homogeneous) photorefractive crystals is presented in [68]. With some modifications the algorithm can also be used to calculate gap solitons however, as we will demonstrate in the following.

The Petviashvili method is based on a fixed point iteration of the Fourier transformed soliton conditional equation, i.e., Eqn. (2.31) or (2.32) in our case. Applied to Eqn. (2.31), the iteration scheme reads

$$a_{n+1} = \mathcal{F}^{-1}\left[|M|^{3/2} \cdot \frac{\mathcal{F}\left[k_0^2 w_0^2\, \delta n_p^2(\mathbf{r}_\perp) a_n\right] - \mathcal{F}\left[\gamma_{nl} E_{scr}(|a_n|^2) a_n\right]}{2\beta + \mathbf{k}_\perp^2}\right] \tag{A.7}$$

$$M = \frac{\int \mathrm{d}\mathbf{k}_\perp \left(2\beta + \mathbf{k}_\perp^2\right) \left|\mathcal{F}[a_n]\right|^2}{\int \mathrm{d}\mathbf{k}_\perp \left(-\mathcal{F}\left[k_0^2 w_0^2\, \delta n_p^2(\mathbf{r}_\perp) a_n\right] + \mathcal{F}\left[\gamma_{nl} E_{scr}(|a_n|^2) a_n\right]\right) \left(\mathcal{F}[a_n]\right)^*}, \tag{A.8}$$

where $\mathcal{F}$ and $\mathcal{F}^{-1}$ denote the Fourier transform and its inverse. A similar scheme can be formulated for Eqn. (2.32).

The functional M is necessary in order to obtain convergence. Obviously, M becomes equal to 1 if $a(\mathbf{r}_\perp)$ is solitary. In this case, Eqn. (A.7) is fully equivalent to a Fourier transformed version of Eqn. (2.31).

Without further modifications, this straightforward application of the original algorithm only works within the semi-infinite gap however. The convergence is slower than for homogeneous media, and there are several cases where the iteration does not converge at all. Although several generalizations of the Petviashvili method have been published in the last years, they are either not applicable to the photorefractive nonlinearity (2.23) [69], or the restriction to the semi-infinite gap remains [70].

This can be overcome if the Fourier transform is replaced by another, more appropriate transform [71]: The key idea of Petviashvili was to separate linear and nonlinear terms during the iteration. In the case of statically imprinted lattices [Eqn. (2.31)], the linear terms can be expressed by the operator [cf. Eqn. (A.2)]

$$G_{lin}^{(stat.)} \stackrel{\text{def}}{=} -2\beta + \boldsymbol{\nabla}_\perp^2 + k_0^2 w_0^2\, \delta n_p^2(\mathbf{r}_\perp). \tag{A.9}$$

Since the eigenbasis of this operator is formed by the Bloch functions $\psi_m(\mathbf{r}_\perp, \mathbf{k}_\perp)$ (cf. section 2.3.1), the inverse operator $\left(G_{lin}^{(stat.)}\right)^{-1}$ can be applied easiest in the Bloch space. The link between the ordinary space and the Bloch space is provided by the *Bloch transform*

$$\mathcal{B}_m[f(\mathbf{r}_\perp)] \stackrel{\text{def}}{=} \hat{f}_m(\mathbf{k}_\perp) = \int_{\mathbb{R}^2} f(\mathbf{r}_\perp) \psi_m^*(\mathbf{r}_\perp, \mathbf{k}_\perp) \mathrm{d}\mathbf{r}_\perp, \quad m \in \mathbb{N},\ \mathbf{k}_\perp \in FBZ \tag{A.10}$$

and its inverse [cf. Eqn. (2.33)]

$$\sum_{m=1}^{\infty} \mathcal{B}_m^{-1}[\hat{f}_m(\mathbf{k}_\perp)] \stackrel{\text{def}}{=} f(\mathbf{r}_\perp) = \sum_{m=1}^{\infty} \int_{FBZ} \hat{f}_m(\mathbf{k}_\perp) \psi_m(\mathbf{r}_\perp, \mathbf{k}_\perp) \mathrm{d}\mathbf{k}_\perp. \tag{A.11}$$

Herein m denotes the number of the Bloch band. With this transform the Petviashvili iteration becomes

$$a_{n+1} = \sum_{m=1}^{\infty} \mathcal{B}_m^{-1} \left[|M|^{3/2} \cdot \frac{\mathcal{B}_m \left[-\gamma_{nl} E_{scr}(|a_n|^2) a_n \right]}{\beta_m(\mathbf{k}_\perp)} \right] \tag{A.12}$$

$$M = \frac{\int \mathrm{d}\mathbf{k}_\perp \, \beta_m(\mathbf{k}_\perp) \, \left| \mathcal{B}_m[a_n] \right|^2}{\int \mathrm{d}\mathbf{k}_\perp \mathcal{B}_m \left[\gamma_{nl} E_{scr}(|a_n|^2) a_n \right] \left(\mathcal{B}_m[a_n] \right)^*} \, . \tag{A.13}$$

The $\beta_m(\mathbf{k}_\perp)$ represent the eigenvalues of $G_{lin}^{(stat.)}$ corresponding to the Bloch functions $\psi_m(\mathbf{r}_\perp, \mathbf{k}_\perp)$.

The algorithm (A.12), (A.13) shows good convergence properties also within the finite gaps. Additional control can be exercised by restricting the Bloch basis to those $\psi_m(\mathbf{r}_\perp, \mathbf{k}_\perp)$ whose propagation constants lie within certain bands. This provides an easy method to obtain the basic solitons of the higher-order gaps, since the constraints on the initial condition a_0 are not critical (a roughly approximated intensity profile with a correct phase profile is sufficient in the majority of cases).

One drawback of this algorithm consists in the relatively large numerical expense, since the Bloch transform is much slower than the fast Fourier transform. This expense can be reduced by further restricting the Bloch basis, although this leads to less accurate solutions. However, these are excellent initial conditions for the gadient-based methods discussed in the previous section.

In the case of optically induced lattices, $G_{lin}^{(stat.)}$ has to be replaced by

$$G_{lin}^{(opt.)} \stackrel{\text{def}}{=} -2\beta + \boldsymbol{\nabla}_\perp^2 - \gamma_{nl} E_{ext}(|A_{latt}|^2). \tag{A.14}$$

Consequently, $E_{scr}(|a_n|^2)$ has to be replaced by $E_{scr}(|A_{latt}|^2 + |a_n|^2) - E_{scr}(|A_{latt}|^2)$ in the equations (A.12) and (A.13). This is obtained by adding and subtracting the term $\gamma_{nl} E_{scr}(|A_{latt}|^2)$ on the left hand side of equation (2.32). Otherwise the periodicity would be ignored in the linear part of the iteration scheme, and the Bloch transform would degenerate to a Fourier transform.

B Numerical beam propagation and absorbing boundary conditions

There are several methods to solve the propagation equation (2.11) numerically [72]. The standard one is the so-called *split-step Fourier method* [also known as *beam propagation method (BPM)*], which belongs to the class of *pseudospectral methods*. The basic idea is to split the integration procedure into that steps that would be required, if the right hand side of (2.11) consisted either of the linear or the nonlinear term alone. The linear step can be carried out in the Fourier space; it corresponds to solving a linear Schrödinger equation. The nonlinear step is approximated by an exponential function, thereby assuming that the nonlinearity (δn^2) does not change during the step (therefore the step width has to be small enough).

Due to its explicit nature and the possibility of using FFT routines, this algorithm is very fast (see [72] for a comparison). Nevertheless, it has also been proven to be very reliable.

However, using the discrete Fourier transform implies periodic boundary conditions. Though this does not matter as long as the beam stays localized, it becomes problematically when the decay of gap solitons is studied. As being demonstrated in chapter 3, the corresponding unstable eigenmodes have far-ranging, oscillating tails. Therefore artificial interferences arising from the grid boundaries cannot be efficiently suppressed by simply enlarging the numerical grid.

A simple method to circumvent these problems is to multiply the amplitude distribution by a filter function $f(x, y)$ in each step (filtered BPM). This function must be equal to one in the middle of the grid (usable area), whereas it should continuously approach zero in a transition zone near the boundaries of the grid. This is sufficient to absorb beams whose angles of incidence are not too high (less than 89.5°). Otherwise the transition zone has to be made very large (inefficient), or a significant amount of intensity is reflected.

A more efficient way of implementing truly absorbing boundary conditions is presented in [53]. It is based on rewriting the propagation equation (2.11) as follows:

$$i\partial_z A = -\frac{1}{2}\frac{1}{\nu(x,y)}\boldsymbol{\nabla}_\perp\left(\frac{1}{\nu(x,y)}\boldsymbol{\nabla}_\perp A\right) - \frac{k_0^2 w_0^2}{2}\delta n^2(I)A. \tag{B.1}$$

The original equation (2.11) is recovered for $\nu \equiv 1$, whereas it can be easily shown that the solution of the equation (B.1) is an exponentially damped wave if $\nu \equiv i$ and $\delta n^2 \equiv 0$. Thus an absorbing boundary layer (*Perfecly Matched Layer, PML*) can be constructed by choosing $\nu(x, y)$ to vary in a similar way between 1 and i, as the filter function $f(x, y)$ does between 1 and 0. The function $\nu(x, y)$ does not need

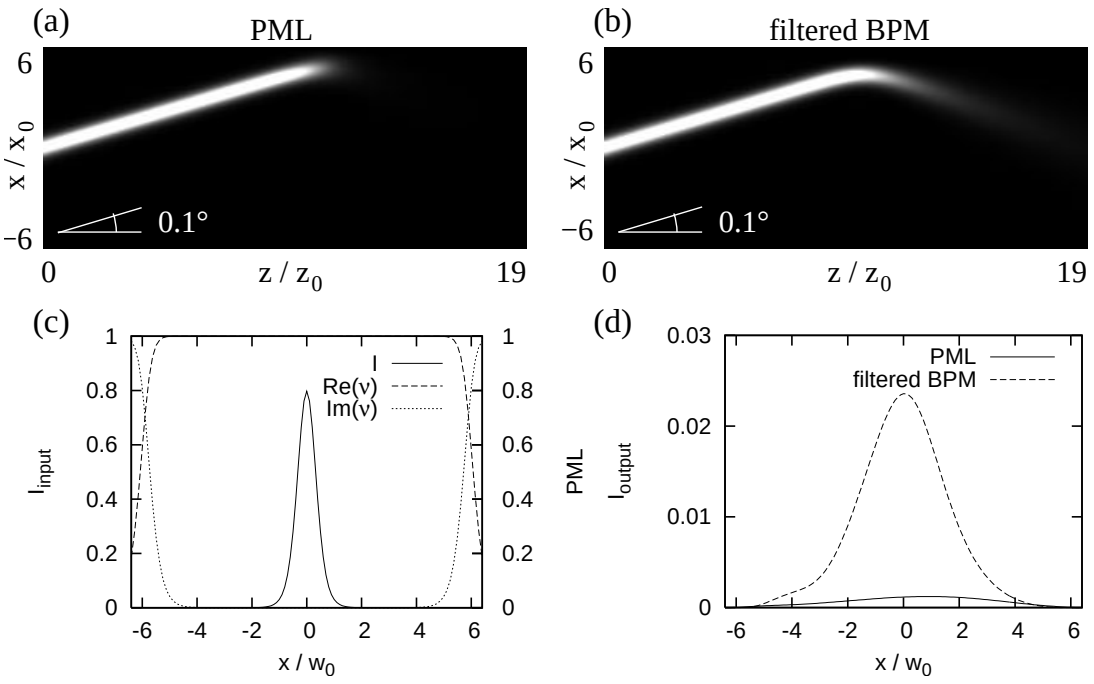

Figure B.1: Comparing PML and filtered BPM. (a), (b) transverse profiles of a tilted beam being absorbed by (a) PML boundary conditions and (b) a simple envelope function; (c) input intensity profile (x transverse section) and PML profiles [Re(θ) is also used as evelope function for the filtered BPM]; (d) output intensity profiles

to be continuously differentiable however (this property is needed for the filtered BPM, since otherwise strong reflections occur at the boundaries).

Though a non-vanishing nonlinear term slightly increases the reflectivity of the PML, very high absorption coefficients can be achieved even for relatively thin transition zones and angles of incidence being very close to 90°.

A comparison between filtered BPM and PML is shown in Figure B.1. For that purpose, $f(x, y) = \mathrm{Re}(\nu(x, y))$ was chosen. To simplify matters, the calculations have been carried out for a homogeneous medium using the isotropic model (2.24). Similar results are obtained for the anisotropic model however. The input beam was a fundamental soliton tilted by 0.1° in x direction, corresponding to an angle of incidence of 89.9°.

Though both integration methods provide a strong damping of the beam at the grid boundary, the peak intensity of the reflected (output) beam is about one order of magnitude larger in case of the the filtered BPM. For larger angles of incidence, this ratio quickly increases (for 89.95°, it is already larger than 2 orders of magnitude). This is mainly due to the poor efficiency of the filtered BPM; the

reflectivity of the PML raises much slower with the angle of incidence.

However, one drawback of the PML is that pseudospectral methods cannot be applied to equation (B.1). For transversally one-dimensional systems it is possible to use pure implicit methods like the Crank-Nicolson scheme instead [53]. However, these turn out to be too time-consuming for two-dimensional systems.

One alternative is given by the *Hopscotch method*, which combines both the advantages of explicit (speed) and of implicit (stability) integration schemes. This is achieved by dividing the transversal grid points (i, j) into *odd* and *even* ones, depending on the sum $(i + j)$. At first an explicit scheme is applied to the even points; subsequently an implicit one is used for the odd points. In doing so no implicit equations have to be solved directly, since the explicit results can be used as approximations at the adjacent (even) points. That followed, the roles of odd and even points are exchanged in order to retain the symmetry.

Integration schemes of this kind have been successfully applied to several problems, including the Korteweg-De Vries equation [73] and the simulation of the spatio-temporal dynamics of semiconductor lasers [74, 75].

In our case, it is possible to apply it to the whole equation (B.1) on the one hand [72], or to use it as a replacement for the FFT based linear step in the standard BPM on the other hand. Within this thesis, the latter has been implemented.

Bibliography

[1] M. Remoissenet, *Waves Called Solitons (2nd ed.)*, Springer, Berlin, 1996.

[2] N. J. Zabusky and M. D. Kruskal, *Interaction of "solitons" in a collisionless plasma and the recurrence of initial states*, Phys. Rev. Lett. **15**, 240 (1965).

[3] R. Y. Chiao, E. Garmire, and C. H. Townes, *Self-trapping of optical beams*, Phys. Rev. Lett. **13**, 479 (1964).

[4] P. L. Kelley, *Self-focusing of optical beams*, Phys. Rev. Lett. **15**, 1005 (1965).

[5] J. Juul Rasmussen and K. Rypdal, *Blow-up in nonlinear Schroedinger equations - I. A general review*, Phys. Scr. **33**, 481 (1986).

[6] G. Fibich and B. Ilan, *Vectorial and random effects in self-focusing and in multiple filamentation*, Physica D **157**, 112 (2001).

[7] M. Segev, B. Crosignani, A. Yariv, and B. Fischer, *Spatial solitons in photorefractive media*, Phys. Rev. Lett. **68**, 923 (1992).

[8] A. V. Mamaev, M. Saffman, D. Z. Anderson, and A. A. Zozulya, *Propagation of light beams in anisotropic nonlinear media: From symmetry breaking to spatial turbulence*, Phys. Rev. A **54**, 870 (1996).

[9] G. C. Duree, J. L. Shultz, G. J. Salamo, M. Segev, A. Yariv, B. Crosignani, P. Di Porto, E. J. Sharp, and R. R. Neurgaonkar, *Observation of self-trapping of an optical beam due to the photorefractive effect*, Phys. Rev. Lett. **71**, 533 (1993).

[10] M. Tiemann, J. Petter, and T. Tschudi, *Infrared guiding behavior in a 1 x N spatial soliton switch*, Opt. Comm. **281**, 175 (2008).

[11] E. Yablonovitch, *Inhibited spontaneous emission in solid-state physics and electronics*, Phys. Rev. Lett. **58**, 2059 (1987).

[12] S. John, *Strong localization of photons in certain disordered dielectric superlattices*, Phys. Rev. Lett. **58**, 2486 (1987).

[13] Y. S. Kivshar and G. P. Agrawal, *Optical Solitons: From Fibers to Photonic Crystals*, Acad. Press, San Diego, 2003.

[14] J. W. Fleischer, M. Segev, N. K. Efremidis, and D. N. Christodoulides, *Observation of two-dimensional discrete solitons in optically induced nonlinear photonic lattices*, Nature **422**, 147 (2003).

[15] Y. V. Kartashov, V. A. Vysloukh, and L. Torner, *Surface gap solitons*, Phys. Rev. Lett. **96**, 073901 (2006).

[16] A. A. Sukhorukov, D. N. Neshev, and Y. S. Kivshar, *Shaping and control of polychromatic light in nonlinear photonic lattices*, Opt. Expr. **15**, 13058 (2007).

[17] F. Dalfovo, S. Giorgini, L. P. Pitaevskii, and S. Stringari, *Theory of Bose-Einstein condensation in trapped gases*, Rev. of Mod. Phys. **71**, 463 (1999).

[18] O. Zobay, S. Pötting, P. Meystre, and E. M. Wright, *Creation of gap solitons in Bose-Einstein condensates*, Phys. Rev. A **59**, 643 (1999).

[19] P. J. Y. Louis, E. A. Ostrovskaya, C. M. Savage, and Y. S. Kivshar, *Bose-Einstein condensates in optical lattices: Band-gap structure and solitons*, Phys. Rev. A **67**, 013602 (2003).

[20] E. A. Ostrovskaya and Y. S. Kivshar, *Matter-wave gap solitons in atomic band-gap structures*, Phys. Rev. Lett. **90**, 160407 (2003).

[21] A. A. Sukhorukov and Y. S. Kivshar, *Generation and stability of discrete gap solitons*, Opt. Lett. **28**, 2345 (2003).

[22] B. Eiermann, T. Anker, M. Albiez, M. Taglieber, P. Treutlein, K.-P. Marzlin, and M. K. Oberthaler, *Bright Bose-Einstein gap solitons of atoms with repulsive interaction*, Phys. Rev. Lett. **92**, 23401 (2004).

[23] N. K. Efremidis, S. Sears, D. N. Christodoulides, J. W. Fleischer, and M. Segev, *Discrete solitons in photorefractive optically induced photonic lattices*, Phys. Rev. E **66**, 046602 (2002).

[24] D. Träger, R. Fischer, D. N. Neshev, A. A. Sukhorukov, C. Denz, W. Królikowski, and Y. S. Kivshar, *Nonlinear Bloch modes in two-dimensional photonic lattices*, Opt. Expr. **14**, 1913 (2006).

[25] R. Fischer, D. Träger, D. N. Neshev, A. A. Sukhorukov, W. Krolikowski, C. Denz, and Y. S. Kivshar, *Reduced-symmetry two-dimensional solitons in photonic lattices*, Phys. Rev. Lett. **96**, 023905 (2006).

[26] J. W. Fleischer, G. Bartal, O. Cohen, T. Schwartz, O. Manela, B. Freedman, M. Segev, H. Buljan, and N. K. Efremidis, *Spatial photonics in nonlinear waveguide arrays*, Opt. Expr. **13**, 1780 (2005).

[27] H. Trompeter, W. Królikowski, D. N. Neshev, A. S. Desyatnikov, A. A. Sukhorukov, Y. S. Kivshar, T. Pertsch, U. Peschel, and F. Lederer, *Bloch oscillations and Zener tunneling in two-dimensional photonic lattices*, Phys. Rev. Lett. **96**, 053903 (2006).

[28] A. Ciattoni, P. Di Porto, B. Crosignani, and A. Yariv, *Vectorial nonparaxial propagation equation in the presence of a tensorial refractive-index perturbation*, J. Opt. Soc. Am. B **17**, 809 (2000).

[29] N. V. Kukhtarev, V. B. Markov, S. G. Odoulov, M. S. Soskin, and V. L. Vinetskii, *Holographic storage in electrooptic crystals. I. steady state + II. beam coupling - light amplification*, Ferroelectrics **22**, 949 (1979).

[30] A. A. Zozulya and D. Z. Anderson, *Propagation of an optical beam in a photorefractive medium in the presence of a photogalvanic nonlinearity or an externally applied electrical field*, Phys. Rev. A **51**, 1520 (1995).

[31] A. Stepken, *Optische räumliche Solitonen in photorefraktiven Kristallen*, Dissertation (TU Darmstadt), Shaker Verlag, Aachen, 2001.

[32] W. Królikowski, M. Saffman, B. Luther-Davies, and C. Denz, *Anomalous interaction of spatial solitons in photorefractive media*, Phys. Rev. Lett. **80**, 3240 (1998).

[33] W. Królikowski, N. Akhmediev, M. Luther-Davies, and B. Cronin-Golomb, *Self-bending photorefractive solitons*, Phys. Rev. E **54**, 5761 (1996).

[34] B. B. Baizakov, V. V. Konotop, and M. Salerno, *Regular spatial structures in arrays of Bose-Einstein condensates induced by modulational instability*, J. Phys. B **35**, 5105 (2002).

[35] M. Petrović, D. Träger, A. Strinić, M. Belić, J. Schröder, and C. Denz, *Solitonic lattices in photorefractive crystals*, Phys. Rev. E **68**, 055601R (2003).

[36] A. S. Desyatnikov, E. A. Ostrovskaya, Y. S. Kivshar, and C. Denz, *Composite band-gap solitons in nonlinear optically induced lattices*, Phys. Rev. Lett. **91**, 153902 (2003).

[37] A. S. Desyatnikov, D. N. Neshev, Y. S. Kivshar, N. Sagemerten, D. Träger, J. Jägers, C. Denz, and Y. V. Kartashov, *Nonlinear photonic lattices in anisotropic nonlocal self-focusing media*, Opt. Lett. **30**, 869 (2005).

[38] Z. Chen, H. Martin, A. Bezryadina, D. Neshev, Y. S. Kivshar, and D. N. Christodoulides, *Experiments on Gaussian beams and vortices in optically induced photonic lattices*, J. Opt. Soc. Am. B **22**, 1395 (2005).

[39] D. N. Neshev, T. J. Alexander, E. A. Ostrovskaya, Y. S. Kivshar, H. Martin, I. Makasyuk, and Z. Chen, *Observation of discrete vortex solitons in optically induced photonic lattices*, Phys. Rev. Lett. **92**, 123903 (2004).

[40] J. W. Fleischer, G. Bartal, O. Cohen, O. Manela, M. Segev, J. Hudock, and D. N. Christodoulides, *Observation of vortex-ring "discrete" solitons in 2d photonic lattices*, Phys. Rev. Lett. **92**, 123904 (2004).

[41] B. Terhalle, A. S. Desyatnikov, C. Bersch, D. Träger, L. Tang, J. Imbrock, Y. S. Kivshar, and C. Denz, *Anisotropic photonic lattices and discrete solitons in photorefractive media*, Appl. Phys. B **86**, 399 (2007).

[42] P. Rose, T. Richter, B. Terhalle, J. Imbrock, F. Kaiser, and C. Denz, *Discrete and dipole-mode gap solitons in higher-order nonlinear photonic lattices*, Appl. Phys. B **89**, 521 (2007).

[43] N. Aközbek and S. John, *Optical solitary waves in two- and three-dimensional nonlinear photonic band-gap structures*, Phys. Rev. E **57**, 2287 (1998).

[44] T. J. Alexander, E. A. Ostrovskaya, and Y. S. Kivshar, *Self-trapped nonlinear matter waves in periodic potentials*, Phys. Rev. Lett. **96**, 040401 (2006).

[45] T. J. Alexander and Y. S. Kivshar, *Soliton complexes and flat-top nonlinear modes in optical lattices*, Appl. Phys. B **82**, 203 (2006).

[46] T. Mayteevarunyoo and B. A. Malomed, *Stability limits for gap solitons in a Bose-Einstein condensate trapped in a time-modulated optical lattice*, Phys. Rev. A **74**, 033616 (2006).

[47] A. A. Sukhorukov and Y. S. Kivshar, *Spatial optical solitons in nonlinear photonic crystals*, Phys. Rev. E **65**, 036609 (2002).

[48] D. E. Pelinovsky, A. A. Sukhorukov, and Y. S. Kivshar, *Bifurcations and stability of gap solitons in periodic potentials*, Phys. Rev. E **70**, 036618 (2004).

[49] T. Richter, K. Motzek, and F. Kaiser, *Long distance stability of gap solitons*, Phys. Rev. E **75**, 016601 (2007).

[50] N. G. Vakhitov and A. A. Kolokolov, *Stationary solutions of the wave equation in a medium with nonlinearity saturation*, Radiophys. Quant. Electr. **16**, 783 (1973).

[51] A. A. Kolokolov, *Stability of stationary solutions of nonlinear wave equations*, Radiophys. Quant. Electr. **17**, 1016 (1974).

[52] K. Motzek, *Instabilities of Spatial Solitons in Saturable Nonlinear Media*, Dissertation (TU Darmstadt), Darmstadt, 2005.

[53] C. Farrell and U. Leonhardt, *The perfectly matched layer in numerical simulations of nonlinear and matter waves*, J. Opt. B **7**, 1 (2005).

[54] A. S. Desyatnikov, N. Sagemerten, R. Fischer, B. Terhalle, D. Träger, D. N. Neshev, A. Dreischuh, C. Denz, W. Krolikowski, and Y. S. Kivshar, *Two-dimensional self-trapped nonlinear photonic lattices*, Opt. Expr. **14**, 2851 (2006).

[55] C. R. Rosberg, D. N. Neshev, A. A. Sukhorukov, W. Krolikowski, and Y. S. Kivshar, *Observation of nonlinear self-trapping in triangular photonic lattices*, Opt. Lett. **32**, 397 (2007).

[56] O. Peleg, G. Bartal, B. Freedman, O. Manela, M. Segev, and D. N. Christodoulides, *Conical diffraction and gap solitons in honeycomb photonic lattices*, Phys. Rev. Lett. **98**, 103901 (2007).

[57] T. J. Alexander, A. S. Desyatnikov, and Y. S. Kivshar, *Multivortex solitons in triangular photonic lattices*, Opt. Lett. **32**, 1293 (2007).

[58] E. A. Ostrovskaya and Y. S. Kivshar, *Matter wave gap vortices in optical lattices*, Phys. Rev. Lett. **93**, 160405 (2004).

[59] T. J. Alexander, A. A. Sukhorukov, and Y. S. Kivshar, *Asymmetric vortex solitons in nonlinear periodic lattices*, Phys. Rev. Lett. **93**, 063901 (2004).

[60] A. Bezryadina, D. N. Neshev, A. S. Desyatnikov, J. Young, Z. Chen, and Y. S. Kivshar, *Observation of topological transformations of optical vortices in two-dimensional photonic lattices*, Opt. Expr. **14**, 8317 (2006).

[61] B. Terhalle, T. Richter, A. S. Desyatnikov, D. N. Neshev, W. Królikowski, F. Kaiser, C. Denz, and Y. S. Kivshar, *Observation of multivortex solitons in photonic lattices*, accepted for publication in Phys. Rev. Lett. (2008).

[62] W. Firth and D. V. Skryabin, *Optical solitons carrying orbital angular momentum*, Phys. Rev. Lett. **79**, 2450 (1997).

[63] H. Sakaguchi and B. A. Malomed, *Higher-order vortex solitons, multipoles, and supervortices on a square optical lattice*, Europhys. Lett. **72**, 698 (2005).

[64] J. Yang, *Stability of vortex solitons in a photorefractive optical lattice*, New J. of Phys. **6**, 47 (2003).

[65] T. Richter and F. Kaiser, *Anisotropic gap vortices in photorefractive media*, Phys. Rev. A **76**, 033818 (2007).

[66] J. J. García-Ripoll and V. M. Pérez-García, *Optimizing Schrödinger functionals using sobolev gradients: Applications to quantum mechanics and nonlinear optics*, SIAM J. Sci. Comput. **23**, 1316 (2001).

[67] V. I. Petviashvili, *On the equation of a nonuniform soliton*, Fiz. Plasmy **2**, 469 (1976).

[68] A. A. Zozulya, D. Z. Anderson, A. V. Mamaev, and M. Saffman, *Solitary attractors and low-order filamentation in anisotropic self-focusing media*, Phys. Rev. A **57**, 522 (1998).

[69] T. I. Lakoba and J. Yang, *A generalized Petviashvili iteration method for scalar and vector hamiltonian equations with arbitrary form of nonlinearity*, J. Comp. Phys. **226**, 1668 (2007).

[70] Z. H. Musslimani and J. Yang, *Self-trapping of light in a two-dimensional photonic lattice*, J. Opt. Soc. Am. B **21**, 973 (2004).

[71] private discussion with Kristian Motzek (IAP, TU Darmstadt).

[72] T. R. Taha and M. J. Ablowitz, *Analytical and numerical aspects of certain nonlinear evolution equations. II. Numerical, nonlinear Schrödinger equation*, J. Comp. Phys. **55**, 203 (1984).

[73] I. S. Greig and J. L. Morris, *A hopscotch method for the Korteweg-de Vries equation*, J. Comp. Phys. **20**, 64 (1976).

[74] H. Adachihara, O. Hess, R. Indik, and J. V. Moloney, *Semiconductor laser array dynamics: Numerical simulations on multistripe index-guided lasers*, J. Opt. Soc. Am. B **10**, 496 (1993).

[75] M. Münkel, *Raum-zeitliche Strukturbildung in Halbleiterlasern mit zeitverzögerter Rückkopplung*, Dissertation (TU Darmstadt), Darmstadt, 1998.

Danksagung

Ich möchte an dieser Stelle noch denjenigen Personen meinen Dank aussprechen, ohne deren Unterstützung diese Arbeit sicher nicht in ihrer heutigen Form vorliegen würde.

Zuerst danke ich *Prof. Friedemann Kaiser* dafür, daß er mir die Promotion in seiner Arbeitsgruppe ermöglicht und stets für ein sehr angenehmes Arbeitsverhältnis gesorgt hat. Dadurch konnte ich in relativ kurzer Zeit Einblick in viele Bereiche des „wissenschaftlichen Alltags“ erhalten und genoß dennoch eine recht große Freiheit. *Prof. Robert Roth* danke ich für die Übernahme des Korreferats.

Meinen Kollegen *Martin Gassel* und *Erik Glatt* gilt mein besonderer Dank für das entspannte und freundschaftliche Verhältnis, welches sich nicht nur auf die Arbeitsgruppe beschränkt hat.

Bei meinem Vorgänger *Kristian Motzek* bedanke ich mich für die Einführung in das Thema der Gap-Solitonen, sowie für die hilfreichen Diskussionen in der Anfangsphase der Arbeit.

Prof. Cornelia Denz und ihrer Arbeitsgruppe an der Westfälischen Wilhelms-Universität Münster gebührt mein Dank für die Einladung zu einem Kolloquiumsvortrag und die daraus resultierende, äußerst produktive Zusammenarbeit mit vielen Anregungen aus experimenteller Sicht. Dies gilt insbesondere für *Bernd Terhalle* und *Patrick Rose*.

Anton Desyatnikov aus der Arbeitsgruppe von *Prof. Yuri Kivshar* in Canberra danke ich für etliche Diskussionen, die mich an vielen Stellen ermutigt haben, das angefangene Thema weiterzuverfolgen und zu vertiefen.

Den Mitgliedern der Arbeitsgruppe *Experimentelle Licht- und Teilchenoptik* am IAP danke ich für die Einladungen zu ihren Workshops und für die sehr nette und entspannte Atmosphäre dort.

Abschließend möchte ich mich noch bei meinen Eltern für die vielfältige Unterstützung während der Arbeit bedanken.

Lebenslauf

Persönliche Daten

Name	Tobias Richter
Geburtsdatum	27.1.1979
Geburtsort	Frankfurt am Main
Staatsangehörigkeit	deutsch
Familienstand	ledig
Anschrift	Jahnstraße 55, 64285 Darmstadt

Schulausbildung

1985 - 1989	Grundschule (Selzerbachschule Klein-Karben)
1989 - 1998	Gymnasium (Augustinerschule Friedberg/Hessen)
6/1998	Abitur

Zivildienst

10/1998 - 10/1999	ASB Kreisverband Wetterau (Groß-Karben)

Hochschulausbildung

10/1999 - 12/2004	Studium der Physik an der TU Darmstadt
9/2001	Vordiplom
12/2003 - 10/2004	Diplomarbeit unter der Leitung von Prof. F. Kaiser am Institut für Angewandte Physik der TU Darmstadt; Titel „Dynamik gegenläufiger Solitonen“
12/2004	Diplom
seit 4/2005	Promotion unter der Leitung von Prof. F. Kaiser am Institut für Angewandte Physik der TU Darmstadt

Berufstätigkeit

5/1998 - 9/1998	Aushilfsangestellter in der Hauptabteilung Datenverarbeitung der Deutschen Bundesbank
10/2001 - 3/2003 4/2004 - 2/2005	Wissenschaftliche Hilfskraft zur Betreuung von Übungsgruppen in den Fachbereichen Physik und Mathematik
seit 4/2005	Wissenschaftlicher Mitarbeiter von Prof. F. Kaiser am Institut für Angewandte Physik der TU Darmstadt; Betreuung von Übungsgruppen und Seminaren; Administration des lokalen Rechnernetzwerks der Arbeitsgruppe

Hiermit erkläre ich an Eides statt, daß ich
die vorliegende Dissertation selbständig verfaßt
und nur die angegebenen Hilfsmittel verwendet habe.
Ich habe bisher keinen Versuch unternommen, an einer
anderen Hochschule das Promotionsverfahren einzuleiten.

Darmstadt, im Mai 2008